

Influencing the Ionic Space Charge Potential in Grain Boundaries of Oxide Ceramics

Von der Fakultät Chemie der Universität Stuttgart
zur Erlangung der Würde eines

Doktors der Naturwissenschaften

(Dr. rer. nat.)

genehmigte Abhandlung

Vorgelegt von

Michael Patrick Weissmayer

aus Stuttgart

Hauptberichter:	Prof. Dr. rer. nat. J. Maier
Mitberichterin:	Prof. Dr. rer. nat. A. Weidenkaff
Prüfungsvorsitzender:	Prof. Dr. rer. nat. T. Schleid

Tag der Einreichung:	21.11.2016
Tag der mündlichen Prüfung:	13.01.2017

Max-Planck-Institut für Festkörperforschung

Stuttgart

2017

Für Lisa

Erklärung über die Eigenständigkeit der Dissertation

Die vorliegende Doktorarbeit mit dem Titel *Influencing the Ionic Space Charge Potential in Grain Boundaries of Oxide Ceramics* wurde vom Autor selbst in der Abteilung von Prof. Maier am Max-Planck-Institut für Festkörperforschung angefertigt. Der Inhalt ist die eigene Arbeit des Autors, Ausnahmen sind gekennzeichnet, und die Arbeit wurde noch nicht zur Erlangung einer Qualifizierung oder eines Titels an einer akademischen Institution eingereicht.

Declaration of Authorship

The work described in this thesis entitled *Influencing the Ionic Space Charge Potential in Grain Boundaries of Oxide Ceramics* was carried out by the author in the Department of Prof. Maier at the Max Planck Institute for Solid State Research. The contents are the original work of the author except where indicated otherwise and have not been previously submitted for any other degree or qualification at any academic institution.

Name/Name: _____

Unterschrift/Signature: _____

Ort/Place: _____

Datum/Date: _____

Contents

CONTENTS	IX
ABBREVIATIONS AND SYMBOLS	XI
LIST OF ABBREVIATIONS	XI
LIST OF SYMBOLS.....	XII
ZUSAMMENFASSUNG	XV
ABSTRACT	XIX
1 INTRODUCTION AND MOTIVATION	1
1.1 CHOICE OF MATERIAL AND OUTLINE OF THE THESIS	2
2 THEORETICAL BACKGROUND	5
2.1 INTRODUCTION TO SrTiO_3	5
2.2 DEFECT CHEMISTRY OF SrTiO_3	5
2.3 SPACE CHARGE EFFECTS	11
2.3.1 Gouy-Chapman model.....	12
2.3.2 Mott-Schottky model.....	13
2.3.3 Space charge layers in a mesoscopic situation	15
2.4 THE BRICK LAYER MODEL.....	16
2.5 CONSIDERATIONS ON CALCULATIONS OF THE ELECTRICAL CONDUCTIVITY	17
2.6 CLASSIFICATION OF GRAIN BOUNDARIES	22
3 EXPERIMENTAL METHODS	25
3.1 SAMPLE PREPARATION	25
3.1.1 Spark plasma sintering (SPS).....	25
3.1.2 Grain boundary decoration.....	26
3.1.3 Bicrystal fabrication.....	26
3.2 CHARACTERIZATION TECHNIQUES.....	27
3.2.1 Electrochemical impedance spectroscopy (EIS)	27
3.2.2 X-ray diffraction (XRD)	29
3.2.3 Electron microscopy.....	29
3.2.4 Inductively coupled plasma-optical emission spectrometry (ICP-OES) and Atomic absorption spectroscopy (AAS).....	30
3.2.5 Thermogravimetric analysis (TGA)	30
3.2.6 Diffuse reflectance spectroscopy.....	30
3.2.7 BET measurement	31
3.2.8 Density measurement	31
4 RESULTS AND DISCUSSION	33
4.1 NANOCRYSTALLINE SrTiO_3	33

4.1.1	<i>Powder characterization</i>	33
4.1.2	<i>Chemical analysis</i>	34
4.1.3	<i>Density characterization</i>	35
4.1.4	<i>Impedance spectroscopy analysis</i>	37
4.1.5	<i>Discussion</i>	50
4.2	SRTiO₃ BICRYSTALS	62
4.2.1	<i>Undoped SrTiO₃ bicrystals</i>	62
4.2.2	<i>Rb decorated $\Sigma 3$ (111) SrTiO₃ bicrystals</i>	71
5	CONCLUSIONS	77
	REFERENCES	79
	ACKNOWLEDGEMENTS	83

Abbreviations and symbols

List of abbreviations

AAS	Atomic absorption spectroscopy
AC	Alternating current
BET	Brunauer-Emmett-Teller
CPE	Constant phase element
CSL	Coincidence-site lattice
DC	Direct current
EDX	Energy dispersive x-ray spectroscopy
EIS	Electrochemical impedance spectroscopy
HAGB	High-angle grain boundary
GB	Grain boundary
ICP-OES	Inductively coupled plasma-optical emission spectrometry
LAGB	Low-angle grain boundary
SEM	Scanning electron microscopy
SPS	Spark plasma sintering
TEM	Transmission electron microscopy
TGA	Thermogravimetical analysis
XRD	X-ray diffraction

List of symbols

a	Unit cell parameter
A	Cross section area of the sample
A'	Acceptor according to the Kröger-Vink notation
c_j	Concentration of the defect j
$c_{j,\infty}$	Concentration of the defect j in the bulk
C	Capacitance
d_g	Grain size
ΔE_{bulk}	Activation energy of the bulk electrical conductivity
ΔE_{GB}	Activation energy of the grain boundary electrical conductivity
ΔE_{meso}	Activation energy of the electrical conductivity in the mesoscopic case
e	Elementary charge
e'	Electron according to the Kröger-Vink notation
$F(R_\infty)$	Kubelka-Munk function
h^\bullet	Electron hole according to the Kröger-Vink notation
k	Boltzmann constant
l	Sample thickness
m	Acceptor concentration
M	Dielectric modulus
M'	Real part of the dielectric modulus
M''	Imaginary part of the dielectric modulus
N	Number of grains
n	Electron concentration
p	Electron hole concentration
pO_2	Oxygen partial pressure
$pO_{2,min}$	Oxygen partial pressure at the minimum of the electronic conductivity

$pO_{2,min,bulk}$	Oxygen partial pressure at the minimum of the bulk electronic conductivity
$pO_{2,min,meso}$	Oxygen partial pressure at the minimum of the electronic conductivity in the mesoscopic case
Q	Constant phase element
Q_{core}	Grain boundary core charge density (per area)
Q_{cd}	Local charge density (per volume)
R	Resistance
R_{bulk}	Bulk resistance
R_{GB}	Grain boundary resistance
r_{∞}	Reflectance of an “infinitely” thick film
s	Exponent in the formula for the Tauc plot
T	Absolute temperature
u_j	Mobility of the defect j
v	Oxygen vacancy concentration
$V_O^{\bullet\bullet}$	Oxygen vacancy concentration according to the Kröger-Vink notation
V_{Sr}''	Strontium vacancy concentration according to the Kröger-Vink notation
z_j	Effective charge of the defect j
Z	Impedance
Z'	Real part of the impedance
Z''	Imaginary part of the impedance
A	Fitting parameter for impedance spectra
δ	Average grain boundary thickness
ϵ_0	Vacuum dielectric constant
ϵ_{bulk}	Bulk dielectric constant
ϵ_{GB}	Grain boundary dielectric constant
ϵ_r	Relative dielectric constant

Θ	Profile parameter in the Gouy-Chapman model
λ	Debye length
λ^*	Space charge layer width in the Mott-Schottky case
Σ	Degree of fit of a singular grain boundary
σ	Electrical conductivity
σ_{bulk}	Bulk electrical conductivity
σ_{bulk}^{\perp}	Bulk electrical conductivity in the depletion mode
$\sigma_{bulk}^{\parallel}$	Bulk electrical conductivity in the accumulation mode
σ_{GB}	Grain boundary electrical conductivity
σ_{GB}^{\perp}	Specific grain boundary electrical conductivity in the depletion mode
σ_{GB}^{\parallel}	Grain boundary electrical conductivity in the accumulation mode
σ_j	Partial conductivity of the defect j
σ_{meso}	Electrical conductivity in the mesoscopic case
σ_{meso}^{\perp}	Electrical conductivity in the mesoscopic case in the depletion mode
σ_{min}	Minimum of the electronic conductivity
σ_{tot}	Total electrical conductivity
τ	Relaxation time constant
τ_{bulk}	Bulk relaxation time constant
$\tau_{electrode}$	Electrode relaxation time constant
τ_{GB}	Grain boundary relaxation time constant
ϕ	Electrostatic potential
$\Delta\phi(x)$	Electrostatic potential in relation to the bulk
$\Delta\phi_0 = \Delta\phi(x=0)$	Space charge potential (electrostatic potential at the interface)
ω	Angular frequency

Zusammenfassung

In Elektrokeramiken beeinflussen Korngrenzen oftmals entscheidend die elektrischen Leitfähigkeitseigenschaften, da sie, bedingt durch den ionischen Charakter der Materialien, geladen sind. So behindern die Korngrenzen zum Beispiel den Transport von Ladungsträgern über sie hinweg, wenn Ladungsträger und Korngrenze Ladung gleichen Vorzeichens aufweisen. Aus diesem Grund ist es wünschenswert, die Ladung der Korngrenzen zu modifizieren, um damit die elektrischen Leitfähigkeitseigenschaften gezielt zu beeinflussen.

SrTiO_3 ist diesbezüglich für Forschungszwecke ein interessantes Material, da es einerseits ein gemischter Leiter ist und dadurch erlaubt, den Einfluss von Korngrenzmodifikationen auf p-Typ, n-Typ und ionische Leitfähigkeit am gleichen Material zu untersuchen. Andererseits ist SrTiO_3 von hoher technischer Relevanz, da es zum Beispiel als Varistor, als Anode in Festkörperbrennstoffzellen oder als Sauerstoffsensoren zum Einsatz kommt. Daher ist seine Defektchemie bereits umfassend analysiert und gut verstanden und bildet eine verlässliche Basis für die Interpretation von Effekten durch die Modifizierung von Korngrenzen.

Der Korngrenzkern von SrTiO_3 ist aufgrund strukturell nötiger Sauerstoffleerstellen positiv geladen. Um negativ geladene Defekte – vorzugsweise am Korngrenzkern – zu generieren, wurde die Korngrenze durch Dekorieren mit einem monovalenten Kation modifiziert, mit dem Ziel Sr^{2+} zu substituieren. Zu diesem Zweck wurde Rb ausgewählt, da es verglichen mit Sr einen um 20% größeren ionischen Radius hat, dies sollte die Positionierung des Kations im Korngrenzkern gewährleisten. Um zwei sehr unterschiedliche Fälle zu untersuchen, wurden zum einen nanostrukturierte Keramiken mit einer hohen Dichte an Korngrenzen mit Rb dekoriert und zum anderen selbst hergestellte Bikristalle, die nur eine spezifisch orientierte Korngrenze aufweisen.

Die nanostrukturierten Keramiken wurden mittels Sparkplasmasintern hergestellt. Dies ermöglicht das Sintern bei relativ niedrigen Temperaturen, was deutlich das Kornwachstum limitiert. Zwei verschiedene Dekorationsgehalte von 3at% Rb und 5,5at% Rb wurden ausgewählt, eine undotierte SrTiO_3 Probe diente als Referenz. Eine starke lokale Beschränkung der Rb-Verteilung in den nanostrukturierten Proben konnte durch Transmissionselektronenmikroskopie (TEM-EDX) Linienscans quer zur Korngrenze nachgewiesen werden. Diese wiesen Rb nur in einem 1 nm breiten Bereich nach, was beweist, dass sich Rb hauptsächlich im Korngrenzkern befindet. Die elektrochemische Charakterisierung erfolgte mittels Impedanzspektroskopie. Sauerstoffpartialdruckabhängigkeitsmessungen die einen Druckbereich von 1 bar bis zu 10^{-25} bar abdecken,

ermöglichen es, den Einfluss der Rb-Dekoration sowohl auf die p-Typ als auch die n-Typ Leitfähigkeit zu bestimmen. Unter oxidierenden Bedingungen, im p-Typ Bereich, zeigt das mit 3at% Rb dekorierte nanokristalline SrTiO₃ eine höhere Leitfähigkeit als das undotierte nanokristalline SrTiO₃, während das mit 5,5at% Rb dekorierte nanokristalline SrTiO₃ einen vergleichbaren Wert wie das undotierte SrTiO₃ aufweist. Diese Unterschiede können mit einem Raumladungseffekt erklärt werden. In beiden dekorierten Zusammensetzungen dringt Rb in die Gitterstruktur des Korngrenzkerns ein und diffundiert in eine sehr dünne Schicht direkt neben dem Kern. Mit einem zunehmenden Anteil an Rb das in die Gitterstruktur von SrTiO₃ diffundiert substituiert das Rb nicht nur Sr, sondern nimmt auch interstitielle Plätze ein. Daher bestimmen die relativen Konzentrationen von Rb auf Sr-Plätzen und auf interstitiellen Plätzen im Korngrenzkern die Änderung der Ladung des Korngrenzkerns verglichen mit dem nicht dotierten SrTiO₃. Im 3at% Rb dekorierten SrTiO₃ ist die Konzentration von Rb auf Sr Plätzen höher als die auf interstitiellen Plätzen, was zu einer erhöhten Leitfähigkeit und einem reduzierten Raumladungspotenzial im Vergleich zur undotierten Probe führt. Beim 5,5at% Rb dekorierten SrTiO₃ hingegen sind die Konzentrationen von Rb auf interstitiellen Plätzen und auf Sr Plätzen vergleichbar. Dementsprechend sind die Leitfähigkeit und das Raumladungspotenzial ähnlich dem im undotierten Fall. Unter reduzierenden Bedingungen, im n-Typ-Bereich, zeigen undotiertes und mit 3at% Rb dotiertes SrTiO₃ sehr ähnliche Leitfähigkeiten, wohingegen das mit 5,5at% Rb dekorierte SrTiO₃ etwas niedrigere Werte aufweist. Diese Ergebnisse können nicht allein mit einem Raumladungseffekt erklärt werden. Vielmehr ist die lokale Bandlücke in den Rb dekorierten Proben leicht verändert verglichen mit der undotierten Referenz, was zu den jeweiligen n-Typ Leitfähigkeiten führt. Die Bandlücke ist für die 3at% Rb dekorierte Zusammensetzung kleiner und für die 5,5at% Rb dekorierte größer als für undekoriertes SrTiO₃, was sich aus dem Minimum der elektronischen Leitfähigkeit in der Sauerstoffpartialdruckabhängigkeitsmessung der Leitfähigkeit ablesen lässt. Diese Veränderungen der Bandlücke wurden zudem durch Reflexionsspektroskopiemessungen bestätigt.

Im Fall der selbst hergestellten SrTiO₃ Bikristalle lag der Fokus darauf, passende Sinterbedingungen zur reproduzierbaren Herstellung der Bikristalle zu finden, da dies die erste Studie zur Herstellung von SrTiO₃ Bikristallen mittels Sparkplasmasintern ist. Dies stellte sich als schwieriger als zunächst vermutet heraus und wirkliche Reproduzierbarkeit konnte nicht erreicht werden. Gleichwohl konnte in einigen Fällen eine Verbindung zwischen den zwei Einkristallen erzielt und die Korngrenze eindeutig durch

Impedanzspektroskopiemessungen nachgewiesen werden. Ursprünglich war es beabsichtigt, $\Sigma 3$ (111) und $\Sigma 13$ (510) orientierte SrTiO_3 Bikristalle herzustellen, um zwei Korngrenzen mit verschiedenen Graden an Fehlorientierung zu untersuchen. Allerdings stellte sich das Sintern der $\Sigma 13$ (510) Orientierung als deutlich schwieriger als das der $\Sigma 3$ (111) Orientierung heraus, was vermutlich mit der höheren Korngrenzenergie der erstgenannten Orientierung zusammenhängt. Trotz der mit der Herstellung von SrTiO_3 -Bikristallen durch Sparkplasmasintern verbundenen Probleme wurde eine Rb Dekorierung ähnlich der der nanokristallinen Keramiken durchgeführt. Das erfolgreiche Auftragen von Rb auf die Einkristalloberfläche vor dem Sintern wurde durch chemische Analyse (ICP-OES Messungen) nachgewiesen. Allerdings streuen die Daten aus den Impedanzspektroskopiemessungen dieser $\Sigma 3$ (111) Rb dekorierten Bikristalle recht stark, so dass ein die Leitfähigkeit steigernder Effekt der Rb Dekorierung für die Bikristalle nicht zweifelsfrei nachgewiesen werden konnte.

Zusammengefasst gibt diese Arbeit einen tieferen Einblick in den Effekt der Dekorierung von Korngrenzen als Methode zur zielgerichteten Modifikation von Korngrenzkernladungen in SrTiO_3 . Weiterhin wurden SrTiO_3 Bikristalle, in denen die Korngrenze eindeutig mittels Impedanzspektroskopie nachgewiesen werden konnte, zum ersten Mal durch Sparkplasmasintern hergestellt.

Abstract

Grain boundaries in electroceramics often severely influence the overall electrical conduction properties since they are charged, which results from the ionic nature of the material. So for example they hinder the transport of charge carriers across them if they have an equal sign of charge. Therefore the selective modification of the grain boundary charge in order to tune the electrical conduction properties is desirable.

In this regard SrTiO₃ is a fascinating material to study, as it is on the one hand a mixed conductor, which allows one to investigate how a grain boundary modification affects p-type, n-type and ionic conductivity, all in the same material. On the other hand SrTiO₃ is of technological importance, as it is for example used as a varistor, as an anode in solid oxide fuel cells or as an oxygen sensor. Therefore its defect chemistry has been extensively studied and is well understood, which builds a reliable basis for the interpretation of the effects of a grain boundary modification.

The grain boundary core of SrTiO₃ is positively charged due to structurally necessary oxygen vacancies. Therefore, with the intention of generating negatively charged defects, preferably at the grain boundary core, a grain boundary modification by decoration with a monovalent cation was performed, aiming to substitute Sr²⁺. Rb⁺ was chosen for this purpose because of its 20% larger ionic radius compared to Sr²⁺, which should ensure the positioning at the grain boundary core. In order to investigate two very different scenarios the Rb decoration was performed on nanostructured ceramics with a high density of grain boundaries, as well as on home-made bicrystals, containing only one specifically oriented grain boundary.

For the fabrication of the nanostructured ceramics spark plasma sintering was employed. It enables sintering at relatively low temperatures, which greatly limits the grain growth. Two different decoration contents of 3at% Rb and 5.5at% Rb were chosen, while an undoped SrTiO₃ sample served as a reference. A strong local confinement of Rb in the nanostructured ceramics was confirmed by transmission electron microscopy (TEM-EDX) line scans across grain boundaries which could detect Rb only within a total range of 1 nm, proving that Rb is mostly located in the grain boundary core. The electrochemical characterization was carried out by means of impedance spectroscopy. Oxygen partial pressure dependence measurements, covering the range of 1 bar down to 10⁻²⁵ bar, allow the determination of the influence of the Rb decoration on both p-type and n-type conductivity. Under oxidizing conditions, in the p-type regime, the 3at% Rb decorated nanocrystalline SrTiO₃ displays a higher conductivity than undoped nanocrystalline SrTiO₃, whereas the conductivity of the 5.5at% Rb decorated

nanocrystalline SrTiO₃ is on the same level as the undoped SrTiO₃. These differences can be explained by a space charge effect. For both decorated compositions Rb enters the grain boundary core lattice structure and slightly diffuses into a very thin layer directly adjacent to the core. With an increasing amount of Rb entering the SrTiO₃ lattice structure it not only substitutes Sr, but is also placed interstitially. Therefore, the relative concentrations of Rb on Sr sites and on interstitial sites in the grain boundary core determine the change of the grain boundary core charge compared to undoped SrTiO₃. In the 3at% Rb decorated SrTiO₃ the concentration of Rb on Sr sites is higher than that of interstitially placed Rb, resulting in a higher conductivity and reduced space charge potential compared to undoped SrTiO₃. In the 5.5at% Rb decorated SrTiO₃ on the other hand the concentration of interstitially placed Rb is roughly equal to that of Rb on Sr sites, resulting in a similar conductivity and space charge potential as it is determined for undoped SrTiO₃. Under reducing conditions, in the n-type regime, undoped and 3at% Rb decorated SrTiO₃ display very similar conductivities, whereas the conductivity of 5.5at% Rb decorated SrTiO₃ is a bit lower. These findings cannot only be explained by a space charge effect. Rather the local band gap at the grain boundaries in the Rb decorated specimens is slightly altered compared to the undoped reference, which leads to the respective n-type conductivities. The band gap is decreased in the 3at% Rb decorated composition and increased in the 5.5at% Rb decorated composition (relative to undoped SrTiO₃), which can be concluded from the minimum of the electrical conductivity in the oxygen partial pressure dependence measurement of the conductivity. This band gap change is furthermore confirmed by diffuse reflectance spectroscopy measurements.

In case of the home-made SrTiO₃ bicrystals the main focus was to find suitable sintering conditions which allow a reproducible fabrication of the bicrystals, since this was the first time that a fabrication of SrTiO₃ bicrystals by spark plasma sintering was attempted. This proved more difficult than expected and actual reproducibility could not be achieved. Nevertheless, in several cases bonding between the two single crystals was realized and the grain boundary was unambiguously detected by impedance spectroscopy measurements. Initially the intention was to produce $\Sigma 3$ (111) and $\Sigma 13$ (510) oriented SrTiO₃ bicrystals in order to investigate two grain boundaries with different degrees of misorientation. However, sintering of the $\Sigma 13$ (510) orientation proved considerably more difficult than for the $\Sigma 3$ (111) orientation, which is probably related to the higher grain boundary energy of the former. Despite the challenges that were connected with the fabrication of SrTiO₃ bicrystals by spark plasma sintering a Rb decoration in a similar manner as performed for the nanostructured ceramics was realized. The successful application of Rb to the single crystal surface prior to

sintering was verified by chemical analysis (ICP-OES measurements). However, the data gathered by impedance spectroscopy measurements of these $\Sigma 3$ (111) Rb decorated bicrystals scatters a lot, so that a conductivity enhancing effect of the Rb decoration could not be unambiguously confirmed in case of the bicrystals.

In summary this work has given deeper insight into the effects of grain boundary decoration as a method which allows the purposeful modification of the grain boundary core charge in SrTiO_3 . Furthermore, SrTiO_3 bicrystals, for which the grain boundary was unambiguously identified by impedance spectroscopy, were for the first time fabricated by spark plasma sintering.

1 Introduction and motivation

Grain boundaries represent the decisive 2-dimensional defect in polycrystalline materials. By definition a grain boundary separates two grains that have the same crystal structure but different orientations. As such they possess specific properties, being the (compared to the regular bulk lattice) “disordered transition zone” which ensures connection of two neighboring grains.

However, when discussing an ionic polycrystalline material the definition above requires some more in-depth treatment. Inside a grain of such an ionic crystal, under equilibrium conditions, the differently charged point defects compensate each other, ensuring local electroneutrality. This situation changes at the grain boundary, since it can be charged as a result of the broken lattice symmetry. Such a local electrostatic charge then in turn causes the rearrangement of the mobile defects in proximity to the grain boundary core, resulting in so-called space charge layers. Therefore in the case of an ionic crystal, the grain boundary rather consists of the charged grain boundary core as well as the two adjacent space charge layers. Consequently also the defect profiles and thus the electrical conduction properties are altered compared to the bulk when approaching the grain boundary in an ionic material. These very unique properties have generated a lot of research related to grain boundaries in ionic crystals.

An impressive example of a purely grain boundary driven effect in the field of nanoionics is the mesoscopic electrical conduction in nanocrystalline SrTiO_3 [1-3]. SrTiO_3 is a mixed conductor that displays, depending on temperature and oxygen partial pressure, either electronic (p-type or n-type) or ionic conductivity. On microcrystalline and bicrystal samples of nominally pure and acceptor doped SrTiO_3 it has been shown in various studies [4-6] that both p-type and ionic conductivity under oxidizing conditions are severely blocked at the grain boundaries, demonstrating their positive charge. Due to the large dielectric constant of SrTiO_3 the space charge layers are relatively broad (a typical thickness is on the order of 60 nm). By reducing the grain size below two times the space charge layer width a mesoscopic situation with overlapping space charge layers can be achieved. When performing an electrochemical impedance measurement on such a mesoscopic sample one is not able to distinguish between bulk and grain boundaries (contrary to a microcrystalline sample where those responses are well separated) and instead a single response from the grain boundaries is seen. Furthermore the mesoscopic situation leads to very significant changes of the electrical conductivity compared to the bulk transport properties of a microcrystalline sample from the

same powder [2]: The p-type conductivity under oxidizing conditions is reduced by almost four orders of magnitude for the nanocrystalline sample, while the n-type conductivity under reducing conditions is enhanced by three orders of magnitude. Nominally the oxygen vacancy concentration is depleted by at least six orders of magnitude. In addition the p-n transition is shifted up to 12 orders of magnitude for the nanocrystalline sample regarding the oxygen partial pressure when compared to the microcrystalline one. All these effects can be nicely explained by applying a Mott-Schottky model to the overlapping space charge layers.

This example demonstrates the fascinating power of grain boundary engineering in the field of electrically conductive ceramics and at the same time represents the basis for this work. In the case of SrTiO₃ the question arises how far it is possible to reduce the positive grain boundary core charge by grain boundary modification in order to alter the ionic space charge potential and to possibly improve the p-type and ionic conductivity under oxidizing conditions. This work tries to give rise to a better understanding of how to systematically influence the space charge potential. While bicrystals offer the possibility to investigate the properties of an individual boundary parallel and along the interface, the response of polycrystalline materials is an average over various types and orientations. The first situation is ideal for basic investigations, whereas the second is significant for applications.

1.1 Choice of material and outline of the thesis

Being a mixed conductor SrTiO₃ offers the unique possibility to investigate, in one and the same sample, how a grain boundary modification affects p-type, n-type and ionic conductivity. SrTiO₃ also offers a good chemical and thermal stability and its defect chemistry is very well understood. Therefore it serves as a model material that can enable an understanding of more complex systems in the family of ABO₃ perovskites. [7-11]

For the analysis it is crucial to distinguish between grain boundary core, which is usually charged, and the adjacent space charge zone accommodating the compensating charge. Doping of SrTiO₃ grain boundaries is expected to be an effective means to vary and study the interfacial situation. The prerequisite for an unambiguous evidence is however to control the dopants position (core or space charge zone). For this purpose a large-sized monovalent cation, namely Rb⁺, is introduced to replace Sr²⁺ preferably in the core region. Such experiments and evaluation form the basis of the present thesis.

Chapter 2 “Theoretical background” gives an overview on the necessary concepts for the future data analysis and interpretation. Most important are the basics on the defect chemistry of undoped and acceptor doped SrTiO₃ and the chapter on space charge effects (2.3), which

depicts the two main mathematical models to solve the charge carrier distribution within a space charge zone.

The following chapter (3 “Experimental methods”) deals with the sample preparation via spark plasma sintering and comments on how the grain boundary modification is performed. Furthermore the various characterization techniques are presented, with emphasis on electrochemical impedance spectroscopy as it is the main tool for the electrochemical characterization of the samples in this work.

Finally the main results of this work are separately discussed and analyzed: Chapter 4.1 “Nanocrystalline SrTiO₃” deals with the nanocrystalline mesoscopic SrTiO₃ samples, whereas chapter 4.2 “SrTiO₃ bicrystals” highlights the main findings based on the analysis of single grain boundaries.

2 Theoretical background

2.1 Introduction to SrTiO₃

At room temperature SrTiO₃ crystallizes in the cubic perovskite structure ABO₃ (see Figure 1). The A-cation Sr²⁺ and the anion O²⁻ together form a face centered cubic cell with the B-cation Ti⁴⁺ sitting in the center. The Ti⁴⁺ is octahedrally coordinated with six O²⁻ ions, whereas each Sr²⁺ ion has twelve O²⁻ as nearest neighbors. The unit cell parameter of this centrosymmetric structure is $a = 3.905 \text{ \AA}$ [12], with a theoretical density of 5.12 g/cm^3 . Being both chemically and thermally very stable, SrTiO₃ serves as a model material for a lot of other (more complex) mixed (ionically and electronically) conducting perovskites such as BaTiO₃, PbTiO₃ or PbZrO₃.

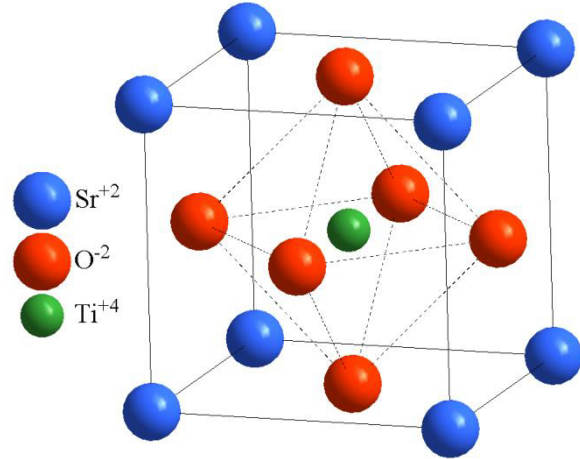


Figure 1 The cubic perovskite SrTiO₃.

2.2 Defect chemistry of SrTiO₃

Since SrTiO₃ serves as a model material for a whole family of perovskites it has been extensively studied for some decades. Therefore the defect chemistry and its relation to the electrical conduction properties are very well understood [7-9, 13]. The reference material in this work is nominally undoped SrTiO₃, which is nevertheless always slightly acceptor doped. For this reason in the following the behavior of point defects will be discussed together for both undoped and acceptor doped SrTiO₃.

Due to the close-packed perovskite structure the dominant ionic point defects in the bulk of SrTiO₃ are rather vacancies than interstitials. This is supported by the fact, that the partial Schottky disorder reaction,



is more favorable than both other Schottky disorder reactions and all Frenkel disorder reactions [14]. Assuming the activity of SrO to be constant, the respective mass action law for reaction 2.1 is formulated as

$$K_s = [\text{V}_{\text{Sr}}^{\prime\prime}] \cdot [\text{V}_{\text{O}}^{\bullet\bullet}] = K_s^0 \exp\left(-\frac{E_s}{kT}\right). \quad (2.2)$$

However, reaction 2.1 is only important at higher temperatures close to the temperatures employed for the conventional sintering of SrTiO₃ [11]. It is noteworthy that at lower temperatures the strontium vacancy concentration is frozen-in. The other important intrinsic defect reaction that has to be considered is the generation of electrons and holes according to

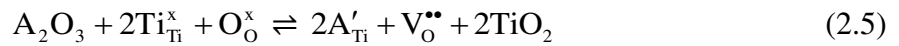


The corresponding mass action constant is defined as

$$K_B = n \cdot p = K_B^0 \exp\left(-\frac{E_B - \beta_B T}{kT}\right), \quad (2.4)$$

with n being the electron concentration, p the hole concentration, E_B the band gap of the material at 0 K and β_B the temperature coefficient of the band gap.

Since also nominally undoped SrTiO₃ is typically slightly acceptor doped (a typical impurity content would be on the order of a few hundred ppm), the presence of a trivalent acceptor A on the Ti site according to



has to be considered. It is important to note that the concentration of oxygen vacancies owing to the intrinsic Schottky reaction (2.1) is (at the temperatures of interest) lower than the oxygen vacancy concentration resulting from (2.5). Therefore, even the presence of such small amounts of acceptors is crucial for determining the defect chemistry of such a compound.

For the temperature range in which the main characterization by electrochemical impedance spectroscopy is performed in this work ($T = 400^\circ\text{C} - 650^\circ\text{C}$) the general electroneutrality condition for SrTiO₃ reads [7]

$$2v + p = m + n, \quad (2.6)$$

with v being the concentration of oxygen vacancies and m the acceptor concentration. For the temperature range $T = 400^\circ\text{C} - 650^\circ\text{C}$, the mobile charge carriers in SrTiO₃ are electrons, holes and oxygen vacancies. The other defects can be considered immobile and therefore they do not contribute to the electrical conduction. Equation 2.6 can be further simplified depending on the oxygen partial pressure of the surrounding environment. Together with the reaction equations for the incorporation of oxygen into the structure (or loss of oxygen from it), one can deduce the concentrations of the charge carriers, as well as (together with the mobility data) the electrical conduction properties of SrTiO₃ over a wide range of oxygen partial pressures. Figure 2 shows a Kröger-Vink diagram and a calculated oxygen partial

pressure dependence plot for SrTiO₃ at $T = 550^\circ\text{C}$ covering the partial pressure range of interest for this work ($pO_2 = 1 - 10^{-30}$ bar). The upcoming analysis will be conducted with the help of these diagrams.

Under oxidizing conditions oxygen is incorporated into the bulk according to



The corresponding mass action law for equation 2.7 is

$$K_{Ox} = \frac{p^2}{v \cdot pO_2^{1/2}} = K_{Ox}^0 \exp\left(-\frac{E_{Ox}}{kT}\right). \quad (2.8)$$

The concentration of oxygen vacancies is independent of the oxygen partial pressure and fixed by the acceptor content, which leads to the further simplified electroneutrality condition

$$2v = m. \quad (2.9)$$

Combining this equation with the mass action law in equation 2.8 results in the following expression for the concentration of holes in SrTiO₃ (cf. Figure 2 (a)):

$$p = \left(\frac{K_{Ox} \cdot m}{2}\right)^{1/2} \cdot pO_2^{1/4}. \quad (2.10)$$

A similar route to explain the n-type conductivity under reducing conditions can be taken, which is quite straightforward. In the regime of low pO_2 one has to consider the loss of oxygen from the lattice according to



with the corresponding mass action constant defined as

$$K_{Red} = pO_2^{1/2} \cdot v \cdot n^2 = K_{Red}^0 \exp\left(-\frac{E_{Red}}{kT}\right). \quad (2.12)$$

The electroneutrality condition is still the same as defined in equation 2.9, which then, in conjunction with equation 2.12, leads to the following dependence of the concentration of electrons in SrTiO₃ on the oxygen partial pressure:

$$n = \left(\frac{2K_{Red}}{m}\right)^{1/2} \cdot pO_2^{-1/4}. \quad (2.13)$$

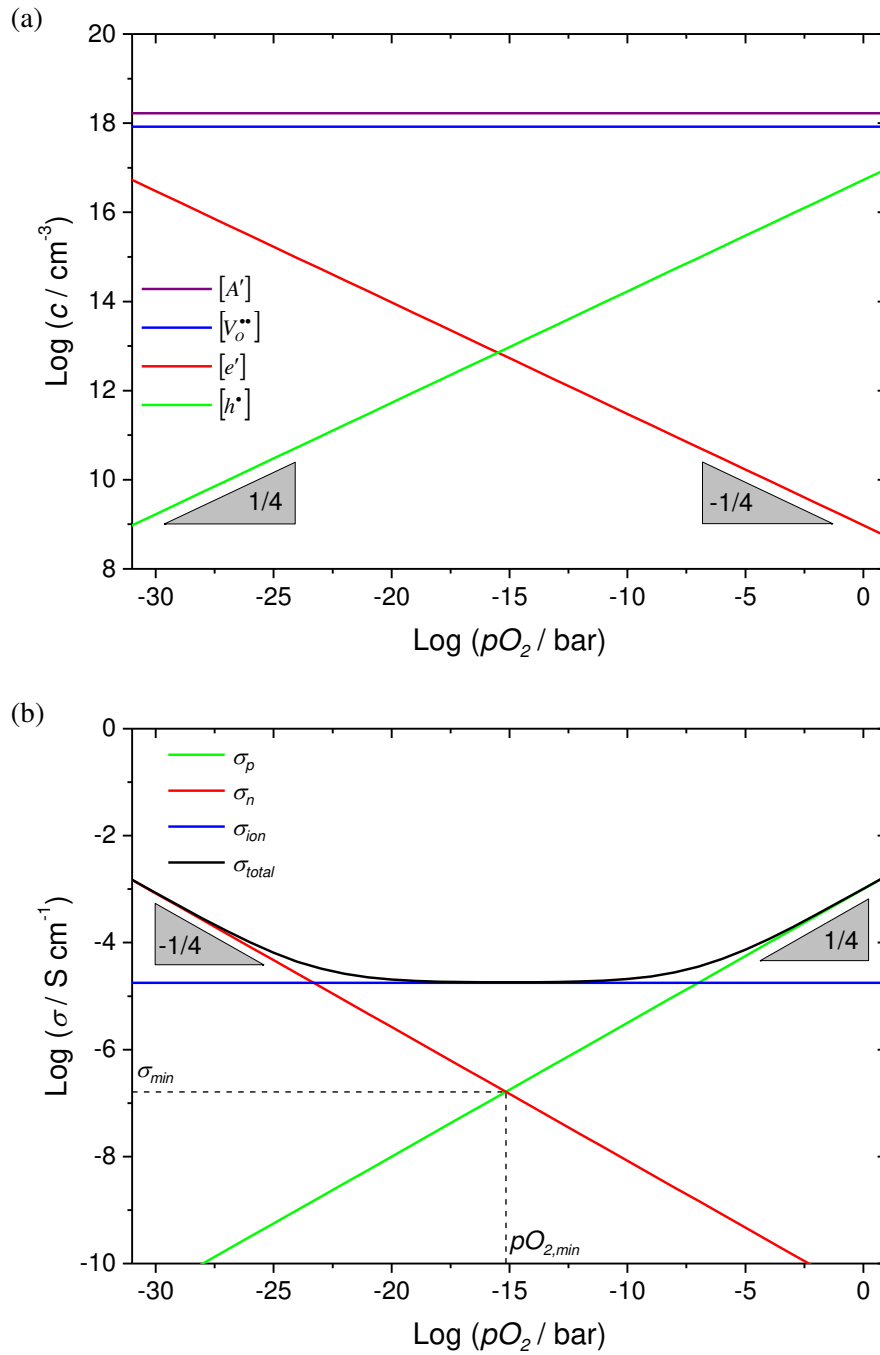


Figure 2 (a) Kröger-Vink diagram for SrTiO₃ and (b) oxygen partial pressure dependence of the bulk electrical conductivity of SrTiO₃ (both calculated for $T = 550^\circ\text{C}$ and an impurity content of 100 ppm acceptors; with the mass action and mobility data from [9]).

As one can see from the Kröger-Vink diagram in Figure 2 (a) the concentration of oxygen vacancies is the highest among the three mobile charge carriers (electrons, holes and oxygen vacancies) throughout the whole oxygen partial pressure range which is of interest in this work. However, in the same range the total conductivity of SrTiO₃ changes from p-type to ionic into n-type (cf. Figure 2 (b)). The total conductivity runs through a minimum which is flattened owing to the constant ionic contribution. This follows from

$$\sigma_{tot}(T, pO_2) = \sum_j \sigma_j = \sum_j z_j \cdot e \cdot c_j(T, pO_2) \cdot u_j(T), \quad (2.14)$$

which is the sum of the partial conductivities σ_j of each charge carrier j [15]. The partial conductivity for each charge carrier being the product of its effective charge z_j , the elementary charge e , its concentration c_j and its mobility u_j . At 550°C the mobility of oxygen vacancies is a couple of orders of magnitude lower than that of electrons and holes [9]. Thus, starting from a high oxygen partial pressure (e.g. from pure oxygen), one first encounters p-type conductivity with the typical slope of $1/4$. Reaching the intermediate oxygen partial pressure range ($pO_2 < 10^{-5}$ bar) the concentration of holes has decreased so much that a transition to purely ionic conductivity occurs. This is marked by the total conductivity reaching a plateau, since the concentration of oxygen vacancies is fixed by the acceptor content. Going to even lower oxygen partial pressures the concentration of electrons progressively increases and at some point, again due to the much higher mobility of the electrons compared to that of the oxygen vacancies, the total conductivity changes to n-type with the typical slope of $-1/4$.

As mentioned above, even nominally undoped SrTiO₃ usually contains several hundred ppm of acceptors, with Fe being the most common residual impurity. Since the Fe cation can switch its oxidation state between +3 and +4, one also has to consider the ionization reaction [9]



for such a redox active species.

The corresponding mass action constant is defined as

$$K_{Fe} = \frac{[Fe'_{Ti}] \cdot p}{[Fe^x_{Ti}]} = K_{Fe}^0 \exp\left(-\frac{E_{Fe} - \beta_{Fe} \cdot T}{kT}\right), \quad (2.16)$$

where

$$[Fe_{total}] = [Fe'_{Ti}] + [Fe^x_{Ti}] = \text{const}, \quad (2.17)$$

must hold because of mass conservation.

By combining equations 2.10, 2.16 and 2.17 one can determine the dependence of the Fe^{3+} concentration on the oxygen partial pressure, as displayed in Figure 3. In the higher oxygen partial pressure range, roughly for $pO_2 > 10^{-10}$ bar (at $T = 550^\circ\text{C}$), a considerable amount of the Fe is oxidized to its +4 state. This results in a lower hole concentration (and therefore lower p-type conductivity) in the high pO_2 regime for this SrTiO_3 ceramic, compared to a fictitious SrTiO_3 sample with the same concentration of an acceptor but no redox active impurities. Accordingly also the slope of the p-type conductivity in the oxygen partial pressure dependence plot of the conductivity of such a Fe containing SrTiO_3 ceramic is slightly lower than the previously theoretically predicted value of $\frac{1}{4}$. At $pO_2 < 10^{-10}$ bar basically all the Fe is reduced to Fe^{3+} and thus the previous derivations for the case of a general trivalent acceptor apply.

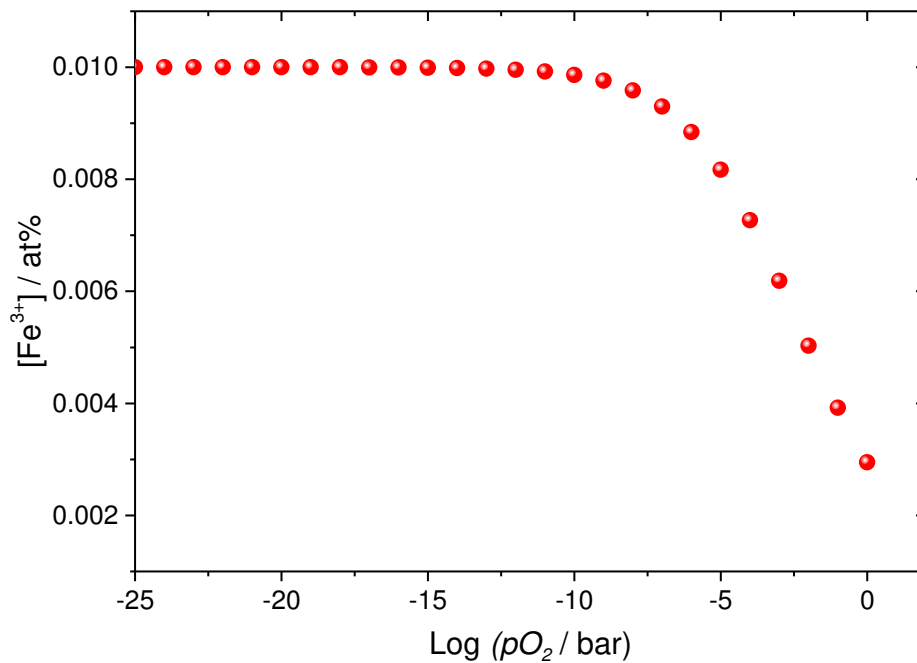


Figure 3: Oxygen partial pressure dependence of the Fe^{3+} concentration in SrTiO_3 calculated for $T = 550^\circ\text{C}$ and an acceptor concentration of 100 ppm Fe (mass action parameters taken from [9]).

All the defect chemistry reactions in undoped and acceptor doped SrTiO_3 that were discussed throughout this chapter, as well as their corresponding mass action parameters are summarized in Table 2.1. Note that all the theoretical calculations regarding the defect concentrations and conductivity in SrTiO_3 throughout this work are based on the data available from Denk *et al.* [9].

Table 2.1 Summary of the most important defect chemistry reactions in SrTiO₃ and their corresponding mass action parameters (mass action parameters for the partial Schottky disorder and the reduction reaction taken from [16], mass action parameters for the band-band transfer, the oxygen incorporation and the Fe ionization taken from [9]).

Equation	Mass action parameters
Partial Schottky disorder $K_S = K_S^0 \exp\left(-\frac{E_S}{kT}\right)$	$K_S^0 = 3 \cdot 10^{44} \text{ cm}^{-6}, E_S = 2.5 \text{ eV}$
Band-band transfer $K_B = K_B^0 \exp\left(-\frac{E_B - \beta_B T}{kT}\right)$	$K_B^0 = 7.67 \cdot 10^{42} \text{ cm}^{-6}, E_B = 3.30 \text{ eV}, \beta_B = 6.0 \cdot 10^{-4} \text{ eV} \cdot \text{K}^{-1}$
Oxygen incorporation $K_{O_x} = K_{O_x}^0 \exp\left(-\frac{E_{O_x}}{kT}\right)$	$K_{O_x}^0 = 1.02 \cdot 10^{23} \text{ Pa}^{-1/2} \cdot \text{cm}^{-3}, E_{O_x} = 1.63 \text{ eV}$
Reduction reaction $K_{Red} = K_{Red}^0 \exp\left(-\frac{E_{Red}}{kT}\right)$	$K_{Red}^0 = 5 \cdot 10^{71} \text{ cm}^{-9} \cdot \text{bar}^{1/2}, E_{Red} = 6.1 \text{ eV}$
Fe ionization $K_{Fe} = K_{Fe}^0 \exp\left(-\frac{E_{Fe} - \beta_{Fe} \cdot T}{kT}\right)$	$K_{Fe}^0 = 2.77 \cdot 10^{21} \text{ cm}^{-3}, E_{Fe} = 1.18 \text{ eV}, \beta_{Fe} = 3.7 \cdot 10^{-4} \text{ eV} \cdot \text{K}^{-1}$

2.3 Space charge effects

So far the discussion of defect chemistry of SrTiO₃ regarded only the bulk properties under equilibrium conditions. However, the electrochemical situation changes significantly in the regions close to the grain boundaries. The grain boundaries are crystallographic mismatch zones due to the differently oriented grains and are electrically charged. Here the electroneutrality condition that was used before for the bulk has to be replaced by the more general Poisson's equation [17-19]

$$\nabla^2 \phi = -\frac{Q_{cd}}{\epsilon_0 \cdot \epsilon_r}, \quad (2.18)$$

with ϕ being the electrostatic potential, Q_{cd} the local charge density (per volume) and ϵ_0 and ϵ_r the vacuum permittivity and the relative material's dielectric constant, respectively.

It has been commonly observed that there is a net excess of oxygen vacancies in the core of the grain boundaries in acceptor doped SrTiO₃ which leads to a positive core charge [20]. As a result of this excess positive charge, at equilibrium, the mobile charge carriers are redistributed (depending on their sign they are either enriched (electrons) or depleted (holes and oxygen vacancies)) in proximity of the grain boundaries in order to maintain

electroneutrality, resulting in the formation of so-called space charge layers [4, 5, 14, 21]. This local charge redistribution can be formally treated in terms of the space charge model [22], as follows.

The concentration profile $c_j(x)$ for any mobile defect j throughout the grain is given by [17]

$$c_j(x) = c_{j,\infty} \cdot \exp\left(-\frac{z_j \cdot e \cdot \Delta\phi(x)}{k \cdot T}\right), \quad (2.19)$$

where $c_{j,\infty}$ is the concentration of the defect j in the bulk and $\Delta\phi(x) = \phi(x) - \phi_\infty$ is the electrostatic potential at a certain distance x from the grain boundary with respect to the bulk potential ϕ_∞ . Combination of the two equations 2.18 and 2.19 yields the Poisson-Boltzmann differential equation for the one dimensional case [23]:

$$\frac{\partial^2 \phi(x)}{\partial x^2} = -\frac{e}{\epsilon_0 \cdot \epsilon_r} \sum_j z_j \cdot c_{j,\infty} \exp\left(-\frac{z_j \cdot e}{k \cdot T} \cdot \Delta\phi(x)\right). \quad (2.20)$$

Two main models have been developed for the solution of the Poisson-Boltzmann differential equation from which the determination of the charge carrier spatial distribution within the space charge layers results. These are the Gouy-Chapman and the Mott-Schottky models, which are presented in the following subsections.

2.3.1 Gouy-Chapman model

In the Gouy-Chapman case, all the charge carriers (including dopants or impurities) redistribute as a consequence of the space charge potential. In such a situation, equation 2.20 can be analytically solved only in the case of two charge carriers having valence $z_1 = -z_2$ and $c_{1,\infty} = c_{2,\infty}$ [24]. By applying appropriate semi-infinite boundary conditions (setting the reference point for the potential to zero in the bulk and defining variations of the potential in the bulk to be zero: $\phi'(x \rightarrow \infty) = 0$) yields the spatial variation of the electrostatic potential in the Gouy-Chapman case [23]:

$$\phi(x) = \frac{2 \cdot k \cdot T}{z_j \cdot e} \ln\left(\frac{1 + \Theta \exp(-x/\lambda)}{1 - \Theta \exp(-x/\lambda)}\right). \quad (2.21)$$

Here λ is the Debye length, defined as

$$\lambda = \sqrt{\frac{\varepsilon_0 \cdot \varepsilon_r \cdot k \cdot T}{2 \cdot z_j^2 \cdot e^2 \cdot c_{j,\infty}}} \quad (2.22)$$

and Θ the profile parameter:

$$\Theta = \tanh\left(\frac{z_j \cdot e \cdot \Delta\phi_0}{4 \cdot k \cdot T}\right). \quad (2.23)$$

$\Delta\phi_0 = \phi(0) - \phi_\infty$ is the potential at the grain boundary core, relative to the bulk and hence called the space charge potential. By combining the two equations 2.19 and 2.21, one ends up with the defect profile for a defect j within the space charge layer in the Gouy-Chapman case, given by

$$c_j(x) = c_{j,\infty} \left(\frac{1 + \Theta \exp(-x/\lambda)}{1 - \Theta \exp(-x/\lambda)} \right)^{2z_j}. \quad (2.24)$$

Within 2λ the concentration of a defect j nearly goes back to the bulk concentration, therefore this is a good measure for the extent of the space charge zone in the Gouy-Chapman case. The charge density in the grain boundary core (per area) can be calculated according to [23]

$$Q_{core} = \sqrt{8 \cdot k \cdot T \cdot c_{j,\infty} \cdot \varepsilon_0 \cdot \varepsilon_r} \sinh\left(\frac{z_j \cdot e \cdot \Delta\phi_0}{2 \cdot k \cdot T}\right). \quad (2.25)$$

2.3.2 Mott-Schottky model

In the Mott-Schottky model the acceptors form majority carriers and are assumed to be immobile, i.e. their concentration is thus constant up to the boundary [25]. In the case of SrTiO₃, this is a reasonable assumption at the typical temperatures of this study (sintering at 850°C, electrical characterization at 400°C - 650°C) [4, 21]. Due to the space charge potential the counter majority defect is depleted and the acceptors determine the charge density. One can neglect the depleted defects and the charge density is assumed to be constant. With these assumptions equation 2.20 can be simplified to [24]

$$\frac{\partial^2 \phi(x)}{\partial x^2} = -\frac{z_j \cdot e \cdot c_{j,\infty}}{\varepsilon_0 \cdot \varepsilon_r} = \text{const} \quad (2.26)$$

and then integrated assuming appropriate semi-infinite boundary conditions ($\phi(\lambda^*) = \phi_\infty$ and $\phi'(\lambda^*) = 0$). This gives the spatial variation of the electrostatic potential in the Mott-Schottky case:

$$\Delta\phi(x) = -\frac{z_j \cdot e \cdot c_{j,\infty}}{2 \cdot \varepsilon_0 \cdot \varepsilon_r} (x - \lambda^*)^2. \quad (2.27)$$

The term λ^* , called the Mott-Schottky space charge layer width, gives the lateral extension of the zone in which redistribution of the charge carriers occurs and is defined as

$$\lambda^* = \sqrt{\frac{2 \cdot \varepsilon_0 \cdot \varepsilon_r \cdot \Delta\phi_0}{z_j \cdot e \cdot c_{j,\infty}}} = \lambda \cdot \sqrt{\frac{4 \cdot z_j \cdot e \cdot \Delta\phi_0}{k \cdot T}}. \quad (2.28)$$

Combining equations 2.19 and 2.27, one can derive the concentration profiles for the defects in the space charge layer in the Mott-Schottky case to be defined by

$$c_j(x) = c_{j,\infty} \cdot \exp\left[-z_j \left(\frac{x - \lambda^*}{2\lambda}\right)^2\right]. \quad (2.29)$$

Since the space charge layers on both sides of the grain boundary together compensate the core charge, the core charge density according to the Mott-Schottky model is given by [5]

$$Q_{core} = 2 \cdot e \cdot c_{j,\infty} \cdot \lambda^* = \sqrt{8 \cdot \varepsilon_0 \cdot \varepsilon_r \cdot e \cdot c_{j,\infty} \cdot \Delta\phi_0}. \quad (2.30)$$

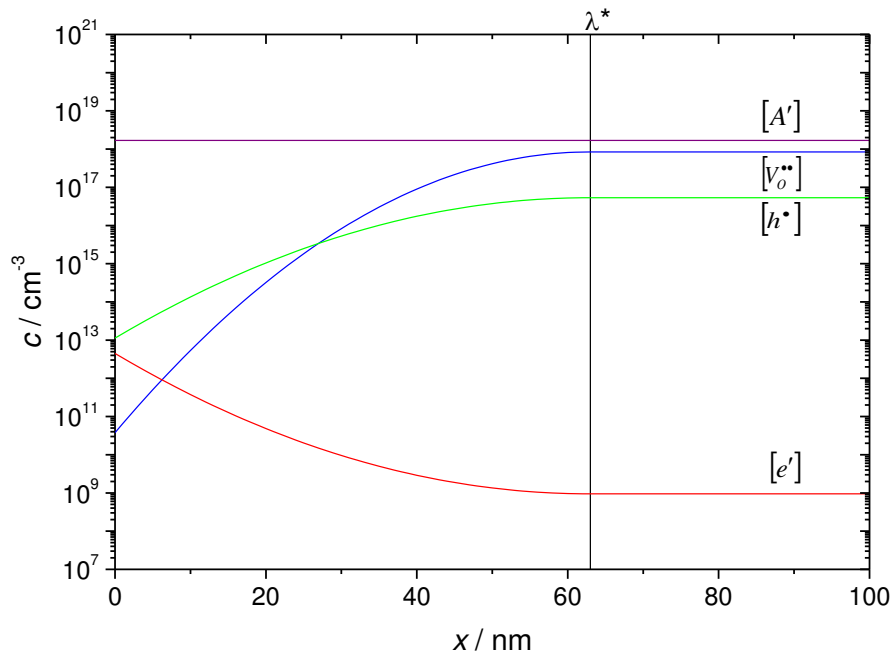


Figure 4: Space charge layer profiles for a microcrystalline slightly acceptor doped SrTiO₃ ceramic according to the Mott-Schottky model ($T = 550^\circ\text{C}$, $pO_2 = 1\text{bar}$, 100 ppm acceptors, $\Delta\phi_0 = 0.6\text{V}$).

The space charge layer profiles for a microcrystalline SrTiO₃ ceramic according to the Mott-Schottky model are exemplarily depicted in Figure 4. Comparing the Mott-Schottky with the Gouy-Chapman model, one notices that in the former the extension of the space

charge layer depends on the space charge potential, since the majority defect cannot redistribute. Consequently the space charge layer width is larger in the Mott-Schottky case compared to the Gouy-Chapman case, in which a stronger charge screening occurs.

2.3.3 Space charge layers in a mesoscopic situation

So far the charge carrier redistribution at a grain boundary was only treated for microcrystalline samples in which the grains are so large, that adjacent to the space charge layers there still remains a large portion of unperturbed bulk. However, if the grain size is reduced below $2\lambda^*$ the space charge layers overlap and the charge carrier concentrations are altered throughout the whole grain (compared to the virtual bulk concentrations), which is referred to as a mesoscopic situation [1]. As mentioned before, the charge carrier profiles for SrTiO₃ in this study are best approximated by the Mott-Schottky model, therefore the calculations for the mesoscopic case will be conducted following the basic ideas of the Mott-Schottky model that were introduced for the microcrystalline case. Again the simplified version of equation 2.20 has to be integrated, this time using the suitable boundary conditions for the mesoscopic case [26]

$$\begin{aligned}\phi(0) &= \phi(d_g) = \phi_0 \\ \phi'(d_g/2) &= 0,\end{aligned}\tag{2.31}$$

with d_g being the grain size. This yields the variation of the electrostatic potential in the mesoscopic case, defined as

$$\Delta\phi(x) = -\frac{k \cdot T}{4 \cdot z_j \cdot e \cdot \lambda^2} \left(x^2 - d_g \cdot x + \lambda^{*2} \right).\tag{2.32}$$

Note that the space charge layer width enters in equation 2.32 during integration, through the term $\Delta\phi_0$, which can be taken from the calculations for the microcrystalline case, since the potential at the grain boundary core is assumed to be the same. Combining the expression for the electrostatic potential in the mesoscopic case with equation 2.19 gives the concentration profiles for the charge carriers in the mesoscopic case:

$$c_j(x) = c_{j,\infty} \cdot \exp \left[-\frac{z_j}{4 \cdot \lambda^2} \left(x^2 - d_g \cdot x + \lambda^{*2} \right) \right].\tag{2.33}$$

Comparison of the space charge layers in a microcrystalline SrTiO₃ sample with those in a nanocrystalline one with a grain size of 50nm (see Figure 5) clearly shows, that in the latter

case the profiles are much less bent and can therefore be approximated by completely flat profiles, assuming the concentrations directly at the core throughout the whole grain.

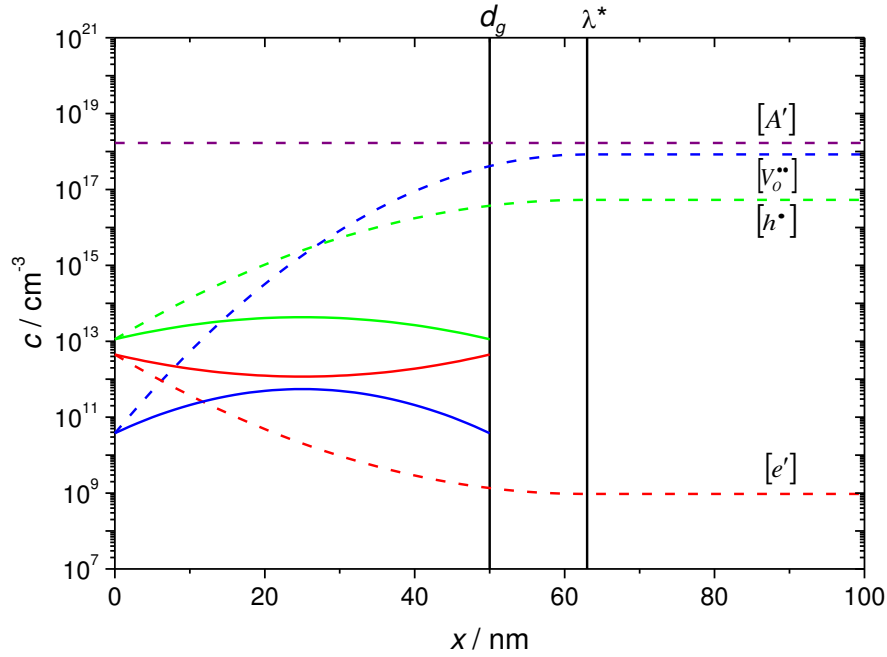


Figure 5: Comparison of the space charge layer profiles for a microcrystalline (dashed lines) and a nanocrystalline (solid lines, $d_g = 50\text{nm}$) slightly acceptor doped SrTiO_3 ceramic calculated by the Mott-Schottky model ($T = 550^\circ\text{C}$, $p\text{O}_2 = 1\text{bar}$, 100 ppm acceptors, $\Delta\phi_0 = 0.6\text{V}$).

2.4 The brick layer model

The brick layer model is a widely used tool to evaluate the impedance response of polycrystalline materials. According to this model, a polycrystalline material is treated in terms of cube shaped “bricks” of equal size representing the grain cores (bulk), which are covered by a thin layer representing the grain boundaries (see Figure 6(a)) [22, 27, 28]. Depending on the specific situation, the current can flow along two possible pathways:

- (i) If the grain boundaries are very resistive it passes in series through the bulk and the blocking perpendicular grain boundaries.
- (ii) If the grain boundaries are highly conductive the current preferably flows along them.

In the case of SrTiO_3 , this depends on whether the majority mobile charge carriers are holes, oxygen vacancies or electrons, i.e. on the oxygen partial pressure as it is explained in chapter 2.2. Since the two majority mobile charge carriers under oxidizing conditions (holes and oxygen vacancies) are depleted in the space charge layers adjacent to the grain boundaries, the electric current consequently follows path (i) in this oxygen partial pressure range. Thus, both a signal from the blocking perpendicular boundaries as well as the bulk are typically recorded

during the impedance spectroscopy analysis (cf. Figure 6 (b) and (c); more details on impedance spectroscopy will be presented in the subsequent chapter 3.2.1). At very low oxygen partial pressures n-type conductivity dominates. Since electrons are accumulated in the space charge layers, the preferred pathway for the n-type transport is therefore along the parallel grain boundaries (path (ii)). Consequently only the response from the parallel boundaries can be seen in the impedance spectrum.

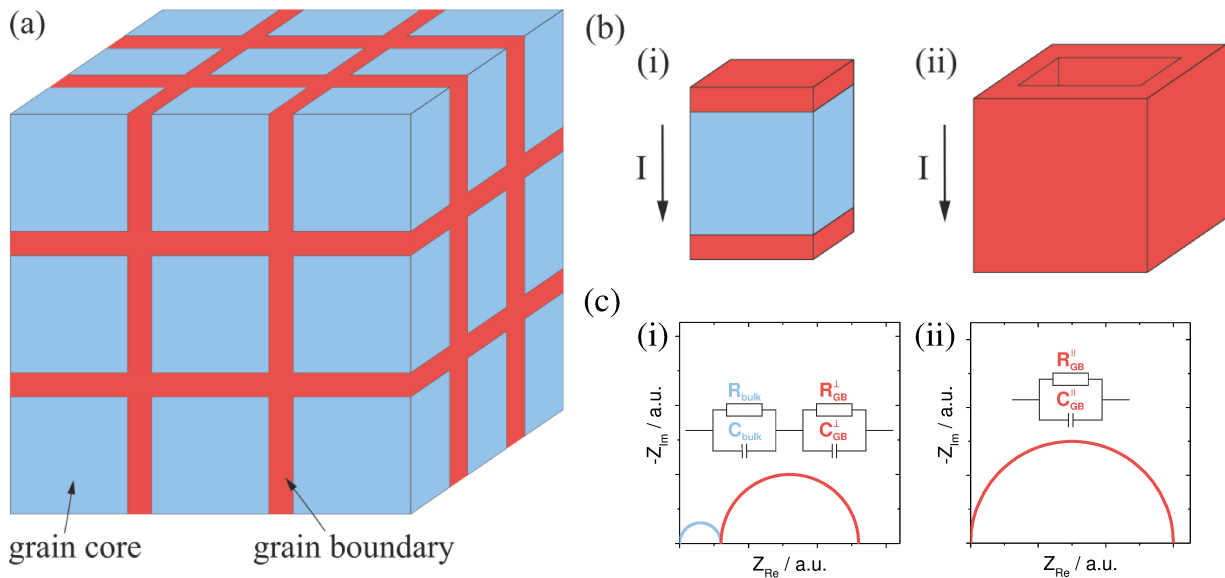


Figure 6: (a) Sketch of a polycrystalline material according to the brick layer model (note that the thickness of the grain boundary layers is not meant to be proportional to the size of the grain core); (b) possible pathways for the electric current: (i) in series through the grain boundaries and the bulk, (ii) along the grain boundaries; (c) corresponding impedance spectra with matching equivalent circuits for the two cases (i) and (ii) in (b) (sketches inspired by [3] and [29]).

2.5 Considerations on calculations of the electrical conductivity

By employing impedance spectroscopy one can determine values of the electrical resistance and capacitance associated with the different contributions in the spectrum, which stem from different loci of the sample. Such information allows for the calculation of the electrical conductivity and the relative permittivity of bulk and grain boundaries by considering the thickness l and the cross section area A of the sample:

$$\sigma_{bulk} = \frac{l}{R_{bulk} \cdot A} \quad (2.34)$$

$$\sigma_{GB} = \frac{l}{R_{GB} \cdot A} \quad (2.35)$$

$$\varepsilon_{bulk} = \frac{C_{bulk} \cdot l}{\varepsilon_0 \cdot A} \quad (2.36)$$

$$\varepsilon_{GB} = \frac{C_{GB} \cdot l}{\varepsilon_0 \cdot A}. \quad (2.37)$$

In the depletion mode (namely, when the majority mobile charge carrier is depleted at the grain boundaries and thus the corresponding current flows perpendicularly to the grain boundaries) the specific grain boundary conductivity σ_{GB}^\perp , which is the local conductivity within the space charge region, has to be considered. Assuming a Mott-Schottky situation, σ_{GB}^\perp is related to the bulk conductivity via the space charge potential according to [30]

$$\frac{\sigma_{bulk}^\perp}{\sigma_{GB}^\perp} = \frac{\exp(ze\Delta\phi_0 / kT)}{2ze\Delta\phi_0 / kT}. \quad (2.38)$$

According to the brick layer model the capacitances of the bulk and grain boundaries are given as follows [31]:

$$C_{bulk}^\perp = \varepsilon_0 \cdot \varepsilon_{bulk} \cdot \frac{A}{N \cdot d_g} \quad (2.39)$$

$$C_{GB}^\perp = \varepsilon_0 \cdot \varepsilon_{GB} \cdot \frac{A}{N \cdot \delta} \quad (2.40)$$

with N being the number of grains that are included in a sample of thickness l and grain boundary extent δ , which is equal to $2\lambda^*$. Combination of the equations 2.39 and 2.40 gives the thickness of the grain boundary, defined as

$$\delta = \frac{C_{bulk}^\perp \cdot \varepsilon_{GB}}{C_{GB}^\perp \cdot \varepsilon_{bulk}} \cdot d_g. \quad (2.41)$$

By employing the brick layer model, the resistances of bulk and grain boundaries are given in a similar fashion as the capacitances above:

$$R_{bulk}^\perp = \frac{1}{\sigma_{bulk}^\perp} \cdot \frac{N \cdot d_g}{A} \quad (2.42)$$

$$R_{GB}^\perp = \frac{1}{\sigma_{GB}^\perp} \cdot \frac{N \cdot \delta}{A}. \quad (2.43)$$

Since the relative permittivity in the space charge layer and the bulk are basically the same [21], the equations 2.41, 2.42 and 2.43 can be combined to yield the specific grain boundary conductivity

$$\sigma_{GB}^\perp = \sigma_{bulk}^\perp \cdot \frac{C_{bulk}^\perp \cdot R_{bulk}^\perp}{C_{GB}^\perp \cdot R_{GB}^\perp}. \quad (2.44)$$

Since the activation energy of the specific grain boundary conductivity is defined as [32]

$$\Delta E_{GB}^{\perp} = -\frac{\partial \ln \sigma_{GB}^{\perp}}{\partial (1/kT)}, \quad (2.45)$$

it can be derived, by performing the derivation on equation 2.38, to be

$$\Delta E_{GB}^{\perp} = \Delta E_{bulk}^{\perp} + e\Delta\phi_0 - kT + \frac{\partial \Delta\phi_0}{\partial (1/kT)} \left(\frac{e}{kT} - \frac{1}{\Delta\phi_0} \right). \quad (2.46)$$

Besides the temperature dependence of the conductivity also the dependence on the oxygen partial pressure is of importance. According to equation 2.14 the bulk conductivity under oxidizing conditions is predominantly p-type and thus can be written as $\sigma_{bulk}^{\perp}(T, pO_2) = e \cdot p(T, pO_2) \cdot u_p(T)$. Here only the hole concentration depends on the oxygen partial pressure and therefore, by employing equation 2.10, the pO_2 -dependence of the p-type bulk conductivity is formulated as

$$\frac{\partial \text{Log } \sigma_{bulk}^{\perp}}{\partial \text{Log } pO_2} = \frac{1}{4} + \frac{1}{2} \frac{\partial \text{Log } m}{\partial \text{Log } pO_2}. \quad (2.47)$$

As long as the impurities are not redox active the second term in equation 2.47 is zero and the typical $1/4$ dependence for p-type conductivity in SrTiO_3 results. The pO_2 -dependence of the n-type conductivity under reducing conditions can be derived accordingly, based on $\sigma_{bulk}^{\parallel}(T, pO_2) = e \cdot n(T, pO_2) \cdot u_n(T)$ and equation 2.13:

$$\frac{\partial \text{Log } \sigma_{bulk}^{\parallel}}{\partial \text{Log } pO_2} = -\frac{1}{4} - \frac{1}{2} \frac{\partial \text{Log } m}{\partial \text{Log } pO_2}. \quad (2.48)$$

For the pO_2 -dependence of the grain boundary conductivity the space charge potential has to be taken into account (cf. equation 2.19). Applying the Mott-Schottky model, the pO_2 -dependence of the grain boundary conductivity across blocking grain boundaries [24] in the p-type regime is defined as

$$\frac{\partial \text{Log } \sigma_{GB}^{\perp}}{\partial \text{Log } pO_2} = \frac{1}{4} + \frac{\partial \text{Log } m}{\partial \text{Log } pO_2} + \frac{1}{2} \frac{\partial \text{Log } \Delta\phi_0}{\partial \text{Log } pO_2} - \frac{1}{2.303} \frac{\partial (e\Delta\phi_0 / kT)}{\partial \text{Log } pO_2}. \quad (2.49)$$

In equation 2.49 the term $(\partial \text{Log } \Delta\phi_0 / \partial \text{Log } pO_2) = (\partial \Delta\phi_0 / \partial \text{Log } pO_2) / \Delta\phi_0$ can be neglected compared to $(\partial \Delta\phi_0 / \partial \text{Log } pO_2) / (kT/e)$ since $|\Delta\phi_0| \gg (kT/e)$ and the simplified form results:

$$\frac{\partial \text{Log } \sigma_{GB}^{\perp}}{\partial \text{Log } pO_2} \approx \frac{1}{4} + \frac{\partial \text{Log } m}{\partial \text{Log } pO_2} - \frac{1}{2.303} \frac{\partial (e\Delta\phi_0 / kT)}{\partial \text{Log } pO_2}. \quad (2.50)$$

Under reducing conditions in the n-type regime the parallel boundaries control the conductivity. At such low oxygen partial pressures the variation of m can be neglected since basically all Fe atoms are ionized and the pO_2 -dependence of the parallel grain boundary conductivity [24] in the n-type regime is thus

$$\frac{\partial \text{Log} \sigma_{GB}^{\parallel}}{\partial \text{Log} pO_2} \approx -\frac{1}{4} + \frac{1}{2.303} \frac{\partial(e\Delta\phi_0/kT)}{\partial \text{Log} pO_2}. \quad (2.51)$$

Furthermore the pO_2 -dependence of the grain boundary conductivity can also be related to the grain boundary core charge density. In the Mott-Schottky approximation combination of the equations 2.30 and 2.50 yields

$$\frac{\partial \text{Log} \sigma_{GB}^{\perp}}{\partial \text{Log} pO_2} \approx \frac{1}{4} + \frac{\partial \text{Log} m}{\partial \text{Log} pO_2} - \frac{1}{18.4\epsilon_0\epsilon_r kT} \cdot \left[\left(\frac{\partial Q_{core}}{\partial \text{Log} pO_2} \cdot \frac{2Q_{core}}{m} \right) - \left(\frac{\partial m}{\partial \text{Log} pO_2} \cdot \left(\frac{Q_{core}}{m} \right)^2 \right) \right] \quad (2.52)$$

In the case of parallel grain boundaries the core charge density can be included in the same manner and equation 2.51 then becomes

$$\frac{\partial \text{Log} \sigma_{GB}^{\parallel}}{\partial \text{Log} pO_2} \approx -\frac{1}{4} + \frac{2Q_{core}}{18.4\epsilon_0\epsilon_r m kT} \cdot \frac{\partial Q_{core}}{\partial \text{Log} pO_2}. \quad (2.53)$$

It is important to note, that the dependencies of the grain boundary conductivity on the oxygen partial pressure derived above also apply in the mesoscopic case.

As far as the conductivity of a sample is regarded, the point (in terms of oxygen partial pressure) at which the transition between n-type and p-type conductivity occurs (i.e. the minimum of the overall electronic conductivity, see Figure 2 (b)) allows to gather some important pieces of information. At this point n-type and p-type conductivity are equal and therefore it holds that

$$\sigma_{min} = e \cdot n \cdot u_n = e \cdot p \cdot u_p. \quad (2.54)$$

Combination with the mass action equation for the band-band transfer (2.4) yields the conductivity at the minimum, defined as

$$\sigma_{min} = e \sqrt{u_n \cdot u_p \cdot K_B}. \quad (2.55)$$

It is interesting to note that, as long as the mobilities of electrons and holes are assumed to stay constant for different SrTiO_3 samples (for example for microcrystalline vs. nanocrystalline), the position of the conductivity minimum can then only be altered by a

possible variation of the band gap with the size of the samples. Another important aspect to consider is that equation 2.55 is also valid in the mesoscopic case.

By considering the charge carrier concentration profiles according to the space charge model, equation 2.19 can be rewritten and the profiles for electrons, holes and oxygen vacancies are then given by

$$n(x) = n_{\infty} \cdot \kappa(x) \quad (2.56)$$

$$p(x) = p_{\infty} \cdot [\kappa(x)]^{-1} \quad (2.57)$$

$$v(x) = v_{\infty} \cdot [\kappa(x)]^{-2}, \quad (2.58)$$

with $\kappa(x) = \exp(e \cdot \Delta\phi(x) / k \cdot T)$. The oxygen partial pressure at which the minimum of the electronic conductivity occurs can be derived by combining the equations for the mass action law of the band-band transfer (2.4), the mass action law of the oxygen incorporation reaction (2.8), the simplified electroneutrality condition (2.9), the equation that follows from the equality of p-type and n-type conductivity at the minimum (2.54) and the oxygen vacancy concentration profile (2.58):

$$pO_{2,min}(x) = \left(\frac{K_B}{K_{Ox}} \right)^2 \cdot \left(\frac{u_n}{u_p} \right)^2 \cdot \frac{1}{m^2} \cdot [\kappa(x)]^4. \quad (2.59)$$

For the bulk electronic conductivity it follows that the conductivity at the minimum is

$$pO_{2,min,bulk} = pO_{2,min}(x \rightarrow \infty) = \left(\frac{K_B}{K_{Ox}} \right)^2 \cdot \left(\frac{u_n}{u_p} \right)^2 \cdot \frac{1}{m^2}. \quad (2.60)$$

All the equations in this chapter are applicable to microcrystalline samples, for which one can clearly differentiate between bulk and grain boundaries. In nanocrystalline samples, with sufficiently small grains, a mesoscopic situation can be encountered because of the overlap of the space charge zones and the relevant equations above are modified accordingly. Since for the mesoscopic case flat concentration profiles can be assumed throughout the grains, equation 2.38 can be simplified to [3]

$$\frac{\sigma_{meso}^{\perp}}{\sigma_{bulk}^{\perp}} = \exp(-ze\Delta\phi_0 / kT). \quad (2.61)$$

The activation energy for the conductivity in the depletion mode for the mesoscopic case then follows to be defined as

$$\Delta E_{meso}^{\perp} = \Delta E_{bulk}^{\perp} + e\Delta\phi_0 + \frac{e}{kT} \cdot \frac{\partial\Delta\phi_0}{\partial(1/kT)}. \quad (2.62)$$

Furthermore, since the charge carrier concentrations within the grain can be approximated by those at the grain boundary core, the oxygen partial pressure at which the minimum of the electronic conductivity occurs results to be defined by

$$pO_{2,min,meso} = pO_{2,min}(x \rightarrow 0) = \left(\frac{K_B}{K_{Ox}}\right)^2 \cdot \left(\frac{u_n}{u_p}\right)^2 \cdot \frac{1}{m^2} \cdot \kappa_0^4 \quad (2.63)$$

in the mesoscopic case. The ratio of the oxygen partial pressures at the minima of the electronic conductivity in the microcrystalline and the mesoscopic case,

$$\frac{pO_{2,min,meso}}{pO_{2,min,bulk}} = \kappa_0^4 = \left[\exp(e \cdot \Delta\phi_0 / k \cdot T)\right]^4 \quad (2.64)$$

thus allows for the determination of the space charge potential of the nanocrystalline mesoscopic sample. Here it is assumed that the mass action equations for the band-band transfer and the oxygen incorporation, as well as the mobilities of electrons and holes do not differ between the microcrystalline and the nanocrystalline sample.

2.6 Classification of grain boundaries

In the previous chapters, grain boundaries were treated from an electrochemical perspective, which means that the term “grain boundary” refers to the space charge layers on either side of the grain boundary core, in which rearrangement of the mobile charge carriers occurs. Yet, from a crystallographic perspective, the term “grain boundary” relates to the boundary plane in the core and its atomistic description. This chapter is intended to give some more information on the latter point of view.

In a solid crystalline material a grain boundary separates two adjacent grains of the same phase but different orientations. Within the grain boundary the atoms are displaced compared to their regular lattice positions in the bulk of the material in order to accommodate the misorientation between the grains. This misorientation can be described via a rotation around a common rotation axis by the angle θ . Depending on the relative orientations of the rotation axis and the grain boundary normal it is possible to distinguish between tilt grain boundaries (the two axes lie perpendicular to each other) and twist grain boundaries (the two axes lie

parallel to each other). Any grain boundaries that are not included in those two descriptions are summarized as mixed grain boundaries. [33]

According to their actual atomic structure, grain boundaries can be further separated, depending on the value of the boundary angle θ , into low-angle grain boundaries (LAGBs) and high-angle grain boundaries (HAGBs). LAGBs can be described by a periodic array of stacked dislocations along the boundary plane, with edge dislocations forming a tilt grain boundary and screw dislocations a twist grain boundary. Their structure and properties are a function of the misorientation angle θ . With increasing boundary angle the dislocation spacing needs to be further and further reduced until the dislocations begin to overlap and the dislocation model cannot be applied anymore. This point is reached for an angle $\theta \approx 13^\circ - 15^\circ$ [34], which marks the transition to HAGBs. The energy of HAGBs is generally independent of the misorientation angle, but at particular orientations so called singular grain boundaries exist, whose interfacial energy is markedly reduced. The HAGBs with a high interfacial energy are called general, whereas those lying in the energetic transition region between singular and general HAGBs are called vicinal [35].

In order to describe the singular HAGBs the so called coincidence-site lattice model (CSL) has been developed by Kronberg and Wilson in 1949 [36]. It is based on the idea that the grain boundary energy is lower, the more atomic positions along the grain boundary coincide for the two adjacent grains. If the crystal lattices of the two neighboring grains are extended into each other, a certain number of atomic positions will coincide. Those coincidence sites form a superlattice, whose elementary cell volume can be related to that of the crystal lattice, to give the degree of fit Σ of the two grains:

$$\Sigma = \frac{V(\text{elementary cell CSL})}{V(\text{elementary cell crystal lattice})}. \quad (2.65)$$

Another possibility to visualize the degree of fit is to compare the total number of atomic sites along the grain boundary with the number of coincidence sites along the grain boundary, e.g. for $\Sigma = 5$ every fifth atomic position is shared between the two grains.

3 Experimental methods

3.1 Sample preparation

3.1.1 Spark plasma sintering (SPS)

Spark plasma sintering (SPS) strongly emerged as a powerful and fast sintering technique over the last two decades [37]. It differs from conventional sintering in the way the heat is applied. For conventional sintering the radiation from a surrounding furnace heats up the green body. By spark plasma sintering DC pulses are passed through the compacted powder itself/a graphite mold, depending on whether the powder is conductive/nonconductive, which enables local Joule heating. Combined with the simultaneous application of an uniaxial load this enables lower sintering temperatures, fast heating and cooling rates as well as shorter holding times, while still achieving high densities [38]. These properties make this technique perfectly suited for the fabrication of nanocrystalline materials in which one wants to limit the grain growth [39].

In this work the HP D 5 spark plasma sintering machine from FCT Systems GmbH was used. In the standard setup a 30 mm graphite die with graphite pistons is placed in a vacuum chamber in between two steel pistons which apply the uniaxial load. For the fabrication of the nanostructured SrTiO₃ ceramics this setup was slightly modified. In order to increase the pressure onto the compacted powder a second die with 5 mm inner diameter was inserted into the 30 mm die. Since the standard graphite parts can only withstand pressures up to 60 - 80 MPa the 5 mm pistons were made out of SiC and for the protection of the graphite pistons tungsten carbide discs were placed in between the SiC and graphite pistons. The temperature was controlled by a thermocouple inserted in the middle of the 30 mm graphite die.

The sintering conditions for the nanocrystalline samples in this work were 850°C, holding time of 5 minutes, heating rate of 100K/min, whereas for the cooling the current was completely shut off, applied pressure of 380 MPa, all performed under Ar atmosphere. The pulsed DC patterns were composed by a sequence of 12 pulses (3 ms each) with a break of 3 ms between each sequence.

3.1.2 Grain boundary decoration

The SrTiO₃ powder employed for all polycrystalline samples in this work was supplied by Inframat Advanced Materials (Lot: IAM12308NSTO). The Rb decoration of the powder surface prior to sintering is achieved by a solution and precipitation method. First RbNO₃ (Alfa Aesar, 99.8%, metals basis, Lot:D18N40) was dissolved in bidistilled water, then the SrTiO₃ powder was added and the mixture thoroughly stirred for two hours by a magnetic stirrer. Afterwards the water was slowly removed in a rotary evaporator. By thermogravimetric analysis the necessary temperature for removal of the nitrate groups was determined and subsequently the powder was calcined under N₂ atmosphere at 550°C for 5 hours. Two Rb decoration contents, namely 3at% (which equals roughly a 25% coverage of the SrTiO₃ surface by Rb ions) and 5.5at% Rb (which equals roughly a 50% coverage of the SrTiO₃ surface by Rb ions) were chosen.

3.1.3 Bicrystal fabrication

For the fabrication of bicrystals by spark plasma sintering a graphite disc (diameter = 30 mm and thickness = 0.7 mm) with a quadratic cutout in the middle was used to keep the single crystals in place in between the graphite pistons during the sintering. Prior to sintering the single crystals were successively cleaned in an ultrasonic bath with acetone and ethanol. During the phase of determining the optimal sintering parameters for the SrTiO₃ bicrystals single crystals of various orientations supplied by CrysTec GmbH were used. The sintering temperatures ranged from 800°C to 1200°C with a holding time of 5 minutes, a heating rate of 100K/min and a cooling rate of 50K/min down to 450°C, then the current was shut off. For the applied pressure 25 MPa up to 130 MPa were tested and the sintering atmosphere was always Ar. The DC pulse pattern that was used is described in section 3.1.1. After spark plasma sintering the sample was oxidized in air at 700°C for 5 hours, which also burnt the graphite which adhered to the bicrystal during sintering. Then the quality of the bond was determined on the basis of visible Newton rings indicating air inclusions and a bonded part was cut out for the electrical characterization. The last step was done in the crystal preparation service group of the MPI for Solid State Research.

For the series production of SrTiO₃ bicrystals 10 mm x 10mm x 0.5mm, both side polished (111) and (510) oriented single crystals were purchased from SurfaceNet GmbH. As far as possible the single crystals were cut from one larger single crystal boule to ensure a constant impurity content. The spark plasma sintering parameters of these specifically oriented bicrystals were set to 1200°C, 5 minutes holding time, heating rate 100K/min, cooling rate

50K/min down to 450°C, then the current is shut off, 25 MPa and Ar atmosphere. The DC pulse pattern was the one described in section 3.1.1.

The Rb decoration of SrTiO₃ bicrystals was performed by coating one of the two single crystals with a solution of RbNO₃ (Alfa Aesar, 99.8%, metals basis, Lot:D18N40) in bidistilled water prior to sintering. For this purpose the SrTiO₃ surface was rendered hydrophilic by illumination with an UV lamp at 120 mW/cm² for 2 hours, to ensure an even wettability of the surface. After application of the RbNO₃ solution the water was slowly evaporated on a hot plate. Subsequently the decorated single crystal was calcined in N₂ atmosphere for 5 hours. Two decoration contents were chosen. On the one hand a 25% coverage by Rb ions which is exactly half of the coverage in the 3at% Rb decorated nanocrystalline SrTiO₃ since for the nanocrystalline ceramic during sintering two surfaces covered with 25% Rb ions come into contact. On the other hand a coverage of 250%, which should ensure an extremely high Rb concentration introduced at the grain boundary.

3.2 Characterization techniques

3.2.1 Electrochemical impedance spectroscopy (EIS)

Electrochemical impedance spectroscopy (EIS) is a powerful method to differentiate the electrical properties of bulk, grain boundaries and the electrode in a polycrystalline electrically conductive material. In EIS an alternating voltage is applied across the sample and the resulting current is recorded as a function of the angular frequency ω . The impedance of a sample is a complex function defined as

$$Z(j\omega) = Z' + jZ'' . \quad (3.1)$$

By plotting the real part Z' on the x-axis against the imaginary part Z'' on the y-axis one can construct the so called Nyquist plot, which displays a semicircle. This semicircle can be fitted by an equivalent circuit consisting of a resistor R connected in parallel with a capacitor C . In the Nyquist plot two extreme situations deserve a separate examination: For $\omega \rightarrow 0$ one reaches the intercept of the semicircle with the x-axis, which marks the total resistance of the sample and the DC resistance is obtained. For very high frequencies the impedance approaches zero and the origin of the Nyquist plot is reached. In this situation the resistors are short-circuited by the highly permeable capacitors. The frequency at the peak of the semicircle ω_{max} is related to the time constant of the process according to

$$\tau_{max} = (RC)_{max} = \omega_{max}^{-1} . \quad (3.2)$$

As long as the relaxation times of certain different physical processes in a material are sufficiently different, e.g. $\tau_{bulk} < \tau_{GB} < \tau_{electrode}$, one can distinguish them as different semicircles in the Nyquist plot. It is important to keep in mind that the experimentally observed semicircles, especially those associated with grain boundaries, are often non ideal and therefore depressed. This results from inhomogeneity in the material that cause a non-uniform current distribution. Consequently in order to achieve a good agreement of the fit with the measured data the ideal capacitors have in such cases to be replaced by the so called constant phase element Q . For the constant phase element the capacitance is defined as [40]

$$C = \left(R^{1-\alpha} Q \right)^{\frac{1}{\alpha}}, \quad (3.3)$$

where α is the ideality factor that describes the degree of depression of the semicircle. In order to achieve a sensible fit the ideality factor has to range between 1, representing an ideal capacitor and 0.7.

Impedance spectra in this work were obtained using an Alpha-A high resolution dielectric analyzer (Novocontrol). For the nanocrystalline SrTiO₃ ceramics the applied AC voltage was 0.1 V, whereas for the SrTiO₃ bicrystals an AC voltage of 0.05 V was applied. In both cases the frequency range of 1 MHz down to 1 Hz was covered. In order to enable the measurement of several samples the single channel of the Novocontrol instrument was split up into four channels by a home built multiplexer.

For the electrical characterization by impedance spectroscopy electrodes were applied to both of the large side faces of the samples. For the nanocrystalline ceramics sputtered Pt electrodes were used, whereas for the bicrystal YBCO electrodes deposited by pulsed laser deposition were employed (deposition performed by Benjamin Stuhlhofer, MPI for Solid State Research). Such electrodes basically eliminate electrode effects from the impedance spectra [4]. In this way a possible overlap of electrode and grain boundary impedance semicircle in a bicrystal (as it could be encountered with sputtered Pt electrodes) is prevented.

Activation energies of the samples under pure oxygen atmosphere were determined by temperature dependence measurements in the range of 550°C to 450°C for the nanocrystalline ceramics and from 500°C to 400°C for the bicrystals. For the determination of the oxygen partial pressure dependence of the conductivity oxygen partial pressures from 1 bar down to ca. 10⁻⁵ bar were achieved by mixtures of pure O₂, 1000 ppm O₂ in N₂ and nominally pure N₂. To cover oxygen partial pressures in the range of 10⁻²¹ bar to 10⁻²⁵ bar CO-CO₂ mixtures were employed. The impedance spectrum at each temperature and oxygen partial pressure was

recorded every 2 hours until the overlap of several consecutively recorded spectra ensured that equilibrium was reached.

The analysis of the impedance spectra was conducted with the software Z-View (Scribner Associates, Version 3.3c).

3.2.2 X-ray diffraction (XRD)

X-ray diffraction (XRD) was employed on the SrTiO₃ powders as well as on sintered pellets in order to determine the phase purity and exclude possible Rb phases in the decorated compositions. Furthermore the characterization of the Rb decorated powders before and after the calcination served as a tool to track the removal of the nitrate groups. Measurements were performed with Cu K_α radiation in Bragg-Brentano geometry with an Empyrean diffractometer equipped with a PIXcel3D detector (PANalytical, Netherlands). The measurements were performed by Helga Hoier (MPI for Solid State Research). Some XRD measurements during the early phase of this thesis were done on an older instrument (PW 3710, Philips, Netherlands) by Gabi Götz (MPI for Solid State Research).

3.2.3 Electron microscopy

Electron microscopy was mainly employed for the characterization of the nanocrystalline SrTiO₃ pellets.

Scanning electron microscopy (SEM) with a thermal field emission gun (Merlin, Zeiss) was used to analyze the microstructure of the pellets regarding their grain size and density. These measurements were performed by Annette Fuchs (MPI for Solid State Research).

Transmission electron microscopy (TEM) with energy dispersive x-ray spectroscopy (EDX) was employed to investigate the positioning of Rb at the grain boundary core and possible diffusion into the grain. For this a part from the center of the nanocrystalline pellet was prepared by the Tripod method (Allied Multiprep Polishing System) and subsequent ion milling (Pips Gretel). The sample preparation for the TEM measurements was done by Ute Salzberger (MPI for Solid State Research), whereas the actual TEM measurement was performed by Wilfried Sigle (MPI for Solid State Research).

3.2.4 Inductively coupled plasma-optical emission spectrometry (ICP-OES) and Atomic absorption spectroscopy (AAS)

Inductively coupled plasma-optical emission spectrometry (ICP-OES) and atomic absorption spectroscopy (AAS) were employed for several purposes: The determination of the Sr/Ti ratio and the impurity content of the undoped SrTiO₃ starting powder. Furthermore the chemical analysis was used to ensure that no essential Rb loss occurs in the decorated powders during the calcination process by characterization of the powder before and after calcination. In addition ICP-OES was employed to determine the impurity content of the SrTiO₃ single crystals used for the bicrystal fabrication. For all measurements the samples were solubilized by different amounts of HCl, HNO₃ and HF depending on the exact sample type. The AAS measurements were performed on a “contrAA 300” system from analytik Jena, whereas the ICP-OES measurements were carried out on a Spectro Ciros CCD, Spectro Analytical Instruments, Germany. All the measurements described above were done by the analytical chemistry laboratory of the Max Planck Institute for Intelligent Systems (Samir Hammoud, Gerhard Werner).

To ensure the successful decoration of the SrTiO₃ single crystals with Rb prior to sintering several test samples with various Rb contents were produced which were then analyzed by ICP-OES (Vista Pro, Varian) in a department at the MPI for Solid State Research. These measurements were carried out by Marie-Luise Schreiber.

3.2.5 Thermogravimetric analysis (TGA)

Thermogravimetric analysis (TGA - STA449, Netsch, Germany) was employed to determine the optimal temperature for the calcination of the Rb decorated SrTiO₃ powders which allowed the removal of the nitrate groups from the decoration with RbNO₃, while still avoiding unwanted grain growth. For this purpose the powders were heated from room temperature to 900°C with a rate of 10K/min in nominally pure nitrogen atmosphere. These measurements were carried out by Rotraut Merkle (MPI for Solid State Research).

3.2.6 Diffuse reflectance spectroscopy

Diffuse reflectance spectroscopy (Perkin Elmer Lambda9 with labsphere RSA-PE-19) was employed to determine the band gap of the nanocrystalline SrTiO₃ ceramics. The diffuse reflectance of the sample surface was measured in the wavelength range of 550 nm to 250 nm and compared to an ideal white standard. The measurements were carried out by Benjamin

Bruha (MPI for Solid State Research). The measured reflectance can be converted into the Kubelka-Munk function

$$F(r_{\infty}) = \frac{(1-r_{\infty})^2}{2r_{\infty}}, \quad (3.4)$$

which is a measure of the absorption of the material. Here r_{∞} is the reflectance of a layer thick enough that a further increase in thickness does not change the reflectance. By plotting $(F(r_{\infty}) \cdot h \cdot f)^{1/s}$ vs. $(h \cdot f)$ in the so called Tauc plot the band gap can be determined from the extrapolation of the linear regime of this curve onto the x-axis. The exponent s depends on the nature of the transitions and is $s = 0.5$ for direct allowed transitions, $s = 1.5$ for direct forbidden transitions, $s = 2$ for indirect allowed transitions and $s = 3$ for indirect forbidden transitions.

3.2.7 BET measurement

The surface area of the initial SrTiO₃ starting powder was determined by nitrogen adsorption-desorption (Quantachrome Autosorb-1 multipoint) in order to be able to calculate the appropriate net weight of RbNO₃ to achieve a certain coverage of the Rb decorated SrTiO₃ powders. Furthermore the characterization of the Rb decorated powders by BET before and after calcination allowed us to investigate if the SrTiO₃ particles grow during the calcination process. The BET measurements were performed by Annette Fuchs (MPI for Solid State Research).

3.2.8 Density measurement

The density of the nanocrystalline SrTiO₃ ceramics was determined in two different ways: The geometrical density of the disc-shaped specimens was determined by measuring their thickness, diameter and their weight. The geometrical density includes open porosity of the sample. The error for this measurement was calculated by error propagation assuming relative errors of the determination of the pellet's diameter by 0.1 mm and of the thickness by 0.02 mm. The uncertainty of the scales was given with 0.001 g by the manufacturer. On the other hand the density of the pellets was also determined by helium pycnometry (micromeritics AccuPyc 1330), which gives an estimate of the closed porosity. The error of this measurement was given by the manufacturer of the pycnometer to be 0.01% when the cell volume is fully occupied. The helium pycnometry measurements were performed by Annette Fuchs (MPI for Solid State Research).

4 Results and discussion

4.1 Nanocrystalline SrTiO₃

This section presents the experimental results regarding the effects of the grain boundary decoration on the electrical conductivity of nanocrystalline SrTiO₃. As indicated in chapter 3.1.2, the singly charged Rb ion was chosen for achieving an acceptor decoration by replacing part of the Sr ions at the grain boundary core only and thus reducing the intrinsic positive core charge. This should result in an increase of the p-type conductivity and reduction of the n-type conductivity in proximity of the grain boundaries.

4.1.1 Powder characterization

The decoration of the SrTiO₃ powder with RbNO₃ was carried out as described in section 3.1.2. Since the characterizations of the freshly decorated and the calcined powders yielded similar results for both Rb contents considered here, in the following only the results obtained from those powders decorated with 3at% Rb are shown.

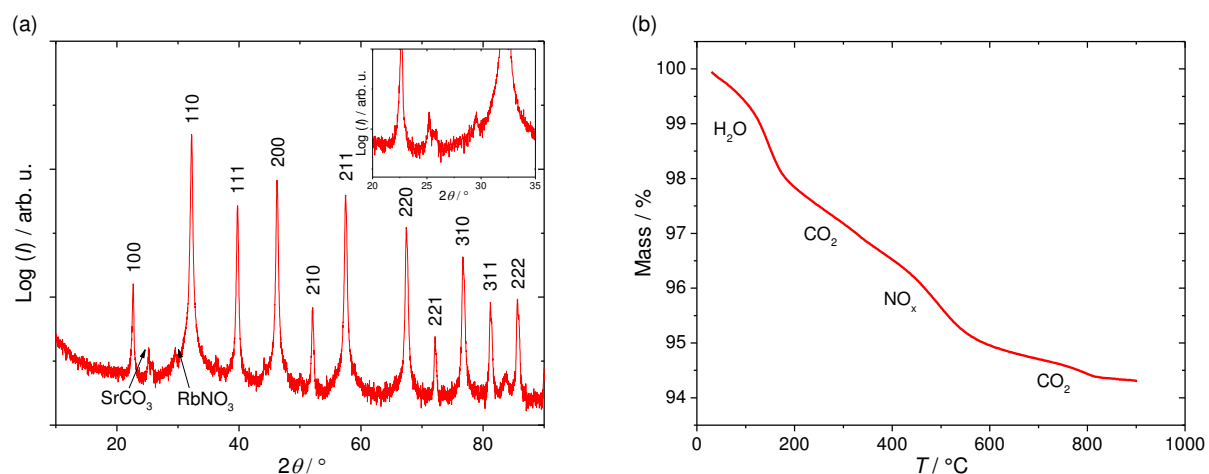


Figure 7 (a) XRD patterns of the freshly decorated SrTiO₃ powder with 3at% Rb (small inset shows more in detail the low angles range); (b) Thermogravimetric analysis of the same powder (the chemical formulas at the different mass drops indicate which gaseous species evolved).

Phase analysis of the freshly decorated powders by means of XRD showed distinct peaks of SrTiO₃, as well as two smaller peaks at lower angles, which were assigned to RbNO₃ and SrCO₃, cf. Figure 7 (a). The latter emerged as a contamination in the as-received SrTiO₃ powder according to the results of further XRD analysis. In addition this is supported by the fact, that chemical analysis of the Sr/Ti ratio in the undoped SrTiO₃ powder showed a Sr excess of roughly 4%. Since the Sr excess is most likely present as SrO in the powder, this is expected to slowly react with atmospheric CO₂ during storage in the lab, leading to the formation of SrCO₃ [41]. On the basis of thermogravimetric analysis, the temperature for

calcination in N_2 atmosphere was set to 550°C . As shown in the corresponding diagram (see Figure 7 (b)), such a temperature ensures removal of most of the nitrate and carbonate groups, while still avoiding unwanted grain growth.

The results from both XRD and thermogravimetical analysis of the calcined powders (cf. Figure 8) prove that the calcination process was successful: The peaks at low diffraction angles have vanished while during TGA only slight mass losses could be detected, as shown in Figure 8 (b) (note the different scaling of the y-axis in the TGA plot when compared to Figure 7 (b)). BET measurements performed before and after calcination indicate that there is no perceptible particle growth happening during the heat treatment. If one treats the SrTiO_3 particles as spheres, which as shown by SEM analysis is a reasonable simplification, their mean diameter determined by BET basically remains the same: 39 nm before and 41 nm after calcination. Furthermore, atomic absorption spectroscopy revealed that only minimal losses of Rb occur during the calcination process.

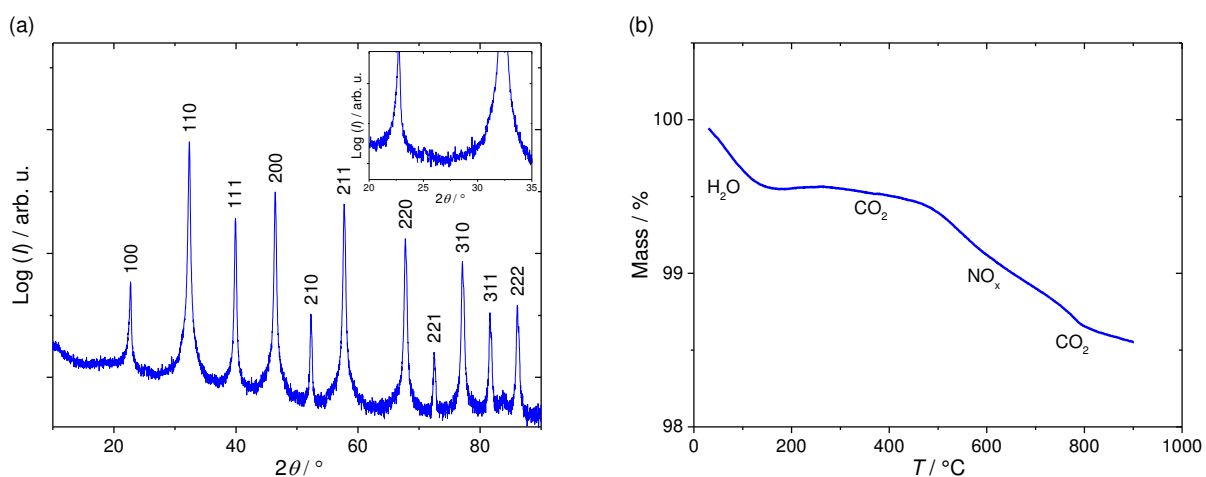


Figure 8 (a) XRD patterns of the calcined SrTiO_3 powder decorated with 3at% Rb (small inset shows more in detail the low angles range); (b) Thermogravimetical analysis of the same powder (the chemical formulas at the different mass drops indicate which gaseous species evolved). Note the different scale on the y-axis compared to Figure 7 (b).

4.1.2 Chemical analysis

Regarding the electrical conduction properties, the impurity content of the undoped SrTiO_3 powder is of great importance (cf. chapter 2.2). Therefore the abundance of the most common cations was measured by inductively coupled plasma optical emission spectrometry (ICP-OES), the results are listed in Table 4.1. The very high amount of Si is quite unexpected and it might be tracked back to a solvent dissolving some glass during the preparation of the solution for the ICP-OES analysis. But even if the Si is not an artifact of the ICP-OES preparation its presence should not affect the defect chemistry, since as a tetravalent cation it

could replace the Ti without leading to the formation of other ionic or electronic defects. The same holds for the next abundant cations Ca^{2+} and Ba^{2+} , which can substitute the also divalent Sr^{2+} . The amount of each of the remaining four cations is rather low, nevertheless the 0.004at% of Cr and 0.003at% of Fe need to be considered, since already such low impurity contents can distinctly influence the defect chemistry. Both elements can substitute Ti, resulting in a negative charge on the Ti site (when Fe and Cr are present in their +3 oxidation state) and oxygen vacancies (cf. equation 2.5).

Table 4.1 Chemical analysis of the most abundant cations in the undoped SrTiO_3 powder by ICP-OES.

Element	Percentage in the powder [wt%]	Percentage in the powder [at%]
Si	0.11	0.714
Ca	0.005	0.023
Ba	0.008	0.011
Cr	< 0.001	< 0.004
Mg	< 0.0005	< 0.004
Fe	< 0.001	< 0.003
Al	< 0.0001	< 0.001

4.1.3 Density characterization

Concerning the conductivity data also the density of the sample is an important aspect to consider, since different degrees of porosity could also lead to corresponding differences in the electrical conductivity. The resulting geometrical densities of the three samples, calculated from the mass and the geometry of the disc-shaped specimens, as well as their absolute densities, measured by helium pycnometry, are summarized in Table 4.2. Since the absolute density by helium pycnometry gives a direct measure of the closed porosity of the sample, the combination of the two densities allows for an estimation of the open porosity as well. Despite the fact that the exact same sintering conditions were employed for all the three samples, their geometrical densities differ from specimen to specimen. Based on this data it seems that the addition of rubidium, up to a certain concentration, promotes the sintering process, resulting in a higher density compared to the undoped reference sample. Since the density of the 5.5at% Rb decorated sample lies in between the densities of the other two sample types, one can assume that from a certain Rb concentration on a second process counteracts the initially beneficial presence of the Rb. Another hint towards the detrimental influence of too much Rb at the grain boundary is the fact that samples prepared from the

5.5at% Rb decorated SrTiO₃ powder sometimes broke after sintering, whereas such problems were not observed with the other two powder types.

With respect to the differences in geometrical density between the samples, it has to be kept in mind, especially regarding the interpretation of the conductivity data, that there is a rather large experimental error connected with the determination of the geometry of the samples since the specimens are not perfectly disc-shaped. From the absolute densities it is striking that the undoped and the 3at% Rb decorated SrTiO₃ show basically the same percentage of closed porosity, whereas the 5.5at% Rb decorated sample has nearly no closed porosity. In this context it is worth noting that the value of the absolute density of the 5.5at% Rb decorated SrTiO₃ sample needs to be treated with care, since a rather larger experimental error (see Table 4.2) results from the low amount of sample that was available for this measurement since most of the specimen was already used up for other characterization techniques. Furthermore it appears to be contradictory, that on the one hand the largest amount of Rb seems to deteriorate the sintering process compared to when 3at% of Rb are used, while on the other hand it seems to promote the removal of nearly all the closed porosity (which is usually a sign of effective sintering). In the light of these considerations, one can disregard the value of the absolute density of the 5.5at% Rb decorated SrTiO₃. In conclusion it thus seems that the three samples display similar percentages of closed porosity, with differing fractions of open porosity (most likely caused by the addition of Rb).

Table 4.2 Geometrical and absolute densities of the three nanocrystalline samples undoped SrTiO₃, 3at% Rb decorated SrTiO₃ and 5.5at% Rb decorated SrTiO₃.

	Geometrical density ρ_{geo} [%]	Absolute density ρ_{abs} [%]
Undoped SrTiO ₃	65.4 ± 3.4	87.9 ± 1.0
3at% Rb decorated SrTiO ₃	76.8 ± 4.3	86.8 ± 4.0
5.5at% Rb decorated SrTiO ₃	69.1 ± 4.7	97.4 ± 9.5

Such conclusions are further confirmed by pictures of the morphology of the samples taken by SEM and TEM, which are displayed in Figures 9 and 10. Especially the TEM micrographs reveal quite nicely the slightly different degrees of open porosity in the samples, already pointed out by their geometrical densities. Besides the differently pronounced intergranular porosity, the TEM micrographs also disclose the presence of intragranular porosity, which is seen in all three sample types to a similar extent (the absolute densities of undoped and 3at% Rb decorated SrTiO₃ being very close further supports this finding). In addition the electron

microscopy images allow an estimation of the average grain size, which is about 60 nm for all three sample types.

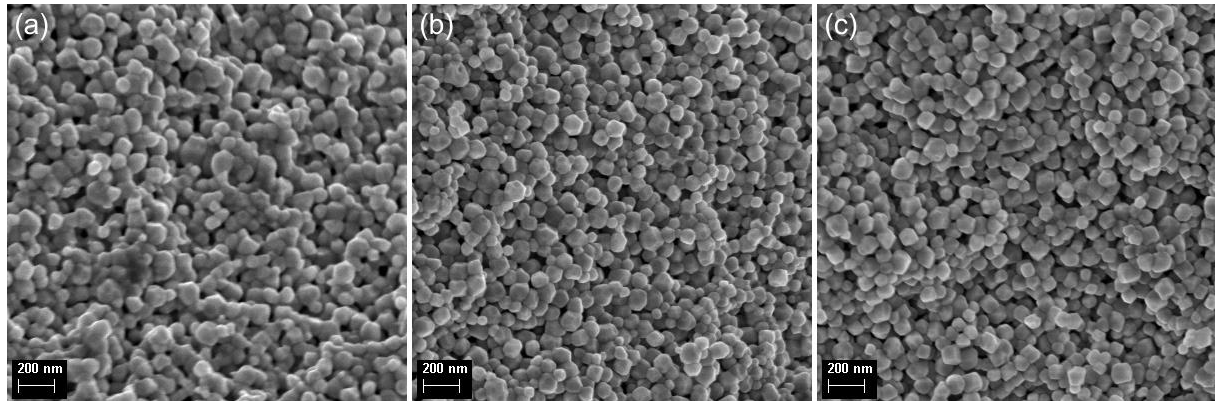


Figure 9 SEM micrographs of the nanocrystalline ceramics (a) undoped SrTiO_3 , (b) 3at% Rb decorated SrTiO_3 and (c) 5.5at% Rb decorated SrTiO_3 . All pictures were taken from freshly created fracture surfaces.

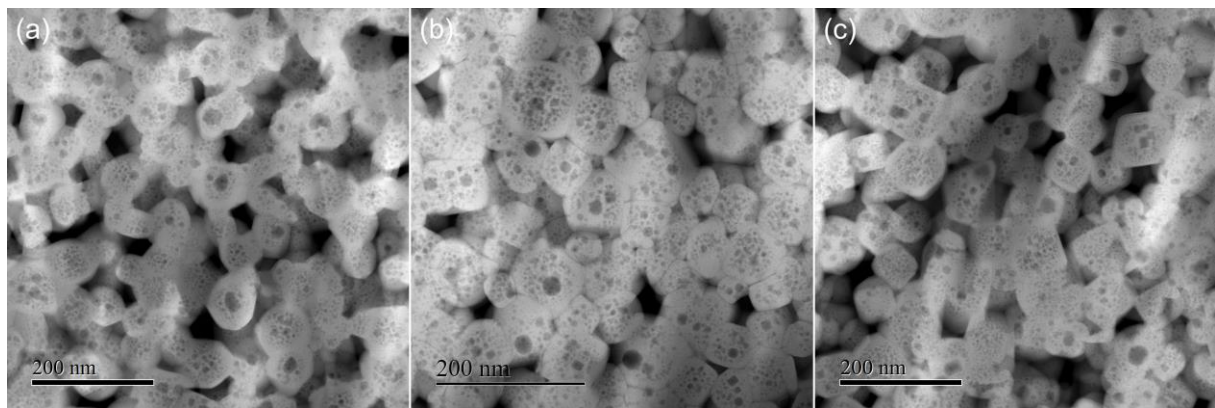


Figure 10 TEM micrographs of the nanocrystalline ceramics (a) undoped SrTiO_3 , (b) 3at% Rb decorated SrTiO_3 and (c) 5.5at% Rb decorated SrTiO_3 .

4.1.4 Impedance spectroscopy analysis

Typical impedance and modulus spectra for the three different types of nanocrystalline samples (undoped SrTiO_3 , 3at% Rb decorated SrTiO_3 and 5.5at% Rb decorated SrTiO_3), taken in pure oxygen and nominally pure nitrogen atmosphere at 550°C , are displayed in Figures 12 and 13. Under pure oxygen, both the impedance and the modulus spectra of all three sample types are characterized by one semicircle. This is in line with the expected mesoscopic situation for such nanocrystalline ceramics [1, 2]: When the average grain size falls below the value of two times the space charge layer width, the space charge zones overlap and no bulk response is present in the impedance spectra anymore (cf. chapter 2.3.3). In this way, under oxidizing conditions, one only gets a response from the blocking grain boundaries perpendicular to the path of the current. In nitrogen atmosphere (see Figure 13) the situation seems similar since for all three compositions only one semicircle is visible, both in

the impedance and modulus spectra. Note that the missing data points of the undoped SrTiO₃ spectra (at 4000 kHz, 3000 kHz and 2500 kHz) were erased from the original dataset since those were clearly due to experimental noise. They are present in all the spectra acquired in nitrogen at 550°C, occurring most probably due to some interference with the surrounding equipment. If one now takes a closer look at the impedance spectrum of the 5.5at% Rb decorated sample, one notices a shoulder at lower frequencies. Such a shoulder seems to be present, to different extents, also in the spectra of the other samples (however only under oxidizing conditions). Assuming that there are two, quite overlapping responses, the equivalent circuit used to fit those spectra consists of a connection in series of two elements comprising a resistor R connected in parallel with a constant phase element Q . This fit yields a relative dielectric constant in the range of 70 - 130 and an electrical capacitance of about 10 - 20 pF for the contribution at high frequencies, depending on the temperature, atmosphere and type of sample. Such values correspond to typical bulk properties of SrTiO₃ [7, 42]. Under oxidizing conditions conduction occurs throughout the grains and the grain boundaries lying perpendicular to the current pathway are expected to hinder the electrical conductivity. Since in a mesoscopic sample along its pathway the current only passes through space charge zones and across the grain boundaries, the electrical capacitance and relative dielectric constant characteristic of the bulk are indeed expected, as it was also demonstrated by previous studies on nanocrystalline mesoscopic SrTiO₃ [1, 2]. The activation energy of this first contribution of 1.18 eV for the undoped SrTiO₃, determined in pure oxygen atmosphere, is also in line with the available literature data [1, 2]. The activation energy of the second contribution (in the low frequency range) results to be roughly 1.5 eV for the decorated samples and 1.8 eV for the undoped SrTiO₃. This would match with impedance measurements performed on a SrTiO₃ single crystal (see the impedance spectrum in Figure 11), also equipped with sputtered Pt electrodes, where it is possible to unambiguously assign the second contribution activation energy of 1.45 eV to the electrode. However, if one considers the values of the relative dielectric constant obtained from the second contribution of the single crystal and nanocrystalline specimen, respectively, they differ by a factor of 60 to 100, depending on the specific samples. Such a discrepancy suggests that most likely the low frequency contribution is not due to the electrode. A current constriction effect resulting from the presence of residual porosity at the grain boundary could be another plausible explanation for the appearance of the extra contribution in the low frequency range of the impedance spectra. As a matter of fact, due to the low sintering temperatures employed to minimize grain growth, the samples are not fully dense (see chapter 4.1.3): The presence of

pores forces the current to deviate from the otherwise straight pathways, leading to the occurrence of an additional resistive contribution, which is visible in the impedance spectra [43-45]. Furthermore, Fleig and Maier described in their work [43] that in poorly sintered ceramics a strong overlap of the bulk semicircle and the semicircle resulting from current constriction is expected. Moreover, because of the varying thickness of the pores the semicircle due to the current constriction effect should be depressed. These two considerations regarding a current constriction effect would match with the shoulder seen on the right hand side of the impedance spectra under oxidizing conditions (see Figure 13). Nonetheless, fits with the above mentioned equivalent circuit match the data points distribution decreasingly well the more pronounced the shoulder gets (while decreasing the oxygen partial pressure from pure oxygen to nominally pure nitrogen the shoulder progressively increases) making it difficult to provide a reliable analysis of the data as a function of the oxygen partial pressure. Therefore this equivalent circuit will not be used in the upcoming data analysis since the fit does not coincide with the impedance spectra over the whole oxygen partial pressure range. It is important to note that the low frequency contribution, whether it is due to current constriction or the Pt electrodes, is actually not of importance for this work. Consequently the fit of the impedance spectra under oxidizing conditions is performed with a single RQ element and by considering only the first half (in the high frequency range) of the distorted semicircle, which unambiguously stems from the grain boundaries.

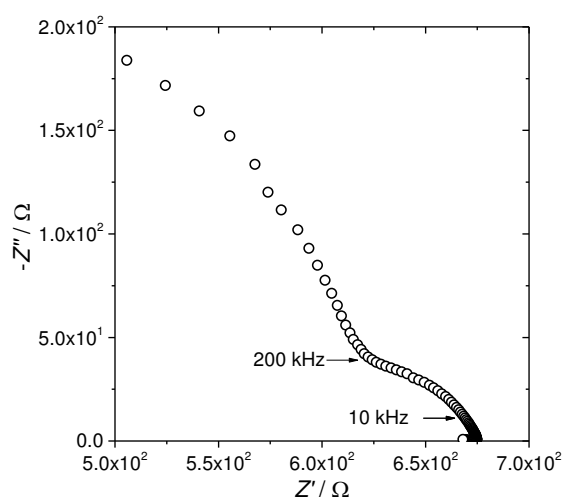


Figure 11 Impedance spectrum of a SrTiO_3 single crystal equipped with Pt electrodes collected at 545°C in pure oxygen.

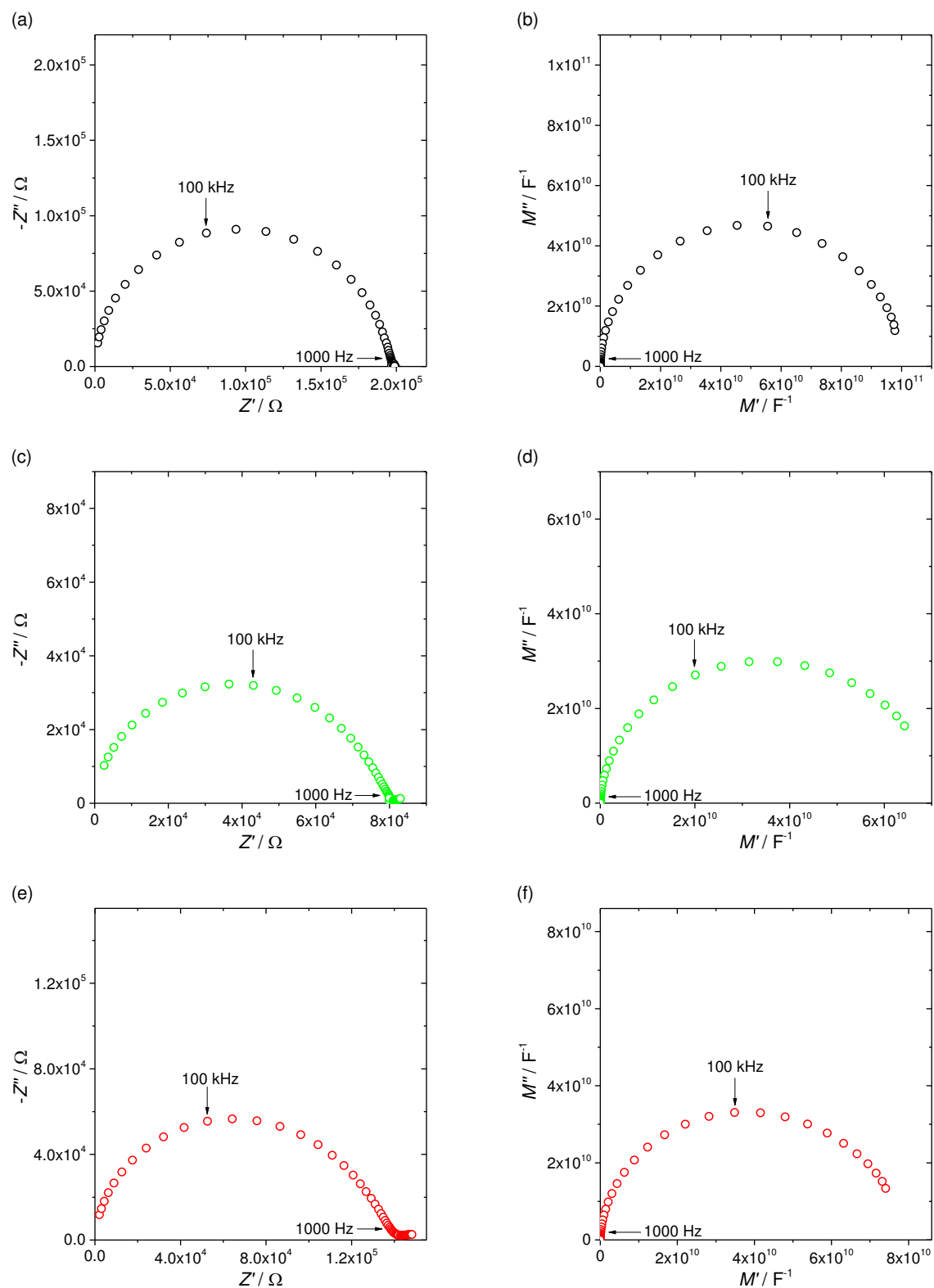


Figure 12 Impedance and modulus spectra collected at 550°C in pure oxygen: (a) and (b) undoped SrTiO₃, (c) and (d) 3at% Rb decorated SrTiO₃, (e) and (f) 5.5at% Rb decorated SrTiO₃.

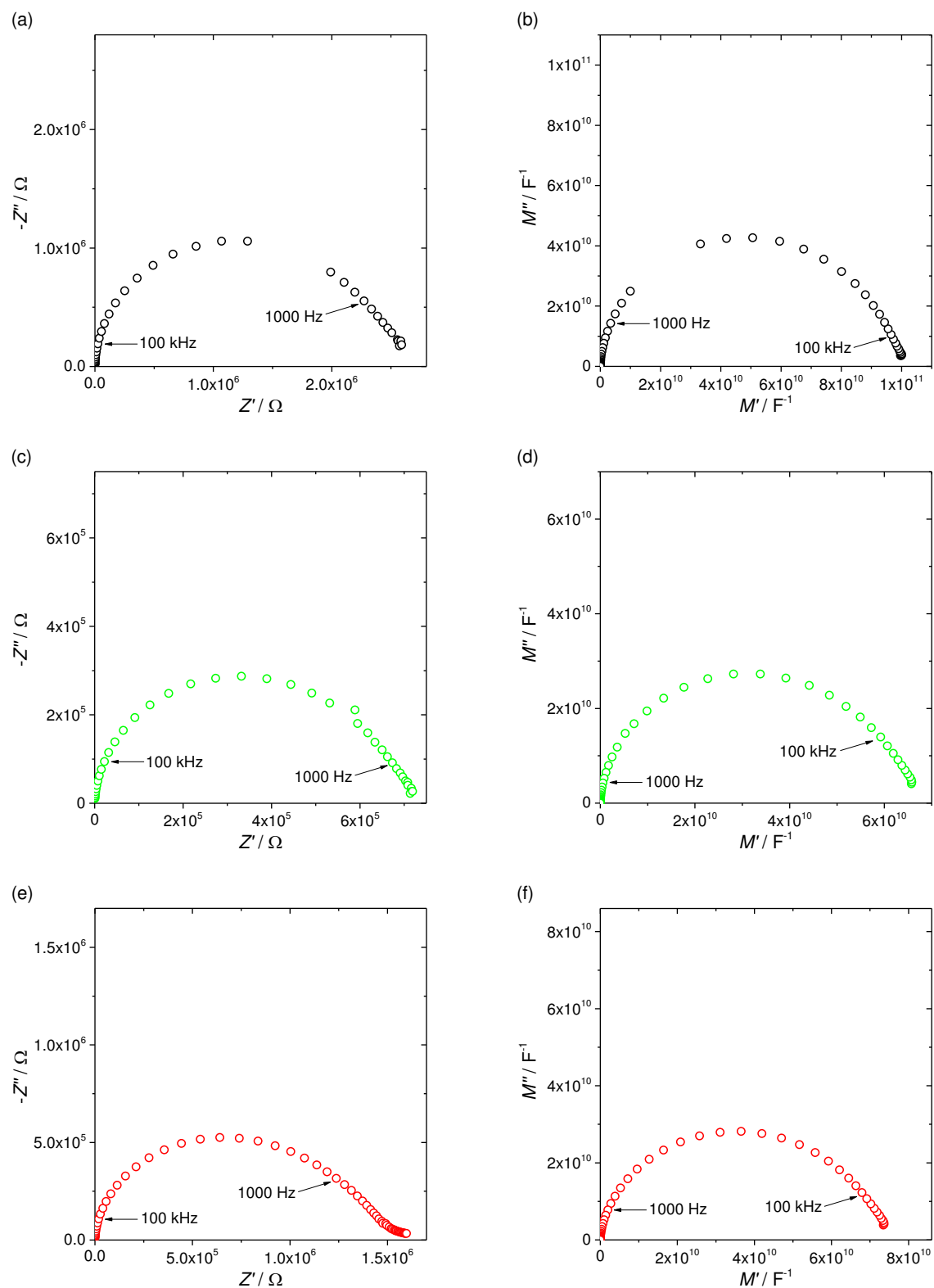


Figure 13 Impedance and modulus spectra collected at 550°C in nominally pure nitrogen ($pO_2 = 3 \cdot 10^{-5}$): (a) and (b) undoped SrTiO₃, (c) and (d) 3at% Rb decorated SrTiO₃, (e) and (f) 5.5at% Rb decorated SrTiO₃.

At very low oxygen partial pressures ($pO_2 = 10^{-21}$ - 10^{-25} bar) the impedance spectra of the three nanocrystalline sample types merely consist of a portion of semicircle (cf. Figure 14). Contrary to the spectra acquired under oxidizing conditions, the low frequency range of such impedance spectra does not seem to be distorted. Therefore they can be fitted by a single RQ equivalent circuit. Such a fit yields, analogously to the fits under oxidizing conditions, values of the dielectric constant (80 - 110) and the electrical capacitance (10 - 20 pF), which are characteristic for bulk $SrTiO_3$.

Under reducing conditions, owing to the enhanced concentration of electrons within the space charge regions, n-type conductivity occurs predominantly along the grain boundaries short-circuiting the grain interior. For this reason the dielectric constant and electrical capacitance characteristic of the bulk are again expected [46].

With regard to the impedance spectrum under reducing conditions of the 5.5at% Rb decorated $SrTiO_3$ sample, one further aspect is worth being considered: Contrary to the undoped $SrTiO_3$ it seems that a second semicircle at very low frequencies follows the one which is ascribed to the parallel grain boundaries (cf. the inset in Figure 14 (e)). Attempts to fit this contribution, whose presence can only be recognized at the highest oxygen partial pressure under reducing conditions ($pO_2 = 2 \cdot 10^{-21}$ bar), yields an electrical capacitance on the order of mF, which is roughly eight orders of magnitude larger than the capacitance of the first contribution at higher frequencies. Such a high capacitance might point towards a possible bulk polarization phenomenon. For example Jannik *et al.* [47] showed that in a homogeneously Fe doped $SrTiO_3$ bicrystal under oxidizing conditions a chemical polarization occurs at very low frequencies (\sim mHz) when performing impedance spectroscopy measurements. This is due to the positively charged grain boundary core that selectively blocks oxygen vacancies. Under the assumption that in the Rb decorated $SrTiO_3$ samples Rb substitutes Sr adjacent to the grain boundary core, a similar polarization effect under reducing conditions as a result of selective blocking can be hypothesized (more details on the possible diffusion of Rb into the grains are given in chapter 4.1.5). Irrespective of the second semicircle in the Rb decorated specimen it is important to note that the grain boundary response of all the nanocrystalline $SrTiO_3$ samples is also clearly identified in the impedance spectra under reducing conditions.

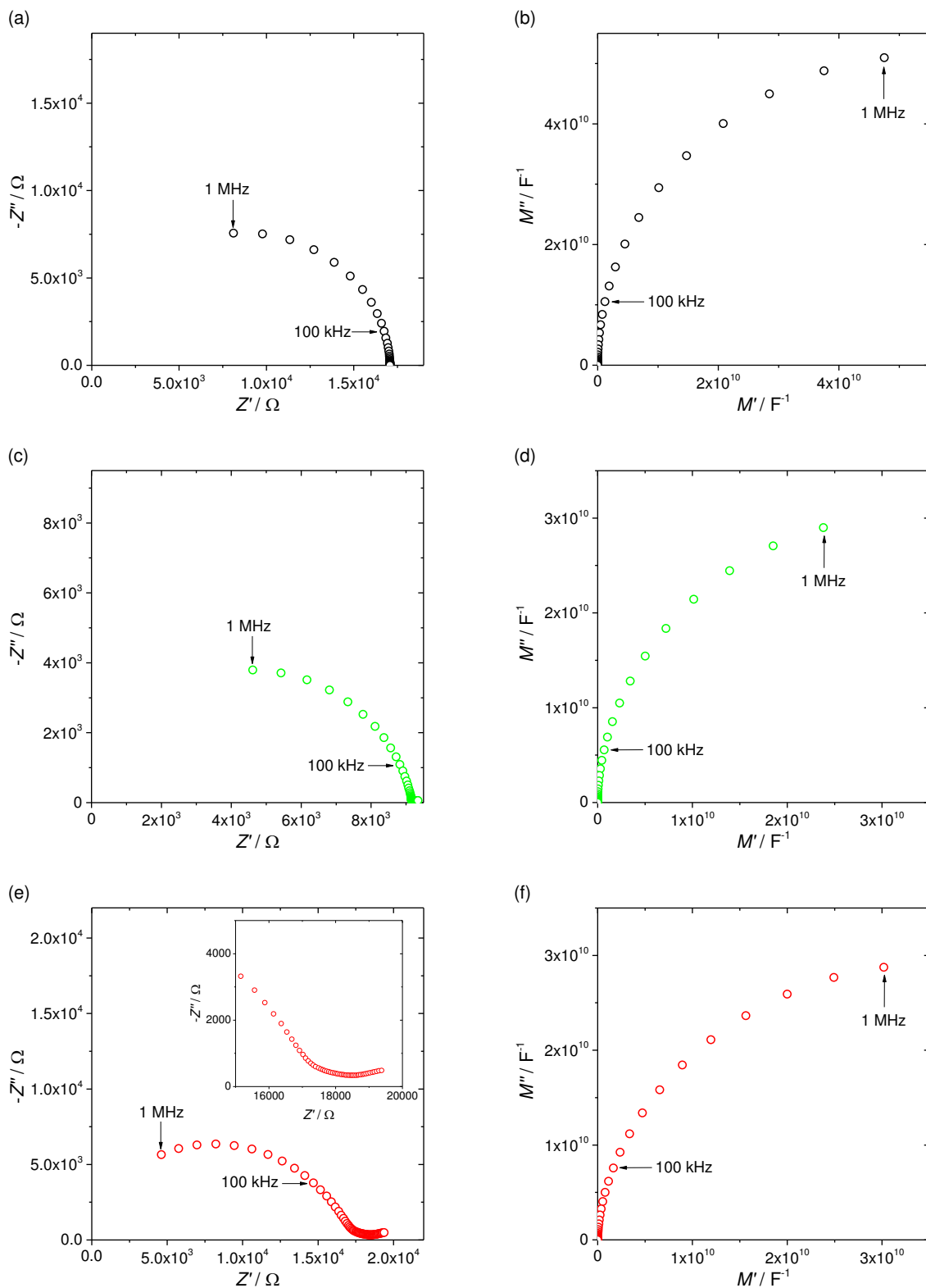


Figure 14 Impedance and modulus spectra collected at 550°C, the oxygen partial pressure at which the measurement was carried out is given separately for each sample type: (a) and (b) undoped SrTiO₃, $pO_2 = 8 \cdot 10^{-20}$ bar, (c) and (d) 3at% Rb decorated SrTiO₃, $pO_2 = 7 \cdot 10^{-21}$ bar, (e) and (f) 5.5at% Rb decorated SrTiO₃, $pO_2 = 2 \cdot 10^{-21}$ bar, the inset in (e) shows the zoomed in low frequency part of the impedance spectrum.

Conductivity data obtained from fitting the high frequency contribution of the impedance spectra acquired during temperature dependence measurements in pure oxygen between 450°C and 550°C are shown in the Arrhenius plot of Figure 15. For comparison bulk conductivity values of SrTiO₃, assuming 40 ppm Cr and 30 ppm Fe as acceptor impurities, calculated by using the mass action parameters and mobility data available from Denk *et al.* [9] are displayed as well. The temperature dependence of the Fe³⁺ concentration was considered according to the Fe ionization reaction (see equations 2.15 and 2.16). The activation energy of the p-type conductivity deduced for the nanocrystalline undoped SrTiO₃ reference sample is 1.32 eV, which agrees very well with previous studies on nanocrystalline mesoscopic SrTiO₃ [1, 2]. Furthermore, the electrical conductivity of this sample is considerably lower than that of bulk SrTiO₃ with a similar impurity content and also the activation energies of nanocrystalline SrTiO₃ ($\Delta E = 1.32$ eV) and the bulk of SrTiO₃ ($\Delta E = 0.74$ eV) clearly differ. This further corroborates the assignment of the first half of the impedance semicircle for the nanocrystalline samples (cf. Figures 12 and 13) to the space charge regions and hence demonstrates that these samples are electrically in a mesoscopic state.

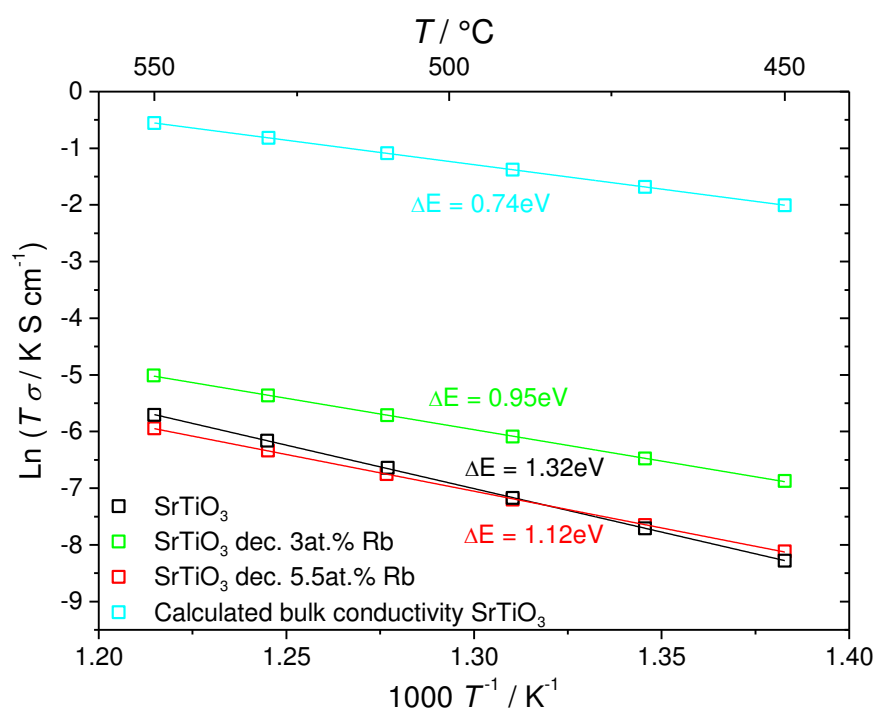


Figure 15 Arrhenius plot of the conductivities of the three nanocrystalline sample types undoped SrTiO₃, 3at% Rb decorated SrTiO₃ and 5.5at% Rb decorated SrTiO₃ in pure oxygen between 450°C and 550°C, as well as calculated bulk SrTiO₃ conductivity, assuming 40 ppm Cr and 30 ppm Fe as acceptor impurities.

Decorating roughly 25% of the surface of the undoped nanocrystalline SrTiO₃ particles by Rb ions prior to sintering (this corresponds to an overall Rb content of 3at%) leads to an

improved electrical conductivity as well as a noticeable decrease of the activation energy for the p-type conduction (cf. Figure 16 on the oxygen partial pressure dependence measurements) across the grain boundaries, compared to the undoped reference sample. Enhancing the decoration content up to 50% coverage (overall 5.5at% Rb content) does not improve such a beneficial effect. Rather, this composition displays conductivity values close to those of the undoped SrTiO_3 . Nevertheless it still shows an activation energy for the conduction lying in between the other two sample types.

Under oxidizing conditions, the oxygen partial pressure dependence of the three nanocrystalline ceramics (cf. Figure 16) provides a picture of the transport properties which is consistent with the temperature dependence plot: The 3at% Rb decorated sample displays the highest conductivity, whereas the undoped and the 5.5at% Rb decorated SrTiO_3 show nearly matching conductivities, which are lower compared to the composition with 3at% Rb. For the two decorated compositions slopes of 0.21 and 0.2 in the log-log plot are obtained whereas the undoped reference specimen exhibits a steeper oxygen partial pressure dependence with a slope of 0.23. Such values are all very close to the theoretically predicted slope of 0.25 for the p-type conduction of bulk SrTiO_3 under oxidizing conditions (cf. equation 2.10).

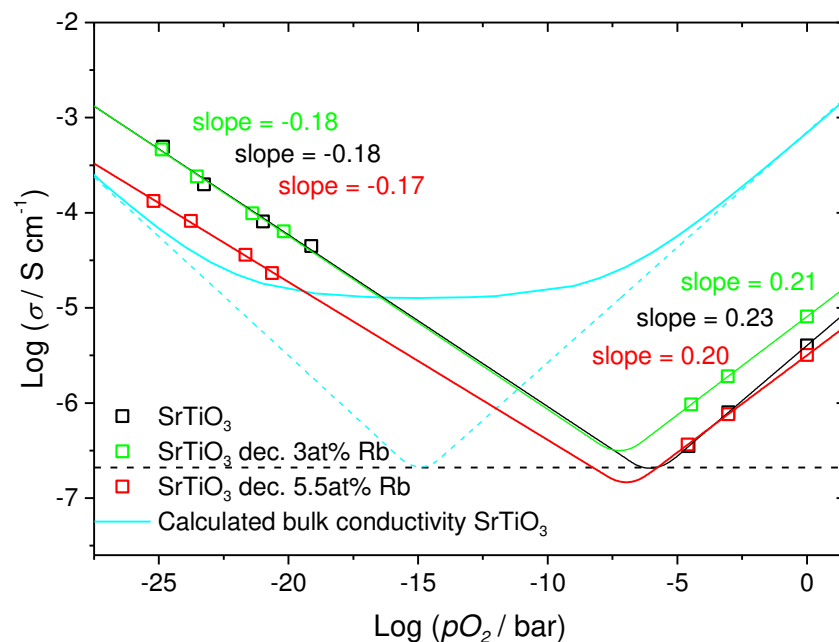


Figure 16 Oxygen partial pressure dependence at 550°C of the three nanocrystalline sample types undoped SrTiO_3 , 3at% Rb decorated SrTiO_3 and 5.5at% Rb decorated SrTiO_3 , as well as calculated bulk SrTiO_3 conductivity, assuming 40 ppm Cr and 30 ppm Fe as acceptor impurities (the continuous blue line shows the total bulk conductivity, the dashed blue line corresponds to the purely electronic bulk conductivity and the dashed black line marks the minimum of the electronic bulk conductivity).

Under reducing conditions the situation is a bit different. As a consequence of the space charge effect owing to the excess positive charge in the grain boundary core, one would expect the samples showing the lowest p-type conductivity under oxidizing conditions to display the largest n-type conductivity under reducing conditions and vice versa. Instead, the conductivities of the undoped and the 3at% Rb decorated SrTiO₃ match nearly perfectly, while the conductivity of the 5.5at% Rb decorated SrTiO₃ is lower by roughly a factor of three to four. For all three compositions the slopes in the log-log plot of the oxygen partial pressure dependence under reducing conditions, being -0.18 for the undoped SrTiO₃ and the 3at% Rb decorated SrTiO₃ and -0.17 for the 5.5at% Rb decorated SrTiO₃, are a bit higher but close to -0.25, which is the expected theoretical value for the n-type conduction of bulk SrTiO₃ under such conditions (cf. equation 2.13). Furthermore the conduction properties of the nanocrystalline undoped SrTiO₃ agree very well with previous work on mesoscopic undoped SrTiO₃ by Lupetin *et al.* [2]: Compared to the bulk conductivity of SrTiO₃ with a similar impurity content the p-type conductivity is decreased by more than two orders of magnitude, whereas the n-type conductivity is increased by slightly less than one order of magnitude. As a consequence the oxygen partial pressure at which the p-n-transition occurs is shifted by nine orders of magnitude towards higher oxygen partial pressures for the undoped nanocrystalline SrTiO₃ compared to the bulk situation.

In order to assess the degree of influence that porosity has on the electrical conductivity, further undoped SrTiO₃ samples were prepared by spark plasma sintering at 800°C and 900°C. Besides the difference in sintering temperature the rest of the program was completely identical to the one used for the samples sintered at 850°C, see chapter 3.1.1. Results from the temperature dependence measurements by impedance spectroscopy in pure oxygen between 450°C and 550°C are displayed in the Arrhenius plot of Figure 17. What immediately stands out from this plot is the fact that all three samples, despite their different sintering temperatures, show the same activation energy for the electrical conduction. This indicates that these samples being in the mesoscopic situation should also have similar grain boundary properties and thus that the differences in electrical conductivity can solely be related to the different degrees of porosity. SEM micrographs taken from cross-sections of the three samples (cf. Figure 18) confirm that their average grain size is essentially the same while the geometrical density measurements lead to values spanning between 58.2% and 70.8% for the pellets sintered at 800°C and 900°C respectively. Therefore the different p-type conductivity in pure oxygen by a factor 1.4 results from the different porosity of the nanocrystalline SrTiO₃ samples.

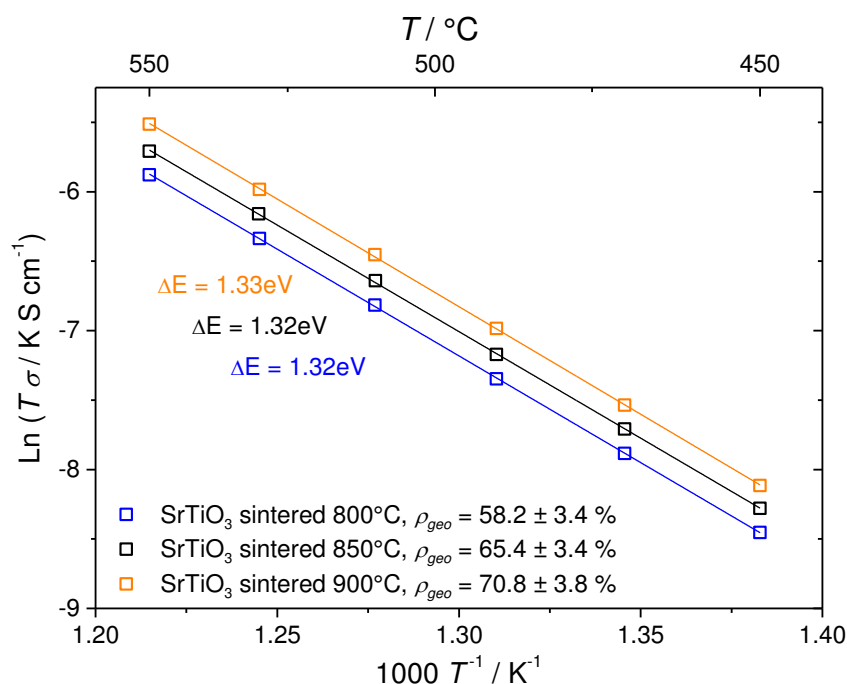


Figure 17 Arrhenius plot of the conductivities of three nanocrystalline undoped SrTiO₃ samples (sintered at 800°C, 850°C and 900°C) in pure oxygen between 450°C and 550°C.

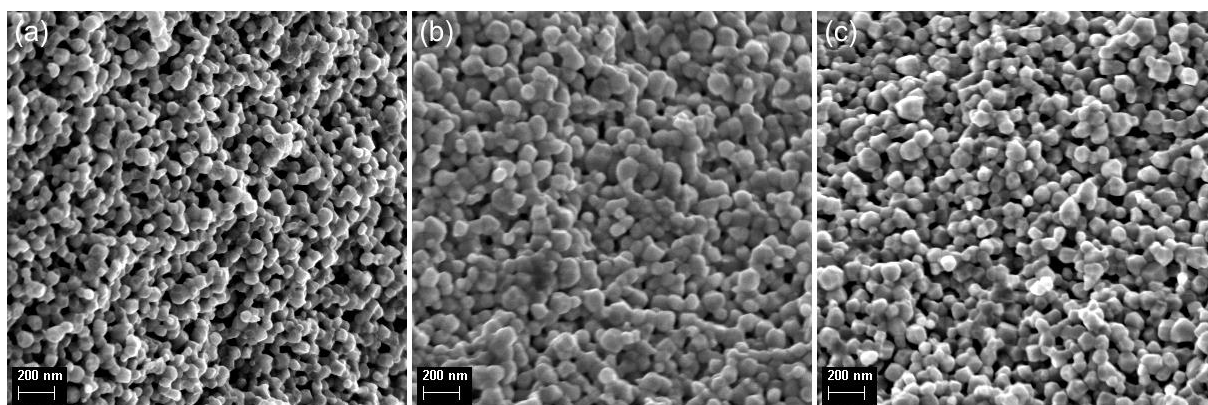


Figure 18 SEM micrographs of the nanocrystalline undoped SrTiO₃ ceramics sintered at (a) 800°C, (b) 850°C and (c) 900°C (all pictures taken from a freshly created fracture surface).

As far as the further interpretation of the data from the Rb decorated samples is regarded, a few important observations can be made at this point: 1) Due to the relatively large experimental uncertainty associated with the densities displayed in Table 4.2 those values are used here only as a rough reference point, 2) There is no simple linear relationship between the density and the electrical conductivity. This is also the reason why no normalization regarding the porosity is performed throughout this work (whenever the different densities of the three nanocrystalline sample types are significant, this is emphasized in the text). 3) For a simplified evaluation of the effect of porosity on the overall electrical transport properties, one can relate the increase of p-type conductivity (at $pO_2 = 1$ bar) by a factor of 1.4 of the undoped nanocrystalline SrTiO₃ sintered at 900°C compared to that sintered at 800°C to the

different geometrical density (12.6% difference). In comparison, from the undoped nanocrystalline SrTiO₃ reference sintered at 850°C to the 3at% Rb decorated nanocrystalline SrTiO₃ sintered at 850°C the p-type conductivity increases by a factor of 2 at 550°C in pure oxygen atmosphere, while the geometrical density of the Rb decorated sample is 11.4% higher. Therefore one could argue that the conductivity increase due to the Rb decoration would be a bit less pronounced if the conductivity data would be normalized by the densities of the samples. We note that even if – in the light of these considerations - the effect of the conductivity increase by the Rb decoration might result to be less pronounced than the data depicted in Figure 15, the effect of the addition of Rb would still be present as proven by the notable differences in activation energy.

In order to further analyze the impedance spectroscopy data acquired from the nanocrystalline mesoscopic samples, bulk conductivity data were obtained from a microcrystalline ceramic prepared starting from the same powder. Such a microcrystalline undoped SrTiO₃ sample was sintered using conventional furnace rather than spark plasma sintering. In particular, the powder was first isostatically pressed at 700 MPa for 3 minutes to form a green body, which was then sintered in air at 1400°C for 10 hours. Electrochemical impedance spectroscopy was used to determine the electrical conduction properties of the bulk by performing a temperature dependence measurement in pure oxygen from 550°C down to 450°C, as well as an oxygen partial pressure dependence measurement at 550°C covering oxygen partial pressures from 1bar down to $3 \cdot 10^{-6}$ bar. The results are displayed in Figures 19 and 20, respectively. For comparison the theoretical bulk conductivity, assuming 40 ppm Cr and 30 ppm Fe as acceptor impurities, calculated by using the mass action parameters and mobility data available from Denk *et al.* [9] is shown. The oxygen partial pressure and temperature dependence of the Fe³⁺ concentration was considered according to the Fe ionization reaction (see equations 2.15 and 2.16). The activation energy of 0.74 eV as well as the capacitance and the resulting dielectric constant values (20 pF and $\epsilon_r \approx 160$, respectively) are unequivocal indications of the bulk behavior of the microcrystalline SrTiO₃ sample, which are in accordance with previous studies [1, 2, 48, 49]. From the oxygen partial pressure dependence plot a slope of 0.22 results under oxidizing conditions. The difference to the theoretically predicted slope of 0.25 for p-type conductivity (see equation 2.10) can be ascribed to the presence of the redox-active Fe: Under oxidizing conditions the concentration of Fe³⁺ decreases with increasing oxygen partial pressure (cf. Figure 3). Both diagrams show that the slopes of the measured bulk conductivity match the calculated data rather well, however, the absolute values of the measured electrical conductivity are consistently lower than the calculated ones. This fact can be explained by

considering the effects of the sintering process: During the isothermal segment at 1400°C (10 hours) a part of the impurities can segregate at the grain boundaries due to their positive core charge. Such a high temperature segregation behavior of acceptors in SrTiO₃ has been demonstrated by Chiang *et al.* [50]. Because of the segregation, the acceptor content in the bulk and accordingly also the conductivity values are lower than the ones calculated with the acceptor content known from ICP-OES.

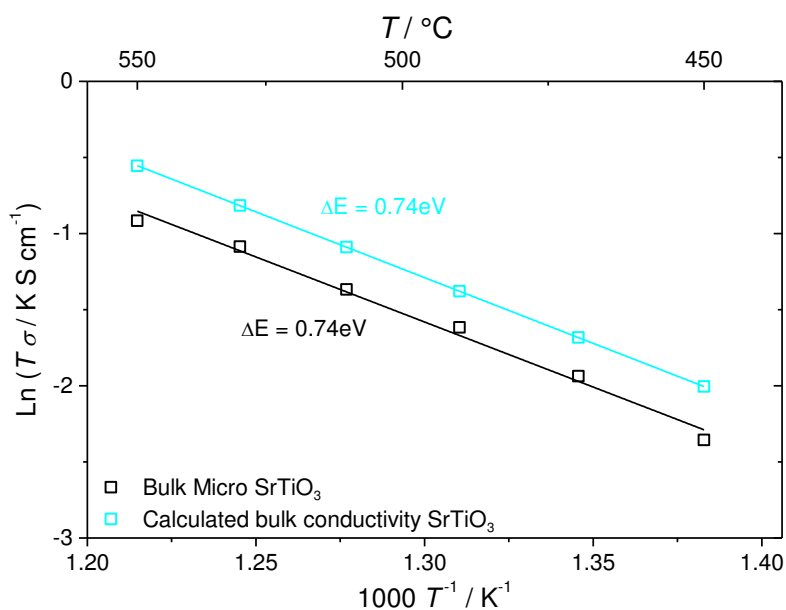


Figure 19 Arrhenius plot of the bulk conductivity of the microcrystalline SrTiO₃ sample in pure oxygen between 450°C and 550°C and calculated bulk conductivity of SrTiO₃ with 40 ppm Cr and 30 ppm Fe as acceptors based on the data available from Denk *et al.* [9].

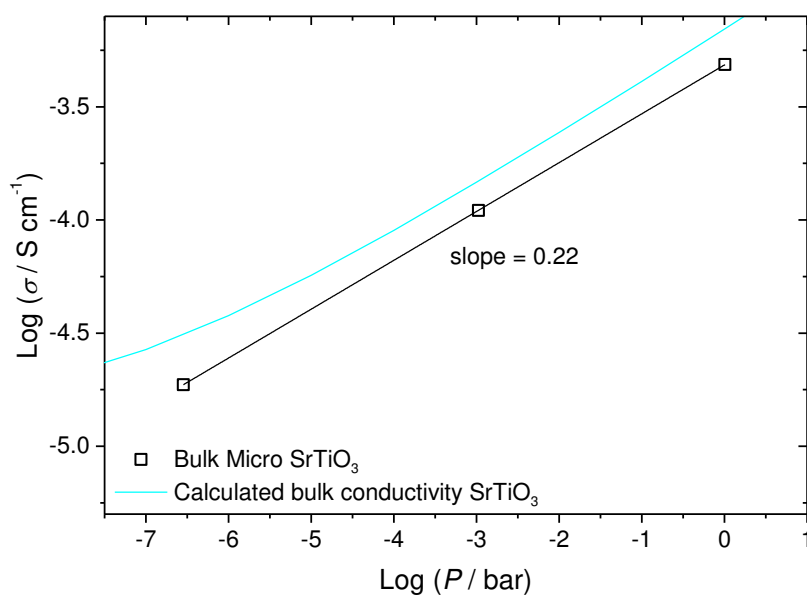


Figure 20 Oxygen partial pressure dependence of the bulk conductivity of the microcrystalline SrTiO₃ sample under oxidizing conditions at 550°C and calculated bulk conductivity of SrTiO₃ with 40 ppm Cr and 30 ppm Fe as acceptors based on the data available from Denk *et al.* [9].

4.1.5 Discussion

From the conductivity differences of the three analyzed nanocrystalline mesoscopic SrTiO₃ compositions the following questions arise:

- Does the Rb diffuse into the grain or does it stay directly at the grain boundary core?
- If it diffuses, how much Rb enters the SrTiO₃ structure and how far does it diffuse into the grain?
- How can the differences between the three sample types in their conduction properties be explained on an atomistic level?

This chapter aims to give answers to the questions above where possible and otherwise present potential approaches and assumptions to solve them.

Before one considers the Rb decorated nanocrystalline SrTiO₃ samples it is helpful to first take a look at the undoped nanocrystalline SrTiO₃ which serves here as a reference. The activation energy of the p-type conductivity in the undoped nanocrystalline SrTiO₃ extracted from the Arrhenius plot (see Figure 15) is 1.32 eV (in pure oxygen), which agrees very well with previous studies on nanocrystalline mesoscopic SrTiO₃ [1, 2]. The space charge potential of this sample at $T = 550^\circ\text{C}$ and $pO_2 = 1$ bar can be calculated according to equation 2.61. However, instead of the measured p-type bulk conductivity of the microcrystalline sample the calculated value based on the data from Denk *et al.* [9] assuming 40 ppm Cr and 30 ppm Fe as acceptor impurities is used (cf. Figure 19). This should yield a more accurate result, since the measured bulk conductivity of the microcrystalline SrTiO₃ sample is that of a sample with an impurity content in the bulk which is lower than that determined by ICP-OES on the powder, due to the high temperature acceptor segregation during sintering (as it was demonstrated in the previous chapter, cf. also Figures 19 and 20). The space charge potential calculated in this manner $\Delta\phi_0 = 0.37$ V is perfectly reasonable for such an undoped nanocrystalline SrTiO₃ ceramic with a grain size of 60 nm [1, 2]. The Mott-Schottky space charge layer width of the undoped nanocrystalline SrTiO₃ at $T = 550^\circ\text{C}$ and $pO_2 = 1$ bar is calculated according to equation 2.28, the bulk acceptor concentration is available from the theoretical calculations. This yields a space charge layer width $\lambda^* = 75$ nm, which is on the order of values from previous studies on nanocrystalline mesoscopic SrTiO₃ [1, 2]. Considering the average grain size of 60 nm, this space charge layer width clearly confirms that the undoped nanocrystalline SrTiO₃ is within the mesoscopic regime since the average grain size of the sample is much lower than the overall space charge regions. Knowing the space charge potential one can now calculate the grain boundary core charge density under the Mott-Schottky approximation

according to equation 2.30, which yields for the undoped nanocrystalline SrTiO_3 $Q_{\text{core}} = 1.91 \cdot 10^{-6} \text{ C/cm}^2$.

For a detailed analysis of the electrical conduction properties of the Rb decorated SrTiO_3 samples it is first of all necessary to determine whether the Rb diffuses into the grain during the sintering process or if it stays at the grain boundary core. For this purpose TEM EDX measurements across the grain boundaries were performed. The results presented here are obtained from a grain boundary in the 5.5at% Rb decorated SrTiO_3 sample (see Figure 21). It is worth noting that Rb was unequivocally detected at six grain boundaries (out of the nine measured in total) and that the results shown here are representative also of the other boundaries where Rb was detected. The EDX profile of Figure 21 (b) shows that Rb is only detected within a total range of about 1 nm across the grain boundary, which means that Rb diffuses roughly 5 \AA into the grain (this distance of diffusion was determined as an average from several grain boundaries). Note that this is only slightly larger than the lattice parameter of SrTiO_3 ($a = 3.905 \text{ \AA}$ [12]). Considering the fact that the grain boundary may not lie perfectly perpendicular to the distance of the EDX scan (marked by the red arrow in Figure 21 (a)), the diffusion length of the Rb might even be a bit overestimated.

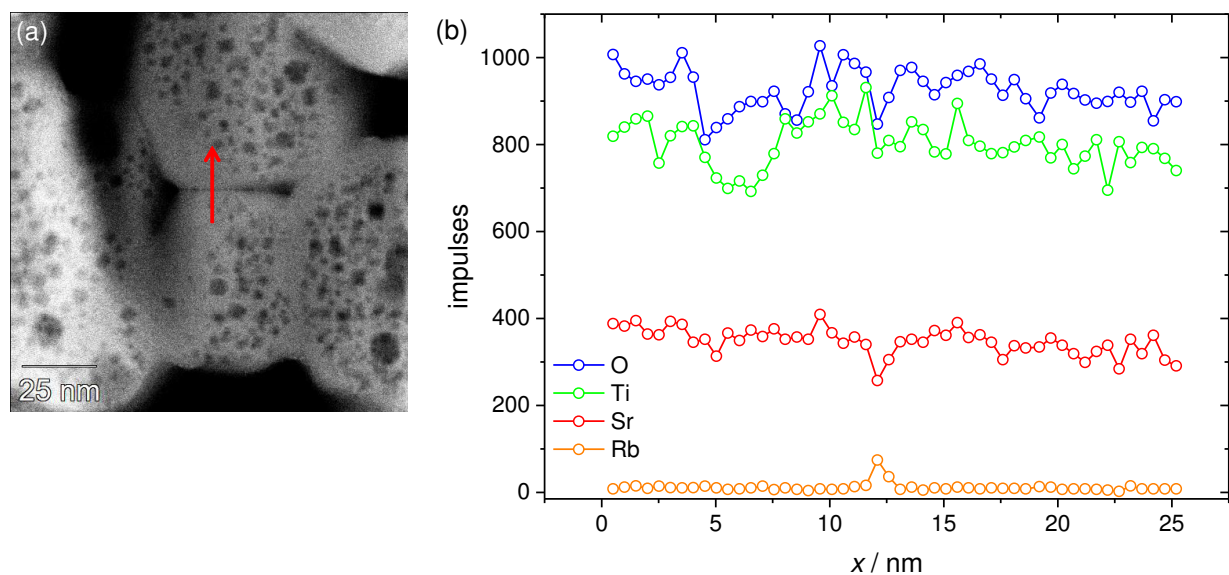


Figure 21 (a) TEM micrograph of a grain boundary in the 5.5at% Rb decorated SrTiO_3 , with the length and direction of the EDX line scan marked by a red arrow, (b) EDX counts of the elements O, Ti, Sr and Rb along the line marked in (a) with the coordinate x set to zero at the bottom of the arrow (note that only the open circles mark actual measured values, the lines in between serve as a guide to the eye).

Overall it has to be noted that Rb was not detected at all grain boundaries which were measured, pointing towards a slightly inhomogeneous distribution of the Rb. Furthermore Rb was not detected by similar line scans across grain boundaries in the nanocrystalline 3at% Rb

decorated SrTiO₃, which can be ascribed to the lower Rb content, probably being below the detection limit of the EDX setup: As it can be seen from Figure 21 (b) the peak of the Rb signal at the grain boundary is already rather low for the 5.5at% Rb decorated sample. However, also for the 3at% Rb decorated sample the local confinement of the Rb can be estimated on the basis of the results of the EDX measurement on one grain boundary: While the EDX scan of a rectangle of 4 x 1 nm² placed on the grain boundary yielded a small Rb signal, the same scan gave no Rb signal when the rectangle was shifted 2 to 3 nm below and above the grain boundary (the shifted rectangle was actually even increased in size in order to record a possibly extremely small signal). In summary, it is concluded for both Rb decorated SrTiO₃ sample types that Rb diffuses roughly 5 Å into the grains. It has to be kept in mind at this point that this diffusion length was determined based on a 5.5at% Rb decorated sample. For this sample type one can assume a larger driving force for Rb diffusion into the grain compared to the samples decorated with 3at% Rb, simply because of the higher Rb content. Consequently the shell in which Rb is located might even be a bit smaller in the case of decoration with 3at% Rb.

In conjunction with the TEM EDX characterization of the decorated SrTiO₃ specimens, two explanations for the improved p-type conductivity of the 3at% Rb decorated nanocrystalline SrTiO₃ compared to the undoped nanocrystalline SrTiO₃ (cf. Figure 16) seem possible, which result in different conduction pathways.

(a) The increased p-type conductivity could be explained by a reduced space charge potential. The Rb substitutes part of the Sr in the grain boundary core (and partially in narrow regions adjacent to the grain boundaries), leading to the formation of negative charges, which results in a reduction of the excess positive grain boundary core charge. In this case the hole conduction under oxidizing conditions is still blocked by the grain boundaries but to a minor extent compared to the undoped SrTiO₃ situation. Correspondingly the electric transport occurs through the grains in the same manner as it is known from undoped SrTiO₃ but with larger conductivity values owing to the less blocking character of the grain boundaries.

(b) If one takes into account the slight diffusion of Rb into the grain, one could picture a highly Rb doped shell directly adjacent to the grain boundary core. Due to the high acceptor doping in the shell, the hole concentration would be increased compared to the undoped grain interior and conduction under oxidizing conditions would only occur through the shell, short-circuiting the grain interior. In this case the improved conductivity of the 3at% Rb

decorated SrTiO₃ compared to the undoped SrTiO₃ would be explained by the acceptor doping.

However, the latter explanation can be ruled out for several reasons as it is discussed in the following: (b1) If such a highly doped shell would be responsible for the increased p-type conductivity of the Rb decorated SrTiO₃ it is reasonable to expect that the Rb content in the shell of the 5.5at% Rb decorated SrTiO₃ could reach or even surpass that of the 3at% Rb decorated sample because of the larger Rb amount. This should result in a further substantial increase of the p-type conductivity. However, the experimental results show the p-type conductivity of the 5.5at% Rb decorated SrTiO₃ to be roughly at the same level of the undoped nanocrystalline SrTiO₃ (cf. Figure 16). (b2) Furthermore, the EDX measurements proved a slightly inhomogeneous distribution of Rb along the grain boundaries, which causes interruptions in the shell. Consequently if the current would pass directly along the grain boundaries under oxidizing conditions doped regions with a hole concentration higher than in the grain interior would alternate with blocking regions where the hole concentration is low and reduced relative to the grain interior because of the positive grain boundary core charge, making this pathway rather unfavorable. (b3) Another important aspect worth considering is that the width of the grain boundary core in SrTiO₃ is about one to two unit cells [51] [52]. Therefore, according to the EDX data, Rb would roughly diffuse into the first unit cell outside the grain boundary core. However, it seems unlikely that a monolayer directly adjacent to the still positively charged core would serve as the main pathway for the p-type current. For all those reasons the model of a highly doped shell adjacent to the grain boundary core that serves as the only pathway for the current under oxidizing conditions in the Rb decorated nanocrystalline SrTiO₃ can be discarded.

In summary it can be concluded that Rb is mostly present in the grain boundary core, but it also diffuses into an extremely thin shell directly adjacent to the core. Rb occupying Sr positions in this shell would also explain the second arc at very low frequencies seen in the impedance spectra of the Rb decorated samples under reducing conditions (cf. Figure 14) which was ascribed to a possible polarization effect [47]. The thin layer of negatively charged defects right in front of the grain boundary would block the electrons when the current passes across the grain boundary, which can be seen at very low frequencies in the impedance spectroscopy measurement.

Let us now get back to the conduction properties of all three compositions over the full oxygen partial pressure range from 1 bar down to 10^{-25} bar. Their conductivity behavior can mostly be explained on the basis of a space charge effect. For direct comparison the slopes deduced from the oxygen partial pressure dependence plots of the conductivity are summarized in Table 4.3. We start by considering the high oxygen partial pressure range in Figure 16 from 1 bar down to 10^{-5} bar: Under pure oxygen at $T = 550^\circ\text{C}$ the space charge potential of the undoped SrTiO_3 was determined to be $\Delta\phi_0 = 0.37$ V. One can assume, based on the EDX line scans that in the decorated samples Rb basically only affects the defect chemistry in the grain boundary core and maybe one monolayer adjacent to it. As the current pathway under oxidizing conditions is then the same for the undoped and the decorated specimens the space charge potentials of the latter are calculated according to equation 2.61 (as it was already done for the undoped nanocrystalline SrTiO_3), employing the theoretically calculated bulk conductivity of SrTiO_3 with the same impurity content as it was determined by ICP-OES on the nanocrystalline powder. This yields for the 3at% Rb decorated SrTiO_3 $\Delta\phi_0 = 0.32$ V and for the 5.5at% Rb decorated SrTiO_3 $\Delta\phi_0 = 0.38$ V. These values lead to the conclusion that an initially beneficial effect of the Rb decoration reaches a maximum for a certain Rb concentration. After crossing this optimal decoration content an opposing effect sets in, which leads to a return to the conductivity values and the space charge potential of the undoped nanocrystalline SrTiO_3 .

Table 4.3 Slopes of the oxygen partial pressure dependence of the conductivity of the nanocrystalline undoped SrTiO_3 , 3at% Rb decorated SrTiO_3 and 5.5at% Rb decorated SrTiO_3 .

	$\frac{\partial \text{Log } \sigma_{meso}^{\perp}}{\partial \text{Log } pO_2}$	$\frac{\partial \text{Log } \sigma_{meso}^{\parallel}}{\partial \text{Log } pO_2}$
Undoped SrTiO_3	0.232 ± 0.00007	-0.180 ± 0.016
3at% Rb decorated SrTiO_3	0.207 ± 0.001	-0.182 ± 0.007
5.5at% Rb decorated SrTiO_3	0.204 ± 0.00004	-0.166 ± 0.005

For a characterization of the charge situation at the grain boundary core, however, the grain boundary core charge density is the more useful because more descriptive parameter. Therefore Q_{core} under the Mott-Schottky approximation according to equation 2.30 is calculated for all three sample types in the oxygen partial pressure range from 1 bar down to 10^{-5} bar (see Figure 22).

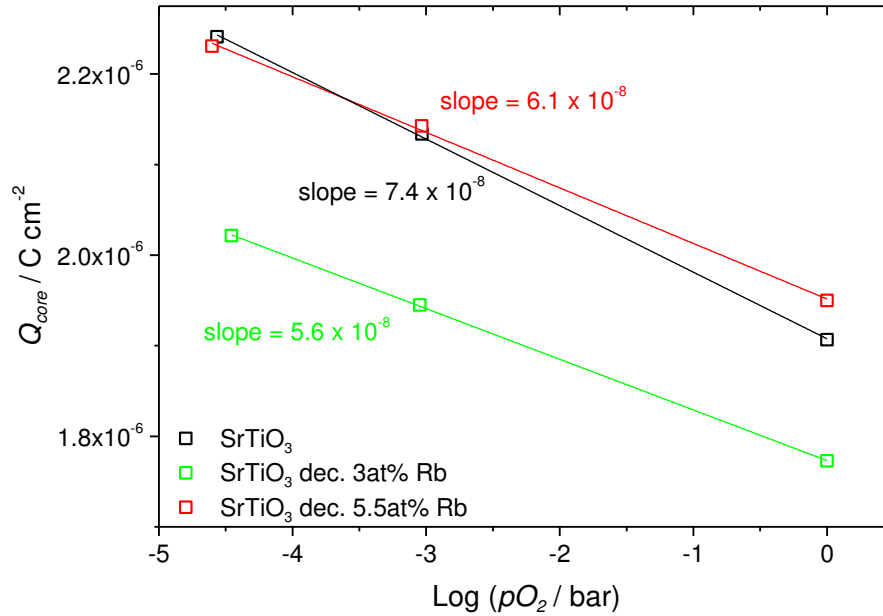


Figure 22 Oxygen partial pressure dependence of the grain boundary core charge density under oxidizing conditions at $T = 550^\circ\text{C}$ of the three nanocrystalline sample types undoped SrTiO₃, 3at% Rb decorated SrTiO₃ and 5.5at% Rb decorated SrTiO₃.

A possible explanation on an atomistic level for the differences in the core charge densities under pure oxygen between the three sample types is presented by the following. Starting from a nominally undoped grain boundary and then adding gradually more and more Rb in the grain boundary core, one can expect Rb to substitute Sr in the beginning. This should be energetically favorable since by creating negative charges the positive core charge, which is due to oxygen vacancies present in the core because of microstructural reasons, is reduced. However, in close proximity to an already substituted Sr position the substitution of another Sr should be less likely because of coulombic repulsion. Therefore one can expect that with increasing Rb content, it becomes more likely that Rb also occupies interstitial sites (i.e. is added to the material without substitution), which leads to positive charges. This should also be facilitated by those Rb ions, which are already incorporated in the Sr positions, since due to the roughly 20% larger ionic radius of Rb compared to Sr [53] it can be expected that the lattice structure is locally slightly widened. As long as there is a net negative charge resulting from the incorporation of Rb, meaning for $[Rb'_{Sr}] > [Rb_i^*]$, the core charge and hence the space charge potential should be reduced. Note that despite the incorporation of Rb, the grain boundary core charge is still expected to be positive, because otherwise the perpendicular grain boundaries would not be hindering the p-type current under oxidizing conditions anymore, which is however not observed in the experiments. Such a situation of a net negative charge should occur in the sample decorated with 3at% Rb. Furthermore, at a certain

Rb concentration within this regime a maximal net negative charge due to incorporated Rb should be achieved, which would mark the optimal decoration content with the most reduced space charge potential compared to undoped SrTiO₃.

At this point it is instructive to perform some calculations based on the grain boundary core charge at $T = 550^\circ\text{C}$ under pure oxygen of undoped ($Q_{core} = 1.91 \cdot 10^{-6} \text{ C/cm}^2$) and 3at% Rb decorated SrTiO₃ ($Q_{core} = 1.77 \cdot 10^{-6} \text{ C/cm}^2$). Under the assumption that Rb would only substitute Sr upon entering the SrTiO₃ lattice, the grain boundary core charge difference of those two sample types would mean that only 0.15% of the initially present Rb ions entered the SrTiO₃ lattice. This seems relative unlikely, as then basically all of the Rb would be present outside the SrTiO₃ lattice structure, probably as a secondary phase at the grain boundary, whereas XRD measurements on the Rb decorated specimen gave no signal from a Rb containing phase. However, if more Rb diffuses into the SrTiO₃ grain boundary core lattice it has to be present on interstitial sites as well, since otherwise the grain boundary core charge in 3at% Rb decorated SrTiO₃ should be lower. These considerations further support the model of Rb being present as a substitutional defect on Sr sites as well as an interstitial defect.

By progressively increasing the Rb content, one expects at some point to reach a situation at which the amount of Rb substituting Sr is compensated by the amount of interstitial Rb, which should de facto resemble the undoped SrTiO₃ situation. When the Rb content is increased beyond this point more Rb is placed on interstitial sites than on Sr positions, which would lead to a net positive charge due to incorporated Rb, resulting in an increased space charge potential as compared to the undoped SrTiO₃. According to the values of the grain boundary core charge (cf. Figure 22) such a situation is encountered for the 5.5at% Rb decorated SrTiO₃ under pure oxygen at 550°C.

From Figure 22 it can be seen that a decrease in the oxygen partial pressure leads to an increase of the grain boundary core charge in all three sample types. As the atmosphere becomes more reducing oxygen ions are extracted from the sample (cf. equation 2.11), which increases the oxygen vacancy concentration also in the grain boundary core and thus the grain boundary core charge. Considering the slopes extracted from the graph in Figure 22 though, one notices that the core charge increases with a slightly higher rate in the undoped SrTiO₃ compared to the decorated specimens. This fact might be explainable as follows: For a certain reduction of the oxygen partial pressure it is reasonable to assume that the total amount of additional oxygen vacancies created in the grain boundary core should be the same in all three

nanocrystalline sample types. However, in the Rb decorated samples the addition of a certain amount of oxygen vacancies to the core might allow a Rb ion which was so far present in an interstitial position to now substitute Sr. In this way the expected increase of the grain boundary core charge upon a reduction of the oxygen partial pressure could be slightly lessened because of the presence of Rb on interstitial sites.

Taking into account the oxygen partial pressure dependence of the grain boundary core charge, the slopes from the oxygen partial pressure dependence under oxidizing conditions of the conductivities of the three sample types (cf. Table 4.3) can be explained as follows: The slope of the undoped nanocrystalline SrTiO₃ is slightly lower (0.23) than the theoretically predicted value of 0.25 because of the presence of redox-active Fe, which was determined by the ICP-OES measurement. In the decorated samples one can expect the same effect of the Fe impurities. In addition, the less steep increase of the core charge upon a reduction of the oxygen partial pressure compared to the undoped SrTiO₃ leads to an even smaller slope (roughly 0.2) in the oxygen partial pressure dependence plot of the conductivity of the decorated samples.

Based on the analysis of the space charge potentials of the three nanocrystalline SrTiO₃ sample types under oxidizing conditions, it is possible to predict the expected relative positioning of their n-type conductivity branches under reducing conditions. One should keep in mind that under reducing conditions the electrical conductivity is n-type and therefore occurs along the parallel grain boundaries where the electron concentration is enhanced compared to the grain interior because of the positive space charge potential. The mesoscopic undoped and 5.5at% Rb decorated SrTiO₃ display similar electrical conductivities under oxidizing conditions and therefore similar space charge potentials. As a consequence one expects that under reducing conditions the electrical conductivities of those two samples should also be on the same level. However, the n-type branch of the conductivity of the 3at% Rb decorated SrTiO₃ though should lie below those of the other two compositions. Due to the lower space charge potential in comparison to the other two sample types the concentration of electrons adjacent to the grain boundaries should be lower and thus also the conductivity along the grain boundaries. However, the experimental data (cf. Figure 16) display basically the opposite result: While the electrical conductivities of undoped and 3at% Rb decorated SrTiO₃ match very well under reducing conditions, the electrical conductivity of 5.5at% Rb decorated SrTiO₃ is roughly a factor 3 to 4 lower.

This at first surprising result can be understood by taking a look at the electrical conductivity at the conductivity minimum. As it is pointed out by equation 2.55 differences in the minimum conductivity are only related to the mass action constant K_B of the band-band transfer and thus the band gap, assuming that the mobilities of electrons and holes remain unchanged in the different samples. At the same time one has to consider the fact that according to equation 2.63 a change of K_B would also alter the value of the oxygen partial pressure at the minimum. As a result a change of the band gap basically only affects the position of the n-type conductivity branch, whereas the position of the p-type branch stays the same. Since the minimum conductivities of all three sample types slightly differ, possible corresponding differences in the band gaps of the materials might explain the at first unexpected relative positions of the n-type conductivity branches under reducing conditions.

In order to prove this hypothesis diffuse reflectance spectroscopy was employed to determine the band gaps of the nanocrystalline ceramics. It is important to note that all of the following discussion on the band gap of SrTiO_3 considers the indirect band gap. The band gaps determined both from the diffuse reflectance spectra and from the conductivity minimum in the oxygen partial pressure dependence plot of the conductivity (see Figure 16) are summarized in Table 4.4, whereas characteristic diffuse reflectance spectra of the three nanocrystalline sample types are shown in Figure 23. Concerning the validity of the band gap values determined via these two methods one can compare the values determined in this work for undoped nanocrystalline SrTiO_3 to literature data: The band gap at 0 K derived from the conductivity minimum is best compared to the work by Denk *et al.* [9], from which the defect thermodynamical data was used for calculations throughout this thesis. In this reference, the band gap at 0 K is determined to be 3.3 eV which matches perfectly with the band gap of the undoped nanocrystalline SrTiO_3 of 3.294 eV. Employing the temperature dependence of the SrTiO_3 band gap from [9] one ends up with 3.12 eV at room temperature, whereas Kok *et al.* [54] determine it to be 3.20 eV. So also the band gap determined by diffuse reflectance spectroscopy at room temperature of 3.16 eV agrees very well with the available literature data.

Table 4.4 Band gaps of the three nanocrystalline sample types undoped SrTiO₃, 3at% Rb decorated SrTiO₃ and 5.5at% Rb decorated SrTiO₃ determined from the conductivity minimum in the oxygen partial pressure dependence plot of the conductivity (see Figure 16) and by diffuse reflectance spectroscopy.

	E_B [eV] at 0 K (determined from σ_{min})	E_B [eV] at 293 K (determined by diffuse reflectance spectroscopy)
Undoped SrTiO ₃	3.294	3.164 ± 0.017
3at% Rb decorated SrTiO ₃	3.231	3.127 ± 0.019
5.5at% Rb decorated SrTiO ₃	3.338	3.159 ± 0.015

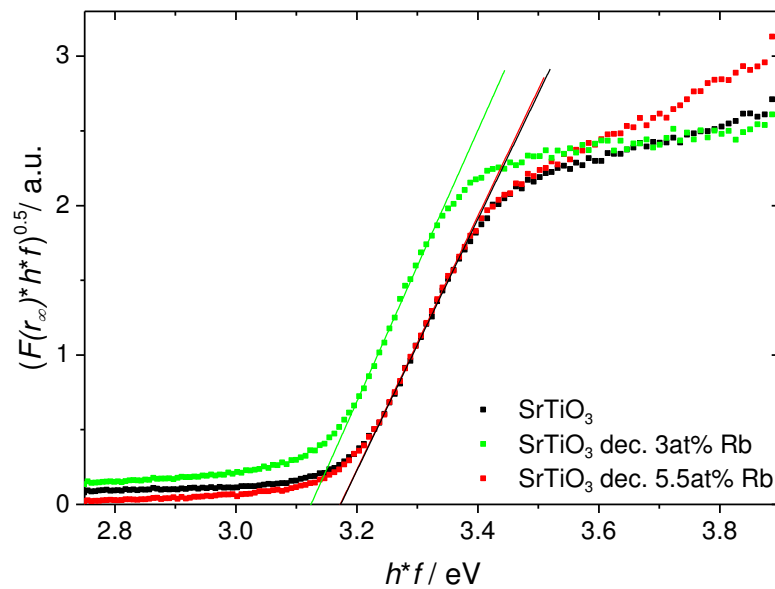


Figure 23 Tauc plot derived from diffuse reflectance spectra of the three nanocrystalline sample types undoped SrTiO₃, 3at% Rb decorated SrTiO₃ and 5.5at% Rb decorated SrTiO₃ (the extrapolation of the steep linear rise in absorption onto the x-axis for the determination of the band gap is exemplarily displayed).

The slight band gap decrease for the 3at% Rb decorated SrTiO₃ compared to undoped SrTiO₃ of $\Delta E_B \approx 0.06$ eV, which was determined from the electrochemical characterization is confirmed by the diffuse reflectance spectroscopy measurements yielding $\Delta E_B \approx 0.04$ eV. Interestingly, a band gap reduction in SrTiO₃ due to Fe doping was already observed by Da Silva *et al.* [55] and Rothschild *et al.* [56]. The measurement error for the band gap determined from the diffuse reflectance spectra seems relatively large in light of the band gap differences that are discussed here. Therefore it is important to note that for each nanocrystalline SrTiO₃ sample type, diffuse reflectance spectra were acquired from several samples on different days. While the determined band gaps obviously vary a bit, two main trends emerge from the separate comparison of the spectra from the samples that were

measured together: (i) The band gap of the 3at% Rb decorated SrTiO₃ is always slightly lower than that of the other two compositions and (ii) the band gaps determined for undoped SrTiO₃ and 5.5at% Rb decorated SrTiO₃ are always very close to each other. From the oxygen partial pressure dependence measurement of the conductivity one expects the band gap of 5.5at% Rb decorated SrTiO₃ to be a bit larger than that of undoped SrTiO₃. However, analysis of the diffuse reflectance spectra shows that those two sample types display very similar band gap values which might be explainable by the following considerations: Because of the local confinement of the Rb it is reasonable to expect that the band gap change also only occurs in a spatially very limited region directly adjacent to the grain boundary core. This would mean that in the Rb decorated samples the band gap within the grains should be equal to that of undoped SrTiO₃, while directly at the grain boundary it is altered. Assuming that in 5.5at% Rb decorated SrTiO₃ locally at the grain boundary the band gap is indeed slightly increased compared to undoped SrTiO₃ one can nevertheless not detect it by diffuse reflectance spectroscopy, since in that measurement it only matters which part of the sample starts to absorb light first. This would be the grain interior, which would explain the similar band gap compared to undoped SrTiO₃.

In summary it can be concluded that the absolute values of the band gaps determined from the conductivity minima in the oxygen partial pressure dependence plots as well as the slight differences in the band gaps between the three nanocrystalline sample types are realistic in light of the reasons listed as follows.

- (i) For the undoped nanocrystalline SrTiO₃ it was clearly demonstrated that the band gap values determined in this work agree very well with literature data.
- (ii) The band gap difference between undoped SrTiO₃ and 3at% Rb decorated SrTiO₃ deduced from the conductivity data was confirmed by the diffuse reflectance measurements.
- (iii) Under the assumption that the band gap in the Rb decorated samples is only altered directly at the grain boundary it is a logical consequence that the band gap determined for 5.5at% Rb decorated SrTiO₃ by diffuse reflectance spectroscopy is equal to undoped SrTiO₃, assuming that the local band gap at the grain boundary is increased in the 5.5at% Rb decorated sample compared to the undoped SrTiO₃.

Finally one has to consider the slopes under reducing conditions in the oxygen partial pressure dependence plot of the conductivity (Figure 16). All three nanocrystalline sample types clearly display n-type conductivity, however, $(\partial \text{Log } \sigma / \partial \text{Log } pO_2)$ is roughly -0.18 for all three samples, which significantly deviates from the theoretically predicted

$(\partial \text{Log } \sigma^I / \partial \text{Log } pO_2) = -0.25$ (cf. equation 2.13). At such low oxygen partial pressures all of the Fe impurities are reduced to Fe^{3+} and therefore an influence on the conductivity due to partial ionization like it is seen under oxidizing conditions (cf. Figure 3) can be ruled out. Since the slopes are very similar for all three compositions also an influence of Rb can be pretty safely discarded. This leaves us with possible association reactions like $V_{\text{O}}^{\bullet\bullet} + e^- \rightleftharpoons V_{\text{O}}^{\bullet}$ that get more favorable when the oxygen partial pressure is decreased. In this way more and more electrons would be bound when decreasing the oxygen partial pressure, which would result in a lower conductivity than theoretically expected. However, this is only a hypothesis, since in previous work [3] the slope of the pO_2 dependence of the n-type conductivity in mesoscopic SrTiO_3 under reducing conditions was determined to be exactly -0.25.

In summary the whole oxygen partial pressure dependence of the conductivity of the three nanocrystalline sample types undoped SrTiO_3 , 3at% Rb decorated SrTiO_3 and 5.5at% Rb decorated SrTiO_3 in the range $pO_2 = 1 - 10^{-25}$ bar can be summarized as follows (the undoped SrTiO_3 sample serves as a reference state which the Rb decorated ones are compared to).

Under oxidizing conditions the effect of the Rb decoration can be explained on the basis of a space charge effect since the Rb is spatially confined to the grain boundary. Up to a certain critical threshold of the Rb concentration, $[Rb'_{\text{Sr}}] \geq [Rb_i^{\bullet}]$ holds in the grain boundary core. As a result the grain boundary core charge and thus the space charge potential is decreased and the p-type conductivity increased (the 3at% Rb decorated SrTiO_3 falls into this regime). Increasing the Rb content beyond this threshold leads to $[Rb'_{\text{Sr}}] < [Rb_i^{\bullet}]$. Then the grain boundary core charge is increased and consequently the p-type conductivity is lower compared to undoped SrTiO_3 . The 5.5at% Rb decorated SrTiO_3 is situated at the border of those two regimes.

Based purely on a space charge driven effect, the n-type conductivity under reducing conditions of the 3at% Rb decorated SrTiO_3 should be lower than that of undoped SrTiO_3 . However, since the band gap of the 3at% Rb decorated SrTiO_3 is decreased, the corresponding n-type conductivity branch is shifted towards higher conductivities and thus overlaps with that of undoped SrTiO_3 . The asymmetric shift of p-type and n-type conductivity branches as a result of a band gap change can be seen from the different dependencies of σ_{min} and $pO_{2,\text{min}}$ on K_B (cf. equations 2.55 and 2.63). According to the value of σ_{min} of 5.5at% Rb decorated SrTiO_3 its band gap is larger than that of undoped SrTiO_3 and consequently its n-type conductivity is also lower, although the space charge potentials under oxidizing conditions in these two samples are similar.

4.2 SrTiO₃ bicrystals

This section presents the experimental results of the electrochemical characterization of the SrTiO₃ bicrystals made in our labs. To the best of our knowledge this was the first time that a fabrication of SrTiO₃ bicrystals by spark plasma sintering was attempted, starting from commercially available single crystals. The primary focus was to find suitable sintering parameters that allowed for a reproducible bonding of the single crystals, which proved to be quite challenging. Nevertheless, efforts were made towards the production of two specific grain boundary orientations, namely $\Sigma 3$ (111) and $\Sigma 13$ (510). Similar to the nanocrystalline SrTiO₃ ceramics that were discussed in the previous chapter, also for the bicrystals a grain boundary decoration with Rb was attempted. Since the reproducibility of the SrTiO₃ bicrystals fabrication was rather poor, the results in this chapter are displayed and critically discussed on the basis of selected examples, for which at least partial bonding between the two single crystals was realized.

4.2.1 Undoped SrTiO₃ bicrystals

4.2.1.1 Determination of the spark plasma sintering parameters

Based on the spark plasma sintering parameters for the nanocrystalline SrTiO₃ ceramics ($T = 850^\circ\text{C}$, applied pressure of 350MPa, Ar atmosphere and holding time of 5 minutes) the first attempts of the bicrystal fabrication were carried out at similar temperatures ranging from 800°C to 900°C with a holding time of 5 minutes, while reducing the applied pressure to 130 MPa in order to reduce the stress exerted on the single crystals. In this first trial phase the orientation of the grain boundary was not of importance and therefore in most of the cases two (100) oriented SrTiO₃ single crystals were used. Figure 24 shows the results of the electrochemical characterization of such a SrTiO₃ bicrystal by impedance spectroscopy. In this case the bicrystal was sintered at 900°C. From the impedance spectrum in Figure 24 (a) three contributions at high, medium and low frequencies are clearly distinguishable. Accordingly the spectrum was fitted with an equivalent circuit consisting of three RQ pairs in series. By performing impedance spectroscopy measurements in pure oxygen between 400°C and 500°C the activation energies of the conductivities associated with these three contributions are accessible (see Figure 24 (b)). In this temperature range a capacitance $C = 29 - 36$ pF, a relative dielectric constant $\epsilon_r = 125 - 156$ and an activation energy $\Delta E = 0.57$ eV were determined for the high frequency contribution, clearly demonstrating that it can be related to the bulk of SrTiO₃ [5, 6, 57]. For the contribution at medium frequencies the fit yields a capacitance $C \approx 4$ nF and an activation energy $\Delta E = 1.19$ eV, whereas for the

low frequency contribution $C \approx 90$ nF and $\Delta E = 1.20$ eV were determined. These capacitance values are relatively close to each other but it turns out that only the latter is comparable with a space charge effect. To show this, tentatively the Mott-Schottky space charge layer widths associated with the two contributions are calculated based on their fitted capacitances by combination of the equations 2.39 and 2.40. Note that for a bicrystal it applies that $N = 2$ in equation 2.39, whereas in equation 2.40 $N = 1$ has to be used since the current only passes one grain boundary ($N =$ “total number of grains” in equation 2.40 can only be used for a polycrystalline ceramic). It can be assumed that the relative permittivities of bulk and grain boundary are the same, while the grain size is simply half of the bicrystal thickness. This yields for the contribution at medium frequencies $\lambda^* = 4.15$ μm and for the low frequency contribution $\lambda^* = 172$ nm at $T = 400^\circ\text{C}$. Only the last value is on the order of typical space charge layer widths of SrTiO_3 , as e.g. De Souza *et al.* [5] determined $\lambda^* = 30$ nm at $T = 420^\circ\text{C}$ and $pO_2 = 0.1$ bar for a symmetrical 5.4° [001] tilt grain boundary in a Fe-doped SrTiO_3 bicrystal. The difference in the absolute values of the space charge layer width arises from the different doping contents (the bicrystals in this work are produced from nominally undoped SrTiO_3 single crystals) and the slightly different oxygen partial pressures. Note that the assignment of a certain contribution in the impedance spectrum to the grain boundary will be based for all bicrystals on the determination of the space charge layer width according to the experimental capacitances as described above, while the conductivity of such a signal is calculated according to equation 2.44.

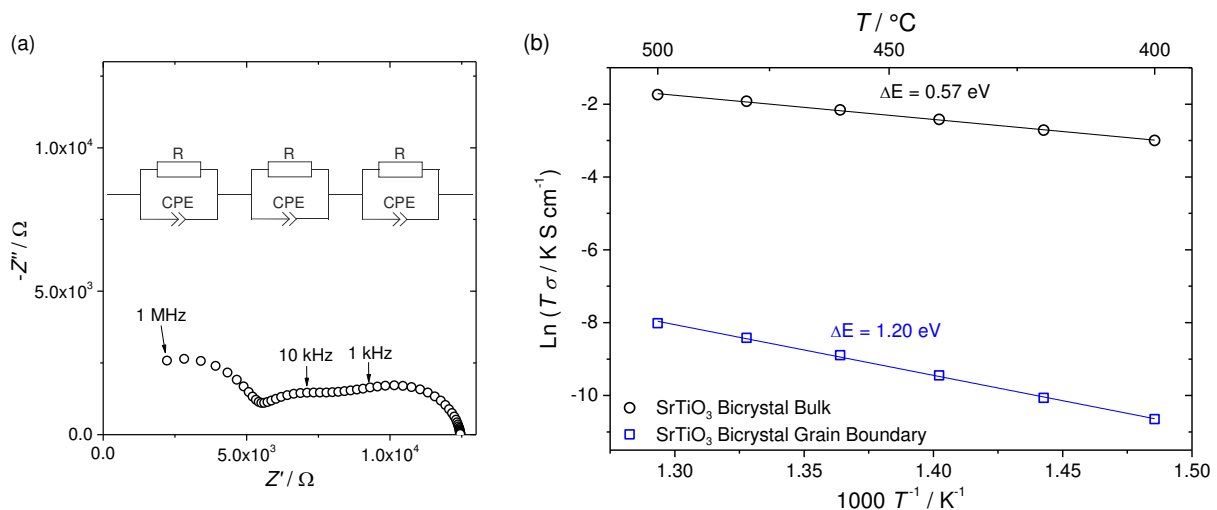


Figure 24 (a) Impedance spectrum of a SrTiO_3 bicrystal consisting of two (100) single crystals sintered at $T = 900^\circ\text{C}$ (data collected at $T = 400^\circ\text{C}$ in pure oxygen) and the equivalent circuit used for the fitting, (b) Arrhenius plot of the conductivities of bulk and grain boundary of the same SrTiO_3 bicrystal, data collected in pure oxygen between 400°C and 500°C .

For further verification that the semicircle at low frequencies is indeed associated with the grain boundary contribution, the space charge potential is calculated according to equation 2.38 which yields $\Delta\phi_0 = 0.62$ V at $T = 400^\circ\text{C}$. Again this value agrees very well with the work by De Souza *et al.* [5] where they determined $\Delta\phi_0 = 0.54$ V at $T = 400^\circ\text{C}$ for the symmetrical 5.4° [001] tilt grain boundary. Moreover, assuming an impurity content of 0.005 at% Fe as it was typically detected by ICP-OES on different SrTiO₃ single crystals used in this work (note that the temperature and oxygen partial pressure dependent concentration of Fe³⁺ needs to be considered) and employing the space charge potential $\Delta\phi_0 = 0.62$ V, equation 2.28 yields a space charge layer width $\lambda^* = 243$ nm at $T = 400^\circ\text{C}$. This value is relatively close to the space charge layer width calculated according to the capacitances of bulk and grain boundary (172 nm). Regarding the remaining contribution at medium frequencies, the similarity of the activation energy of this contribution ($\Delta E_{MF} = 1.19$ eV) to the activation energy of the grain boundary ($\Delta E_{GB} = 1.20$ eV) is striking. Considering the possibility that an imperfect grain boundary contact was created during spark plasma sintering, a current constriction effect could occur. The presence of pores at the grain boundary forces the current to deviate from the otherwise straight pathways, leading to the occurrence of an additional resistive contribution, which is visible in the impedance spectra at frequencies lower than that comprising the bulk semicircle [43-45]. As shown before, the extension of the, under oxidizing conditions strongly blocking, space charge zone in a SrTiO₃ bicrystal of such high purity is very large (roughly 200 nm). Therefore the current constriction effect is decisively influenced by the space charge zone and consequently the activation energy associated with the current constriction effect should be similar to the grain boundary activation energy. Based on these considerations the contribution at medium frequencies is associated with a current constriction effect.

As mentioned before the reproducibility of the SrTiO₃ bicrystals proved to be quite difficult meaning that, although the sintering parameters stayed nominally the same, the following problems occurred rather frequently: (i) the single crystals did not bond at all, (ii) the single crystals (partially) bonded but presented several cracks and (iii) the single crystals partially bonded while also larger air bubbles were trapped at the interface. In order to potentially overcome these problems several adjustments to the bicrystal pressing process were performed. Following the teaching of classical diffusion bonding of bicrystals the sintering temperature was raised to 1200°C and the holding time was increased to 20 minutes with the aim to improve the bonding. Furthermore, larger single crystals were used in order to reduce the pressure onto the single crystals during the sintering process. A simple reduction of the

applied force in the spark plasma sintering machine was not possible since the machine requires a certain minimum force to ensure contact of all the pressing tools. In addition the use of larger single crystals should also minimize the problem of partial bonding, because it enhances the chance of creating a larger contacted portion that can be cut out and used for the electrical measurements.

Figure 25 displays a partially bonded $\Sigma 3$ (111) SrTiO₃ bicrystal which was sintered according to the adjusted conditions described above (only the holding time was still 5 minutes in this preliminary test). Two larger air inclusions and an unconnected stripe at the right side can be clearly identified by the colored Newton interference rings. The red rectangle marks the bonded part which was cut out for impedance measurements.

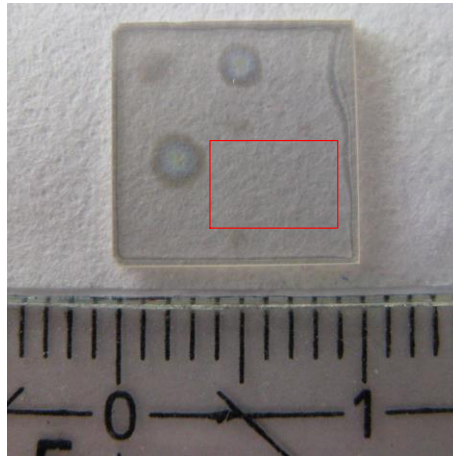


Figure 25 Photograph of a partially bonded $\Sigma 3$ (111) SrTiO₃ bicrystal, the part marked by the red rectangle was cut out for impedance measurements (the distance from zero to one on the ruler equals one centimeter).

The electrical characterization of the $\Sigma 3$ (111) SrTiO₃ bicrystal shown in Figure 25 by impedance spectroscopy (cf. Figure 26) displays very similar results to that of the bicrystal with the undefined grain boundary presented in the beginning of this chapter. The impedance spectrum consists of three very well separated semicircles of which the one at the highest frequencies is clearly associated with the bulk of SrTiO₃ based on $C = 33$ pF and $\epsilon_r = 155$ at $T = 500^\circ\text{C}$ and $\Delta E = 0.57$ eV deduced from the fit of this semicircle. Again, the remaining two contributions can be differentiated by their Mott-Schottky space charge layer widths, calculated from their fitted capacitances, which are $\lambda^* = 16.9$ μm and $\lambda^* = 301$ nm at $T = 500^\circ\text{C}$ for the medium and the low frequency semicircle, respectively. Therefore, also for this bicrystal sintered at 1200°C the impedance semicircle at low frequencies can be assigned to the grain boundary. Such assignment is reasonable also in the light of the corresponding activation energy value determined in pure oxygen atmosphere ($\Delta E = 1.28$ eV), as e.g. for a $\Sigma 5$ SrTiO₃ bicrystal grain boundary $\Delta E = 1.4$ eV was determined in a previous study [4].

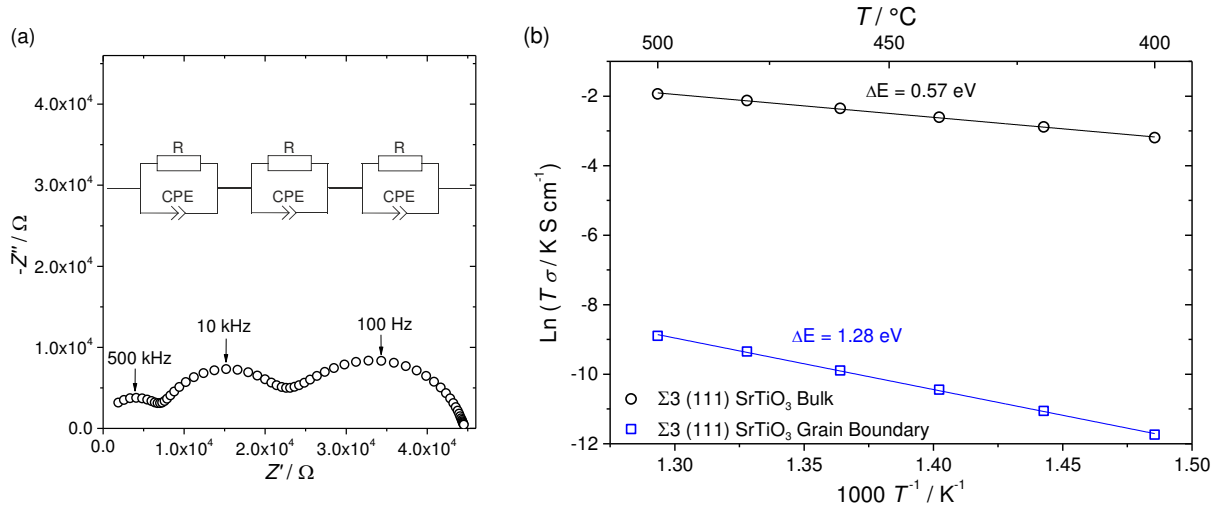


Figure 26 (a) Impedance spectrum of a $\Sigma 3$ (111) SrTiO_3 bicrystal sintered at $T = 1200^\circ\text{C}$ (data collected at $T = 400^\circ\text{C}$ in pure oxygen) and the equivalent circuit used for the fitting, (b) Arrhenius plot of the conductivities of bulk and grain boundary of the same SrTiO_3 bicrystal, data collected in pure oxygen between 400°C and 500°C .

The space charge potential of this bicrystal is calculated according to equation 2.38 and displays a slight temperature dependence (see Figure 27). Such a behavior was also observed by De Souza *et al.* [5] on the symmetrical 5.4° [001] tilt grain boundary in a Fe-doped SrTiO_3 bicrystal and can be ascribed to the different defect chemistry of bulk and grain boundary core. The absolute value of the space charge potential obtained from the data of Figures 26 and 27, $\Delta\phi_0 = 0.66 - 0.68$ V, is well within the range of space charge potentials determined for several SrTiO_3 poly- and bicrystals [58, 59]. A slight deviation from the perfect $\Sigma 3$ (111) orientation might for example explain the somewhat high value of the space charge potential, assuming that this deviation results in a grain boundary of slightly lower symmetry which would then contain a higher concentration of structurally required oxygen vacancies.

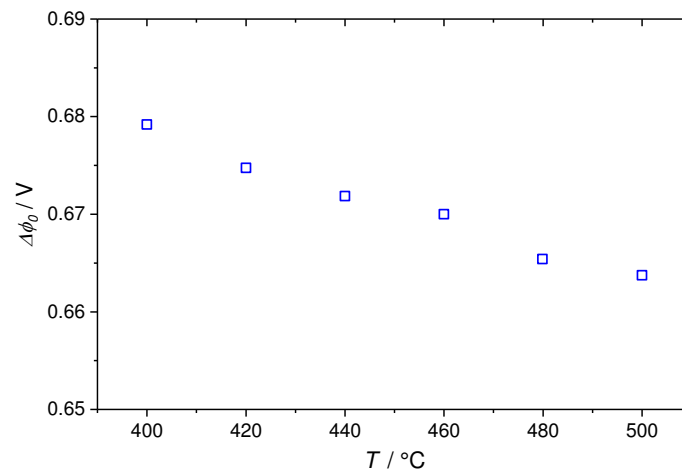


Figure 27 Temperature dependence of the space charge potential in the $\Sigma 3$ (111) SrTiO_3 bicrystal sintered at $T = 1200^\circ\text{C}$.

The thickness of the space charge layer $\lambda^* = 301$ nm at $T = 500^\circ\text{C}$ is relatively large and points towards a very low impurity content. Assuming that Fe is the only impurity, the bicrystal would contain 14 ppm Fe. This is approximately confirmed by an ICP-OES measurement of the bicrystal which yields 50 ppm Fe, 50 ppm Ca and 40 ppm Ba as the main impurities. Hereof only Fe is relevant from an electrochemical point of view, since both Ba and Ca are divalent and therefore create a neutral defect when substituting Sr. As can be seen from Figure 28 (a), both bulk and the grain boundary show an oxygen partial pressure dependence of the conductivity under oxidizing conditions with a slope of roughly 0.24. According to equation 2.47 one can deduce $(\partial \log m / \partial \log pO_2) = -0.01$ from the oxygen partial pressure dependence of the bulk conductivity, whereas the theoretical calculation of the oxygen partial pressure dependence of $[\text{Fe}^{3+}]$ for $[\text{Fe}_{\text{total}}] = 0.005$ at% yields $(\partial \log m / \partial \log pO_2) = -0.09$. A possible explanation for the difference would be a segregation of Fe to the grain boundary at the high temperatures during the sintering process. This can in principle be easily verified by taking a look at the oxygen partial pressure dependence of the grain boundary conductivity (see Figure 28 (a)) and the space charge potential (see Figure 28 (b)) and calculating $(\partial \log m / \partial \log pO_2)$ for the grain boundary based on equation 2.50. However, since the oxygen partial pressure dependence of the space charge potential is surprisingly positive, $(\partial \log m / \partial \log pO_2) = -0.005$ for the grain boundary and therefore similar to that in the bulk, which contradicts the possible Fe segregation to the grain boundary. As a consequence $[\text{Fe}_{\text{total}}]$ should indeed be lower than determined by ICP-OES. Normally one expects the space charge potential to slightly increase upon a reduction of the oxygen partial pressure under oxidizing conditions, since the oxygen vacancy concentration and therefore the grain boundary core charge should increase (this would then lead to a more negative value of $(\partial \log m / \partial \log pO_2)$ for the grain boundary, indicating Fe segregation). Since only three data points are available in this partial pressure range it is at this point not possible to give a final answer on whether the space charge potential is indeed decreasing when decreasing the oxygen partial pressure and therefore whether the impurity content is somehow lower than measured by ICP-OES. Or if instead some error might have occurred during the impedance spectroscopy measurement in nominally pure nitrogen, resulting in a too low space charge potential.

For the semicircle at medium frequencies in Figure 26 (a) an activation energy of $\Delta E_{MF} = 1.11$ eV is determined. Again this value is close to the activation energy of the grain boundary ($\Delta E_{GB} = 1.28$ eV) pointing towards a current constriction effect being associated with this response. The oxygen partial pressure dependence measurement of the conductivity

under oxidizing conditions yields a slope of 0.25 for the semicircle at medium frequencies, which further supports the idea that it results from a current constriction effect.

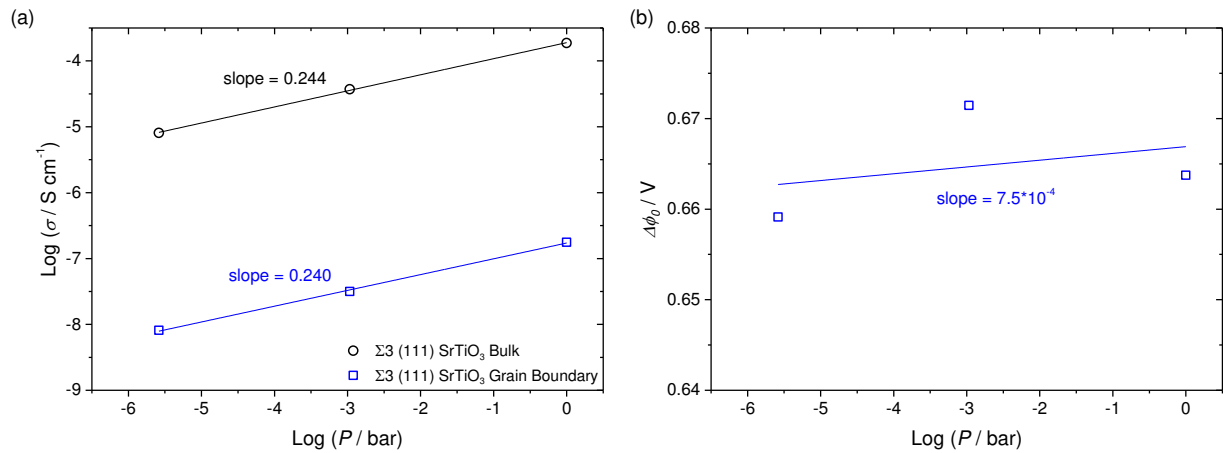


Figure 28 (a) Oxygen partial pressure dependence under oxidizing conditions at 500°C of the bulk and grain boundary conductivity of the $\Sigma 3$ (111) SrTiO_3 bicrystal sintered at $T = 1200^\circ\text{C}$, (b) oxygen partial pressure dependence of the space charge potential under oxidizing conditions in the same bicrystal.

The test run with the $\Sigma 3$ (111) SrTiO_3 bicrystal sintered at 1200°C yielded a relatively high percentage of bonded area and very importantly displayed three very well separated semicircles in the impedance spectrum which can be easily fitted. Therefore, the following sintering parameters were then chosen for the series production of $\Sigma 3$ (111) and $\Sigma 13$ (510) SrTiO_3 bicrystals (including Rb decorated ones) by spark plasma sintering: $T = 1200^\circ\text{C}$, holding time 20 minutes, applied pressure of 24 MPa, Ar atmosphere. For this purpose new (111) and (510) oriented SrTiO_3 single crystals, for the largest part cut from one boule, were ordered. The results of the electrochemical characterization of the undoped versions of these bicrystals are presented in the following sections.

4.2.1.2 $\Sigma 3$ (111) SrTiO_3 bicrystals

Unfortunately, although several attempts were performed, the results from the test runs could be roughly reproduced only once. For the other $\Sigma 3$ (111) bicrystals the optical assessment after sintering also suggested successful bonding, however the impedance spectra allowed no clear assignment of the semicircles besides the bulk one. Nevertheless, it is instructive to consider the sample exhibiting the closest impedance spectrum to what was expected from the preliminary tests. The respective impedance spectrum as well as the temperature dependence of the conductivity of this bicrystal are presented in Figure 29. The impedance spectrum displays, as expected from the preliminary tests, three more or less separated semicircles which have their usual physico-chemical meaning: The semicircle at the highest frequencies is associated with the bulk. The response at medium frequencies can be excluded to result

from the grain boundary based on the space charge layer width of $\lambda^* \approx 10 \mu\text{m}$ associated with it, whereas the semicircle at the lowest frequencies should stem from the grain boundary, based on the evaluation of $\lambda^* \approx 350 \text{ nm}$. Since the focus of this work lies on the grain boundary properties, in the following only the low frequency contribution is discussed in detail.

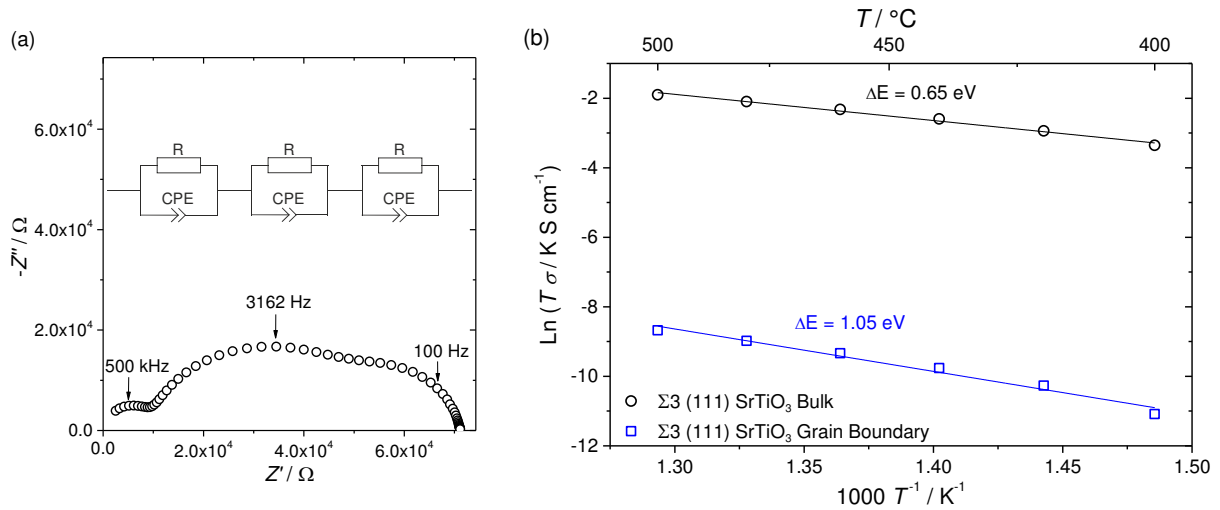


Figure 29 (a) Impedance spectrum of a $\Sigma 3$ (111) SrTiO_3 bicrystal (data collected at $T = 400^\circ\text{C}$ in pure oxygen) and the equivalent circuit used for the fitting, (b) Arrhenius plot of the conductivities of bulk and grain boundary of the same SrTiO_3 bicrystal, data collected in pure oxygen between 400°C and 500°C .

Compared to the preliminary test ($\Delta E = 1.28 \text{ eV}$) and also the literature data on $\Sigma 5$ SrTiO_3 bicrystals [4] ($\Delta E = 1.40 \text{ eV}$) the activation energy of the grain boundary conductivity in this $\Sigma 3$ (111) SrTiO_3 bicrystal in pure oxygen atmosphere of $\Delta E = 1.05 \text{ eV}$ seems to be rather low. For further comparison with the $\Sigma 3$ (111) bicrystal pressed during the preliminary tests the temperature dependence of the space charge potential of both bicrystals, under oxygen atmosphere, is displayed in Figure 30. The absolute values of the space charge potentials of both $\Sigma 3$ (111) bicrystals are perfectly within the range of typical values found for SrTiO_3 grain boundaries [5, 58, 59]. However, only the bicrystal produced in the preliminary tests displays a temperature dependence of the space charge potential as it was expected according to the work by De Souza *et al.* [5], in which a slight increase of the space charge potential upon decreasing the temperature was determined. This leads us to the conclusion that only the data from the $\Sigma 3$ (111) SrTiO_3 bicrystal produced during the preliminary test runs should be considered to actually display grain boundary properties of a $\Sigma 3$ (111) orientation.

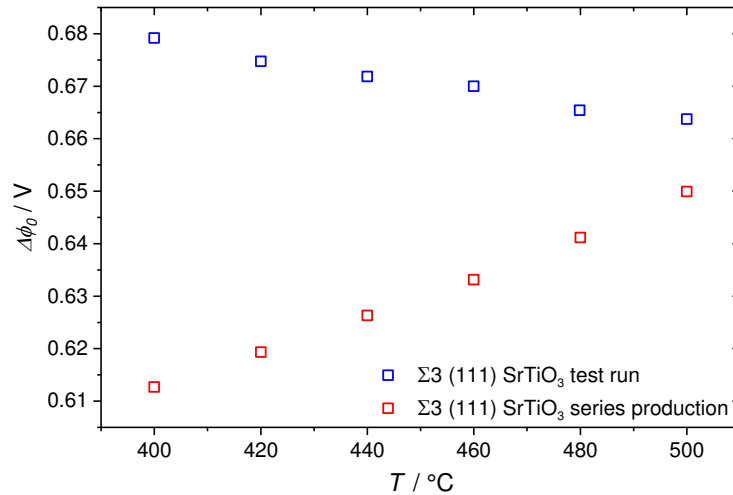


Figure 30 Temperature dependence of the space charge potential in the $\Sigma 3$ (111) SrTiO_3 bicrystal from the test run and the series production, respectively.

4.2.1.3 $\Sigma 13$ (510) SrTiO_3 bicrystals

For the $\Sigma 13$ (510) orientation only in very few cases bonding between the single crystals was achieved. This might be related to the fact that this type of grain boundary, compared to $\Sigma 3$ (111), possesses a higher grain boundary energy which makes it more difficult to realize this orientation. Possibly a longer holding time which may not be accessible with the spark plasma sintering setup is needed.

In one case the electrochemical characterization of an apparently at least partially well bonded $\Sigma 13$ (510) bicrystal yielded an impedance spectrum with a shape similar to what was expected from the $\Sigma 3$ (111) orientations (see Figure 31 (a)). The impedance spectrum consists of three semicircles, of which the one at medium and the one at low frequencies partially overlap. As usual the semicircle at the highest frequencies can be assigned to bulk SrTiO_3 . For the remaining two responses their respective Mott-Schottky space charge layer widths are calculated based on their capacitances, yielding at 500°C $\lambda^* = 28.9 \mu\text{m}$ for the response at medium frequencies and $\lambda^* = 479 \text{ nm}$ for the response at low frequencies. This could lead to the conclusion that, although the space charge layer width is already rather large, the low frequency contribution of the impedance spectrum might stem from the grain boundary. However, if one also considers the temperature dependence of the conductivity in pure oxygen atmosphere displayed in Figure 31 (b), it stands out that the alleged grain boundary contribution displays an activation energy $\Delta E = 0.75 \text{ eV}$, which is very similar to the bulk activation energy $\Delta E = 0.79 \text{ eV}$. However, based on the fact that a $\Sigma 13$ (510) grain boundary exhibits a higher misorientation than the $\Sigma 3$ (111) orientation it should actually display a higher activation energy than this orientation for which $\Delta E = 1.28 \text{ eV}$ (see Figure 26 (b)) was

determined. These facts indicate that the grain boundary contribution cannot be safely identified in these impedance spectra.

Although for all the presented undoped bicrystals the impedance spectra are fairly similar, it is for some samples possible to unambiguously assign the semicircle at the lowest frequencies to the grain boundary while in others this is clearly not possible. The reasons for such an erratic behavior are at the moment unclear. Nonetheless, despite such scattered results, it is clear that spark plasma sintering can be used to prepare SrTiO₃ bicrystals.

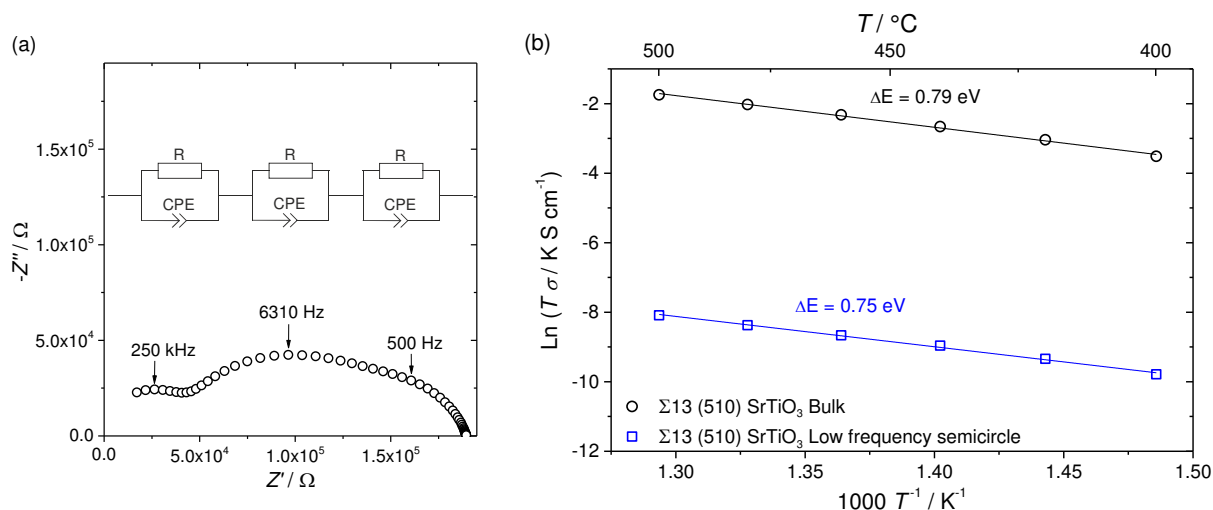


Figure 31 (a) Impedance spectrum of a $\Sigma 13$ (510) SrTiO₃ bicrystal (data collected at $T = 400^\circ\text{C}$ in pure oxygen) and the equivalent circuit used for the fitting, (b) Arrhenius plot of the conductivities of bulk and the low frequency semicircle in the impedance spectrum of the same SrTiO₃ bicrystal, data collected in pure oxygen between 400°C and 500°C .

4.2.2 Rb decorated $\Sigma 3$ (111) SrTiO₃ bicrystals

Since the conductivity enhancing effect of a Rb decoration at the grain boundaries was unequivocally confirmed for the nanocrystalline ceramics it was consequently tested if similar results could be achieved on the bicrystals. For this $\Sigma 3$ (111) oriented bicrystals were chosen, because only for this orientation it was in one sample possible to unambiguously detect the grain boundary in an impedance spectrum as shown in chapter 4.2.1.1. Two Rb contents, namely 25% and 250% coverage of the single crystal surface by Rb ions, were employed for the decoration (cf. chapter 3.1.2). For both decoration contents the measured impedance spectra differ quite a bit regarding their shape and also the conductivities deduced from them. Therefore, in both cases selected examples are discussed in the following two sections.

4.2.2.1 25% Rb coverage

With this decoration content bonding was achieved for several bicrystals, however the characterization by impedance spectroscopy yielded only for one sample a spectrum which resembles that of the undoped bicrystals. The results of the electrochemical characterization of this sample are displayed in Figure 32. The impedance spectrum in Figure 32 (a) consists of three semicircles of which the ones at medium and low frequencies overlap to a certain extent. As for all other bicrystals before, the semicircle at high frequencies can be assigned to the bulk of SrTiO₃. In order to distinguish the other two responses their respective space charge layer widths are calculated based on their fitted capacitances, yielding at 400°C $\lambda^* = 13.1 \mu\text{m}$ for the contribution at medium frequencies and $\lambda^* = 2.9 \mu\text{m}$ for the contribution at low frequencies. Obviously these values are both too high to be characteristic of a grain boundary in a SrTiO₃ bicrystal. As shown in the previous sections, even in a bicrystal with very low impurity content the space charge layer width should be on the order of 100 - 300 nm. However, since so far the grain boundary could always be assigned to the low frequency contribution in the impedance spectrum and this response here at least displays the lower space charge layer width of the two unknown responses its properties are further investigated. From the temperature dependence measurement in pure oxygen atmosphere (cf. Figure 32 (b)) it can be seen that for the low frequency semicircle an activation energy $\Delta E = 1.13 \text{ eV}$ results, which is slightly lower than what was determined for the undoped $\Sigma 3$ (111) bicrystal ($\Delta E = 1.28 \text{ eV}$, cf. Figure 26 (b)). Also the conductivity of the low frequency response in the Rb decorated bicrystal is higher than the grain boundary conductivity in the undoped bicrystal. These findings would match with the expected grain boundary conductivity enhancing effect of such a moderate Rb decoration.

For further comparison the space charge potential which would result from the low frequency response in the Rb decorated bicrystal is calculated according to equation 2.38. In Figure 33 the temperature dependence of this possible space charge potential in the Rb decorated bicrystal is compared to the space charge potential which was unambiguously determined for the undoped $\Sigma 3$ (111) bicrystal (see Figure 27). The space charge potential being lower for the Rb decorated bicrystal would again match with the observations on the Rb decorated nanocrystalline ceramics, where for the 3at% Rb decorated composition a reduction of the space charge potential as a consequence of the Rb decoration was unequivocally determined (cf. chapter 4.1.5). Overall it can therefore be concluded that regarding the conduction properties of the low frequency contribution it would fit to a SrTiO₃ grain boundary, whereas

the capacitance resulting from the fit of this semicircle clearly does not match with the expected values of a SrTiO_3 grain boundary.

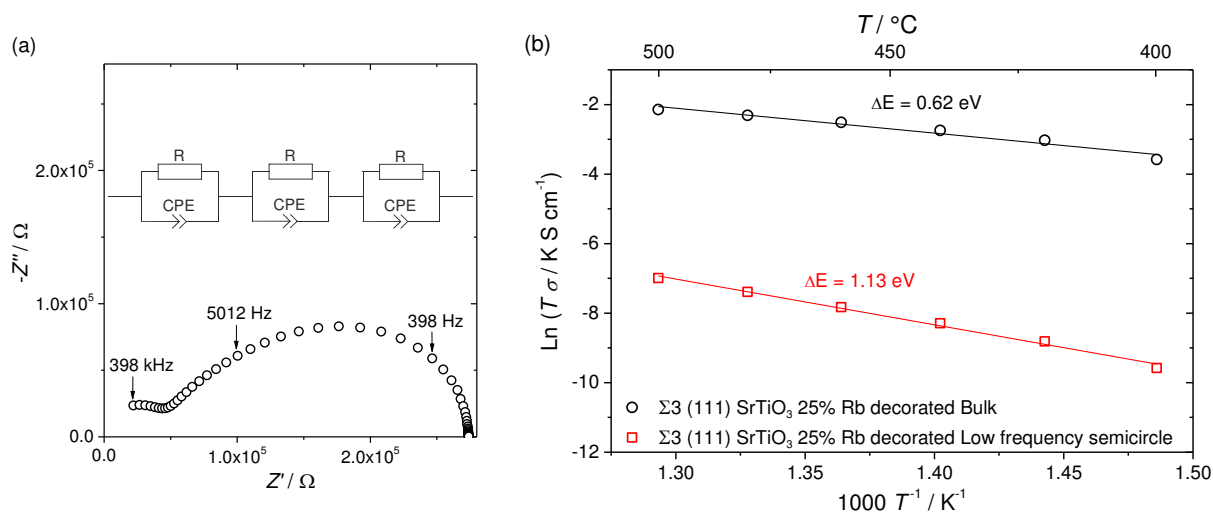


Figure 32 (a) Impedance spectrum of a $\Sigma 3$ (111) 25% Rb decorated SrTiO_3 bicrystal (data collected at $T = 400^\circ\text{C}$ in pure oxygen) and the equivalent circuit used for the fitting, (b) Arrhenius plot of the conductivities of bulk and the low frequency semicircle in the impedance spectrum of the same SrTiO_3 bicrystal, data collected in pure oxygen between 400°C and 500°C .

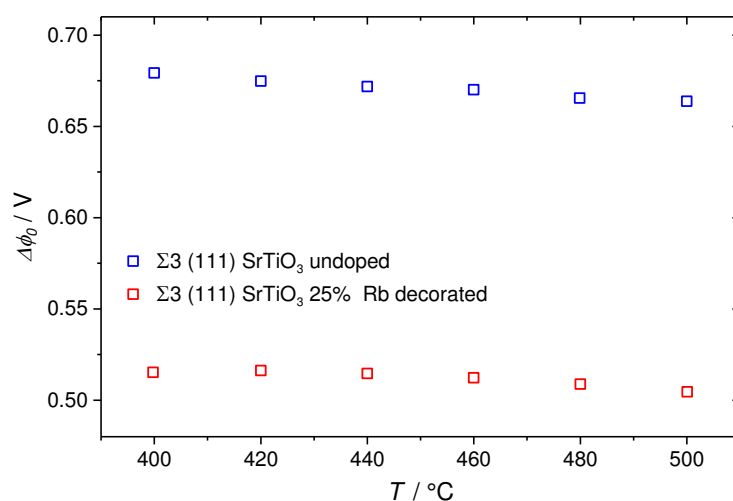


Figure 33 Temperature dependence of the space charge potential in the undoped and the 25% Rb decorated $\Sigma 3$ (111) SrTiO_3 bicrystal (note that in the case of the Rb decorated bicrystal the space charge potential was determined for the low frequency semicircle in the impedance spectrum, although it cannot be unambiguously assigned to the grain boundary).

4.2.2.2 250% Rb coverage

Electrochemical impedance spectroscopy measurements of the three bicrystals that were successfully fabricated with 250% Rb decoration content yield completely differently shaped spectra. One of these however exhibits some similarities to the impedance spectra of the undoped bicrystals and will therefore be discussed in the following. As can be seen from Figure 34 (a) and (b) a very small semicircle occurs at the highest frequencies, which can be assigned to the bulk of SrTiO₃. Continuing towards medium frequencies another smaller semicircle follows, which however overlaps and is dominated by a very large semicircle at low frequencies. The sequence of these three semicircles as well as the partial overlap of the semicircles at medium and low frequencies resembles the spectra of the undoped bicrystals. However, the total resistance of the low frequency semicircle relative to the bulk semicircle is much larger for the 250% Rb decorated bicrystal. For the possible assignment of either the medium or the low frequency contribution to the grain boundary the Mott-Schottky space charge layer widths associated with them are calculated for $T = 400^\circ\text{C}$ based on their capacitances. This results in $\lambda^* = 19.5 \mu\text{m}$ and $\lambda^* = 20.4 \mu\text{m}$ for the response at medium and low frequencies, respectively. Similar to the 25% Rb decorated bicrystal these values are far too high to relate them to a grain boundary. Nevertheless, since for the undoped SrTiO₃ bicrystals the grain boundary could be assigned to the semicircle at low frequencies, here the temperature dependence of the conductivity under pure oxygen atmosphere of this semicircle (see Figure 35 (a)) as well as the possible space charge potential associated with it are determined (see Figure 35 (b)). The investigation of the Rb decorated nanocrystalline ceramics showed that the introduction of a too high Rb content at the grain boundary can actually have a negative influence on the electrical conduction properties. Beyond a certain threshold concentration the preferable incorporation of Rb on interstitial sites increases the space charge potential compared to undoped SrTiO₃. The conduction properties of the low frequency semicircle confirm these expectations for the properties of a grain boundary with such a high Rb content: Its activation energy of $\Delta E = 1.45 \text{ eV}$ is higher than that of the undoped $\Sigma 3$ (111) bicrystal for which $\Delta E = 1.28 \text{ eV}$ was determined and consequently also the space charge potential is increased compared to the undoped bicrystal. Completely analog to the 25% Rb decorated bicrystal, however, one has to keep in mind that the fitted capacitance of the low frequency contribution does not match with a grain boundary response.

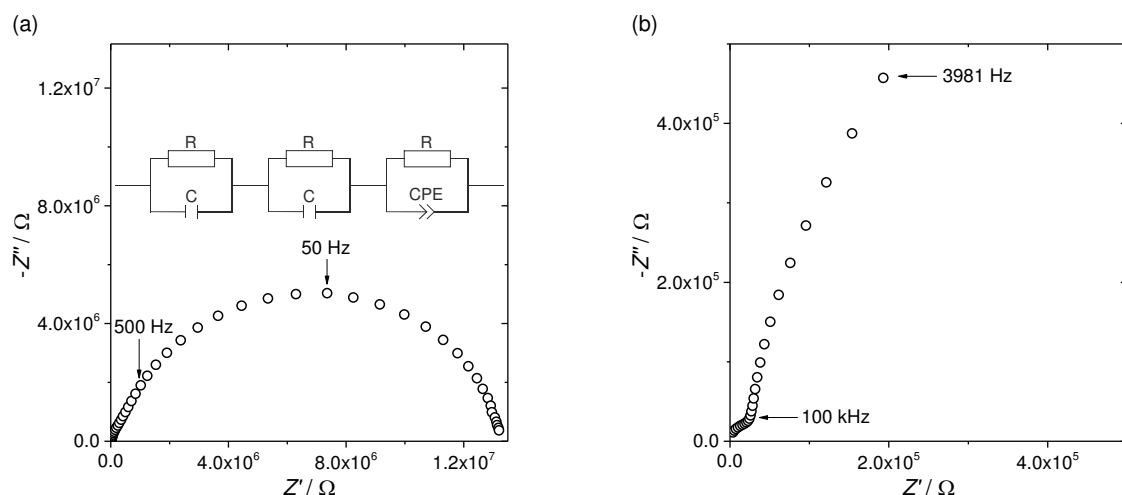


Figure 34 (a) Impedance spectrum of a $\Sigma 3$ (111) 250% Rb decorated SrTiO_3 bicrystal (data collected at $T = 400^\circ\text{C}$ in pure oxygen) and the equivalent circuit used for the fitting, (b) high frequency part of the impedance spectrum in (a).

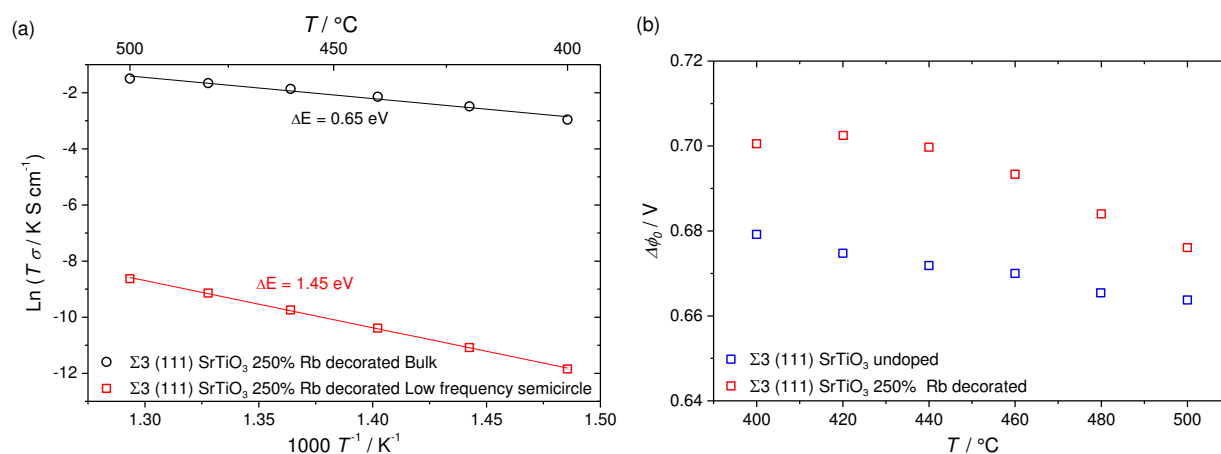


Figure 35 (a) Arrhenius plot of the conductivities of bulk and the low frequency semicircle in the impedance spectrum of the 250% Rb decorated SrTiO_3 bicrystal, data collected in pure oxygen between 400°C and 500°C , (b) Temperature dependence of the space charge potential in the undoped and the 250% Rb decorated $\Sigma 3$ (111) SrTiO_3 bicrystal (note that in the case of the Rb decorated bicrystal the space charge potential was determined for the low frequency semicircle in the impedance spectrum, although it cannot be unambiguously assigned to the grain boundary).

5 Conclusions

The present thesis addresses the reduction of the positive space charge potential in SrTiO₃ via a local grain boundary decoration with a large sized element, namely Rb. For this purpose nanocrystalline mesoscopic samples as well as home-made bicrystals were investigated. The electrical conduction properties of the samples were studied by electrochemical impedance spectroscopy and the results are interpreted in the framework of the space charge model applying the well-known Mott-Schottky model to describe the space charge layers.

In the case of nanocrystalline mesoscopic SrTiO₃ (grain size on the order of 60 nm) it was shown that by locally decorating the surface of the SrTiO₃ particles with RbNO₃ prior to sintering a highly doped very thin shell along the grain boundaries is generated in the sintered ceramics. The diffusion of Rb is limited by employing spark plasma sintering which uses very low sintering temperatures and short holding times. The local confinement of the Rb was confirmed by TEM EDX line scans across the grain boundaries, in which a Rb signal was only detected within a total length of roughly 1 nm across the grain boundaries. The results of the electrochemical characterization demonstrate the existence of an optimal decoration content at which the maximal increase of the p-type conductivity, as well as a maximal decrease of the activation energy for the p-type conductivity compared to an undoped reference sample can be achieved. The improved conductivity properties also result in a reduction of the space charge potential. After crossing this optimal point an opposing trend sets in. These observations can be explained by the following hypothesis: Starting from a nominally undoped SrTiO₃ grain boundary and gradually adding Rb in the grain boundary core it first substitutes Sr, which creates negative charges. The further the Rb content is increased it more and more occupies interstitial sites because of electrostatic reasons, which creates positive charges. Depending on the concentrations of Rb on Sr sites and on interstitial sites, relative to each other, the grain boundary core charge is altered compared to the undoped grain boundary. For 3at% Rb decorated SrTiO₃ a net negative charge from the incorporated Rb leads to a reduction of the space charge potential, whereas in the 5.5at% Rb decorated SrTiO₃ the space charge potential is very similar to that of undoped SrTiO₃, showing that $[Rb'_{Sr}] \approx [Rb_i^\bullet]$. Furthermore the oxygen partial pressure dependence measurements of the electrical conductivities of the samples pointed towards a slight band gap reduction for the sample decorated with 3at% Rb compared to the undoped and 5.5at% Rb decorated samples. This finding was tested by performing diffuse reflectance spectroscopy on

the polished sample surfaces which confirmed the band-gap differences deduced from the electrochemical characterization.

In the case of the SrTiO₃ bicrystals it was first and foremost a challenge to repeatably produce the two orientations $\Sigma 3(111)$ and $\Sigma 13(510)$ by spark plasma sintering, since this was, to the best of the author's knowledge, at the time the experiments were performed during the thesis the very first time that production of SrTiO₃ bicrystals by spark plasma sintering was attempted. For the $\Sigma 3(111)$ orientation it was to some extent possible to produce multiple samples, whereas for most of the attempts on the $\Sigma 13(510)$ orientation it proved difficult to achieve an acceptable bonding between the two single crystals. This may be related to the fact that the $\Sigma 13(510)$ boundary is energetically less favorable and would therefore need a longer bonding time, which may not be accessible due to the limited holding time in the spark plasma sintering machine. Accordingly this part of the thesis focused on the $\Sigma 3(111)$ orientation. Here it was exemplarily shown that the production of SrTiO₃ bicrystals by spark plasma sintering is possible and the grain boundary could be assigned to a certain response in the impedance spectrum. In continuation of the Rb decorated nanocrystalline SrTiO₃ ceramics also the decoration of a single grain boundary with Rb was attempted, testing two different decoration contents. ICP-OES measurements confirmed that it is possible to attach RbNO₃ to the single crystal surface in a similar manner as it was done with nanocrystalline SrTiO₃ powder. However, the electrochemical characterization by impedance spectroscopy gave ambiguous results regarding the enhancement of p-type conductivity that was expected from the nanocrystalline samples. At this point it can only be stated that some bicrystals point towards a similar p-type conductivity enhancing effect, however, overall the data still scatters too much. It is assumed that, although optically always a small well bonded part of the bicrystal was cut out for measurements, on the microscopical level they probably differ too much regarding how well the two single crystals are connected.

In summary this work demonstrated how a local grain boundary decoration of SrTiO₃ can be used to systematically influence the grain boundary core charge. This method should in principle be easily transferable to other materials.

References

- [1] P. Balaya, J. Jamnik, J. Fleig, J. Maier, *Mesoscopic electrical conduction in nanocrystalline SrTiO₃*, Appl. Phys. Lett. **88** (2006).
- [2] P. Lupetin, G. Gregori, J. Maier, *Mesoscopic Charge Carriers Chemistry in Nanocrystalline SrTiO₃*, Angewandte Chemie-International Edition **49** (2010) 10123.
- [3] P. Lupetin, *Charge carrier defect chemistry of nanoscopic SrTiO₃*, PhD Thesis, Universität Stuttgart (2012).
- [4] I. Denk, J. Claus, J. Maier, *Electrochemical investigations of SrTiO₃ boundaries*, J. Electrochem. Soc. **144** (1997) 3526.
- [5] R.A. De Souza, J. Fleig, J. Maier, O. Kienzle, Z.L. Zhang, W. Sigle, M. Ruhle, *Electrical and structural characterization of a low-angle tilt grain boundary in iron-doped strontium titanate*, J. Am. Ceram. Soc. **86** (2003) 922.
- [6] R.A. De Souza, J. Maier, *Capacitance of single crystal and low-angle tilt bicrystals of Fe-doped SrTiO₃*, Faraday Discuss. **134** (2007) 235.
- [7] N.H. Chan, R.K. Sharma, D.M. Smyth, *Nonstoichiometry in SrTiO₃*, J. Electrochem. Soc. **128** (1981) 1762
- [8] U. Balachandran, N.G. Eror, *Electrical Conductivity in Strontium Titanate*, J. Solid State Chem. **39** (1981) 351.
- [9] I. Denk, W. Munch, J. Maier, *Partial conductivities in SrTiO₃: Bulk polarization experiments, oxygen concentration cell measurements, and defect-chemical modeling*, J. Am. Ceram. Soc. **78** (1995) 3265.
- [10] F. Noll, W. Munch, I. Denk, J. Maier, *SrTiO₃ as a prototype of a mixed conductor. Conductivities, oxygen diffusion and boundary effects*, Solid State Ion. **86-8** (1996) 711.
- [11] R.A. De Souza, J. Fleig, R. Merkle, J. Maier, *SrTiO₃: a model electroceramic*, Z. Metallk. **94** (2003) 218.
- [12] H.J. Scheel, *Crystal-Growth and Characterization of Strontium-Titanate, SrTiO₃*, Z. Kristall. **143** (1976) 417.
- [13] R. Waser, *Electronic properties of grain boundaries in SrTiO₃ and BaTiO₃ ceramics*, Solid State Ion. **75** (1995) 89.
- [14] R.A. De Souza, *The formation of equilibrium space-charge zones at grain boundaries in the perovskite oxide SrTiO₃*, Phys. Chem. Chem. Phys. **11** (2009) 9939.
- [15] H.L. Tuller, *Mixed Conduction in Nonstoichiometric Oxides*, pp.271 - 337, In: *Nonstoichiometric Oxides*, O.T. Sørensen, Editor, Academic Press, New York (1981).
- [16] R. Moos, K.H. Hardtl, *Defect chemistry of donor-doped and undoped strontium titanate ceramics between 1000° and 1400°C*, J. Am. Ceram. Soc. **80** (1997) 2549.

-
- [17] J. Maier, *Ionic Conduction in Space Charge Regions*, Prog. Solid State Chem. **23** (1995) 171.
- [18] P.C. McIntyre, *Equilibrium point defect and electronic carrier distributions near interfaces in acceptor-doped strontium titanate*, J. Am. Ceram. Soc. **83** (2000) 1129.
- [19] R. Waser, R. Hagenbeck, *Grain boundaries in dielectric and mixed conducting ceramics*, Acta Materialia **48** (2000) 797.
- [20] N.D. Browning, J.P. Buban, H.O. Moltaji, S.J. Pennycook, G. Duscher, K.D. Johnson, R.P. Rodrigues, V.P. Dravid, *The influence of atomic structure on the formation of electrical barriers at grain boundaries in SrTiO₃*, Appl. Phys. Lett. **74** (1999) 2638.
- [21] M. Vollman, R. Waser, *Grain Boundary Defect Chemistry of Acceptor-Doped Titanates: Space Charge Layer Width*, J. Am. Ceram. Soc. **77** (1994) 235.
- [22] J. Maier, *On the Conductivity of Polycrystalline Materials*, Ber. Bunsen-Ges. Phys. Chem. Chem. Phys. **90** (1986) 26.
- [23] H.L. Tuller, S.J. Litzelman, W. Jung, *Micro-ionics: next generation power sources*, Phys. Chem. Chem. Phys. **11** (2009) 3023.
- [24] S. Kim, J. Fleig, J. Maier, *Space charge conduction: Simple analytical solutions for ionic and mixed conductors and application to nanocrystalline ceria*, Phys. Chem. Chem. Phys. **5** (2003) 2268.
- [25] J. Maier, *Physical Chemistry of Ionic Materials: Ions and Electrons in Solids*, John Wiley & Sons, Ltd (2004).
- [26] J. Maier, *Mass storage in space charge regions of nano-sized systems (Nano-ionics. Part V)*, Faraday Discuss. **134** (2007) 51.
- [27] J. Fleig, J. Maier, *The impedance of ceramics with highly resistive grain boundaries: Validity and limits of the brick layer model*, J. Eur. Ceram. Soc. **19** (1999) 693.
- [28] J.C.C. Abrantes, J.A. Labrincha, J.R. Frade, *Applicability of the brick layer model to describe the grain boundary properties of strontium titanate ceramics*, J. Eur. Ceram. Soc. **20** (2000) 1603.
- [29] K.K. Adepalli, *Influence of Extended Defects on the Electrical Properties of TiO₂ (Rutile)*, PhD Thesis, Universität Stuttgart (2013).
- [30] J. Fleig, S. Rodewald, J. Maier, *Microcontact impedance measurements of individual highly resistive grain boundaries: General aspects and application to acceptor-doped SrTiO₃*, J. Appl. Phys. **87** (2000) 2372.
- [31] X. Guo, R. Waser, *Electrical properties of the grain boundaries of oxygen ion conductors: Acceptor-doped zirconia and ceria*, Prog. Mater. Sci. **51** (2006) 151.
- [32] S. Rodewald, J. Fleig, J. Maier, *Microcontact impedance spectroscopy at single grain boundaries in Fe-doped SrTiO₃ polycrystals*, J. Am. Ceram. Soc. **84** (2001) 521.

- [33] P. Lejček, *Grain Boundaries: Description, Structure and Thermodynamics*, pp.5 - 24, In: *Grain Boundary Segregation in Metals*, Springer, Berlin, Heidelberg (2010).
- [34] D.G. Brandon, *The Structure of High-Angle Grain Boundaries*, *Acta Metallurgica* **14** (1966) 1479.
- [35] A.P. Sutton, R.W. Balluffi, *Interfaces in Crystalline Materials*, Clarendon Press Oxford (1996).
- [36] M.L. Kronberg, F.H. Wilson, *Secondary Recrystallization in Copper*, *Transactions of the American Institute of Mining and Metallurgical Engineers* **185** (1949) 501.
- [37] R. Orru, R. Licheri, A.M. Locci, A. Cincotti, G.C. Cao, *Consolidation/synthesis of materials by electric current activated/assisted sintering*, *Mater. Sci. Eng. R-Rep.* **63** (2009) 127.
- [38] Z.A. Munir, U. Anselmi-Tamburini, M. Ohyanagi, *The effect of electric field and pressure on the synthesis and consolidation of materials: A review of the spark plasma sintering method*, *J. Mater. Sci.* **41** (2006) 763.
- [39] H. Yoshida, K. Morita, B.N. Kim, K. Hiraga, K. Yamanaka, K. Soga, T. Yamamoto, *Low-Temperature Spark Plasma Sintering of Ytria Ceramics with Ultrafine Grain Size*, *J. Am. Ceram. Soc.* **94** (2011) 3301.
- [40] J. Fleig, *The grain boundary impedance of random microstructures: numerical simulations and implications for the analysis of experimental data*, *Solid State Ion.* **150** (2002) 181.
- [41] A. Brandao, J.F. Monteiro, A.V. Kovalevsky, D.P. Fagg, V.V. Kharton, J.R. Frade, *Guidelines for improving resistance to CO₂ of materials for solid state electrochemical systems*, *Solid State Ion.* **192** (2011) 16.
- [42] P. Balaya, M. Ahrens, L. Kienle, J. Maier, B. Rahmati, S.B. Lee, W. Sigle, *Synthesis and characterization of nanocrystalline SrTiO₃*, *J. Am. Ceram. Soc.* **89** (2006) 2804.
- [43] J. Fleig, J. Maier, *Finite-element calculations on the impedance of electroceramics with highly resistive grain boundaries: I, laterally inhomogeneous grain boundaries*, *J. Am. Ceram. Soc.* **82** (1999) 3485.
- [44] J. Fleig, J. Maier, *Finite element calculations of impedance effects at point contacts*, *Electrochimica Acta* **41** (1996) 1003.
- [45] J. Fleig, P. Pham, P. Sztulzaft, J. Maier, *Inhomogeneous current distributions at grain boundaries and electrodes and their impact on the impedance*, *Solid State Ion.* **113** (1998) 739.
- [46] S. Kim, J. Maier, *On the conductivity mechanism of nanocrystalline ceria*, *J. Electrochem. Soc.* **149** (2002) J73.
- [47] J. Jamnik, X. Guo, J. Maier, *Field-induced relaxation of bulk composition due to internal boundaries*, *Appl. Phys. Lett.* **82** (2003) 2820.

- [48] J.R. Jurado, M.T. Colomer, J.R. Frade, *Electrical characterization of Sr_{0.97}Ti_{1-x}Fe_xO_{3-delta} by complex impedance spectroscopy: I, materials with low iron contents*, J. Am. Ceram. Soc. **83** (2000) 2715.
- [49] R. Waser, *Bulk Conductivity and Defect Chemistry of Acceptor-Doped Strontium-Titanate in the Quenched State*, J. Am. Ceram. Soc. **74** (1991) 1934.
- [50] Y.M. Chiang, T. Takagi, *Grain-Boundary Chemistry of Barium-Titanate and Strontium-Titanate: I, High-Temperature Equilibrium Space-Charge*, J. Am. Ceram. Soc. **73** (1990) 3278.
- [51] N.D. Browning, S.J. Pennycook, *Direct experimental determination of the atomic structure at internal interfaces*, J. Phys. D-Appl. Phys. **29** (1996) 1779.
- [52] F. Ernst, O. Kienzle, M. Ruhle, *Structure and composition of grain boundaries in ceramics*, J. Eur. Ceram. Soc. **19** (1999) 665.
- [53] R.D. Shannon, *Revised Effective Ionic Radii and Systematic Studies of Interatomic Distances in Halides and Chalcogenides*, Acta Crystallogr. Sect. A **32** (1976) 751.
- [54] D.J. Kok, K. Irmscher, M. Naumann, C. Guguschev, Z. Galazka, R. Uecker, *Temperature-dependent optical absorption of SrTiO₃*, Phys. Status Solidi A-Appl. Mat. **212** (2015) 1880.
- [55] L.F. da Silva, J.C. M'Peko, J. Andres, A. Beltran, L. Gracia, M.I.B. Bernardi, A. Mesquita, E. Antonelli, M.L. Moreira, V.R. Mastelaro, *Insight into the Effects of Fe Addition on the Local Structure and Electronic Properties of SrTiO₃*, J. Phys. Chem. C **118** (2014) 4930.
- [56] A. Rothschild, W. Menesklou, H.L. Tuller, E. Ivers-Tiffée, *Electronic structure, defect chemistry, and transport properties of SrTi_{1-x}Fe_xO_{3-y} solid solutions*, Chem. Mat. **18** (2006) 3651.
- [57] G. Gregori, S. Heinze, P. Lupetin, H.U. Habermeier, J. Maier, *Seebeck coefficient and electrical conductivity of mesoscopic nanocrystalline SrTiO₃*, J. Mater. Sci. **48** (2013) 2790.
- [58] J. Fleig, B. Rahmati, S. Rodewald, J. Maier, *On the localized impedance spectroscopic characterization of grain boundaries: General aspects and experiments on undoped SrTiO₃*, J. Eur. Ceram. Soc. **30** (2010) 215.
- [59] M. Leonhardt, J. Jamnik, J. Maier, *In situ monitoring and quantitative analysis of oxygen diffusion through Schottky-barriers in SrTiO₃ bicrystals*, Electrochem. Solid State Lett. **2** (1999) 333.

Acknowledgements

I would like to express my deep gratitude to Professor Dr. Joachim Maier for giving me the opportunity to pursue my work on this interesting topic. Our discussions and his valuable suggestions contributed greatly to the completion of this thesis. The work in his department allowed me to gain a much deeper understanding of the many different facets of electrochemistry.

I would like to thank Professor Dr. Anke Weidenkaff and Professor Dr. Thomas Schleid for reviewing my thesis and accepting to be in the examination committee.

Heartfelt thanks goes to my daily supervisor Dr. Giuliano Gregori for always believing in me and my work. Even when an experiment failed he kept his positive attitude and tried to help to extract some information from it. His broad scientific knowledge helped the progress of this thesis a lot, while his friendly and open manner made every day work with him very enjoyable. Special thanks to him for discussing and correcting my thesis even after he left the MPI for Solid State Research.

I also like to thank Dr. Jone Zabaleta for being part of my internal PhD committee, she always showed sincere interest in my work and offered her help where it was possible.

I appreciate all the people who contributed in many different ways to my work. I want to thank Dr. Rotraut Merkle for valuable scientific discussions as well as performing the TGA measurements; Annette Fuchs for conducting the SEM measurements, BET measurements and density measurements by helium pycnometry; Barbara Baum (crystal preparation group) for spending countless hours cutting SrTiO₃ bicrystals for me; Gabi Götz and Helga Hoier for XRD measurements; Ute Salzberger and Wilfried Sigle for the TEM sample preparation and the TEM measurements, respectively; Benjamin Stuhlhofer for application of the YBCO electrodes; Samir Hammoud, Gerhard Werner and Marie-Luise Schreiber for performing the chemical analysis; Benjamin Bruha for conducting the diffuse reflectance spectroscopy measurements; Udo Klock for support with the electronic equipment; Ewald Schmitt, Florian Kaiser and Armin Sorg for technical support; Uwe Traub for IT support; Peter Senk for help with furnaces and Sofia Weiglein for the administrative support.

I thank all my former and current PhD colleagues of the Maier department for fruitful scientific discussions as well as the remarkable team spirit: Dr. Kiran Adepalli, Marco Arrigoni, Dr. Federico Baiutti, Dr. Chia-Chin Chen, Dr. Oliver Gerbig, Dr. Elisa Gilardi, Dr. Marcus Göbel, Pinar Kaya, Dr. Gints Kucinskis, Simon Lorger, Dr. Piero Lupetin, Dr. Jan

Melchior, Andreas Münchinger, Maryam Nojabae, Dr. Nils Ohmer, Dr. Christian Pfaffenhuber, Dr. Daniel Pöttsch, Torben Saatkamp, Maximilian Schaube, Alessandro Senocrate, Dr. Sebastian Stämmler, Dr. Andreas Wohlfarth, Reihaneh Zohourian.

As a great football enthusiast I want to especially mention the Inter Maier football team and all its various players over the years, it was always a pleasure fighting for the Minerva Cup together with you.

I want to thank my parents Karin and Klaus, as well as my sister Maren and my brother Matthias for all their love and encouragement over the years. Particularly in the tougher times of the PhD thesis the strong family bonds kept me moving forward.

Last but not least I want to thank my wife Lisa, her share in this work cannot be described by words and I am endlessly grateful for having her at my side.

